

La sottoscritta Carmen Perri nata a Rossano (CS) il 20/12/1995 residente a Saarbrücken in via Mainzer Strasse 15  
e-mail carmen.perri @poliba.it

iscritto al 3° anno di Corso di Dottorato di Ricerca in Ingegneria Elettrica e dell'Informazione ciclo XXXVI°

ed essendo stato ammesso a sostenere l'esame finale con la prevista discussione della tesi dal titolo:

**Design, Modelling, and Control of a high voltage driving circuit for dielectric elastomer actuators**

**DICHIARA**

- 1) di essere consapevole che, ai sensi del D.P.R. n. 445 del 28.12.2000, le dichiarazioni mendaci, la falsità negli atti e l'uso di atti falsi sono puniti ai sensi del codice penale e delle Leggi speciali in materia, e che nel caso ricorreranno dette ipotesi, decade fin dall'inizio e senza necessità di nessuna formalità dai benefici conseguenti al provvedimento emanato sulla base di tali dichiarazioni;
- 2) di essere iscritto al Corso di Dottorato di ricerca Ingegneria Elettrica e dell'Informazione ciclo XXXVI°, corso attivato ai sensi del "Regolamento dei Corsi di Dottorato di ricerca del Politecnico di Bari", emanato con D.R. n.286 del 01.07.2013;
- 3) di essere pienamente a conoscenza delle disposizioni contenute nel predetto Regolamento in merito alla procedura di deposito, pubblicazione e autoarchiviazione della tesi di dottorato nell'Archivio Istituzionale ad accesso aperto alla letteratura scientifica;
- 4) di essere consapevole che attraverso l'autoarchiviazione delle tesi nell'Archivio Istituzionale ad accesso aperto alla letteratura scientifica del Politecnico di Bari (IRIS-POLIBA), l'Ateneo archiverà e renderà consultabile in rete (nel rispetto della Policy di Ateneo di cui al D.R. 642 del 13.11.2015) il testo completo della tesi di dottorato, fatta salva la possibilità di sottoscrizione di apposite licenze per le relative condizioni di utilizzo (di cui al sito <http://www.creativecommons.it/Licenze>), e fatte salve, altresì, le eventuali esigenze di "embargo", legate a strette considerazioni sulla tutelabilità e sfruttamento industriale/commerciale dei contenuti della tesi, da rappresentarsi mediante compilazione e sottoscrizione del modulo in calce (Richiesta di embargo);
- 5) che la tesi da depositare in IRIS-POLIBA, in formato digitale (PDF/A) sarà del tutto identica a quelle **consegnate**/inviata/da inviarsi ai componenti della commissione per l'esame finale e a qualsiasi altra copia depositata presso gli Uffici del Politecnico di Bari in forma cartacea o digitale, ovvero a quella da discutere in sede di esame finale, a quella da depositare, a cura dell'Ateneo, presso le Biblioteche Nazionali Centrali di Roma e Firenze e presso tutti gli Uffici competenti per legge al momento del deposito stesso, e che di conseguenza va esclusa qualsiasi responsabilità del Politecnico di Bari per quanto riguarda eventuali errori, imprecisioni o omissioni nei contenuti della tesi;
- 6) che il contenuto e l'organizzazione della tesi è opera originale realizzata dal sottoscritto e non compromette in alcun modo i diritti di terzi, ivi compresi quelli relativi alla sicurezza dei dati personali; che pertanto il Politecnico di Bari ed i suoi funzionari sono in ogni caso esenti da responsabilità di qualsivoglia natura: civile, amministrativa e penale e saranno dal sottoscritto tenuti indenni da qualsiasi richiesta o rivendicazione da parte di terzi;
- 7) che il contenuto della tesi non infrange in alcun modo il diritto d'Autore né gli obblighi connessi alla salvaguardia di diritti morali ed economici di altri autori o di altri aventi diritto, sia per testi, immagini, foto, tabelle, o altre parti di cui la tesi è composta.

Luogo e data Saarbrücken, 06/11/2024

Firma



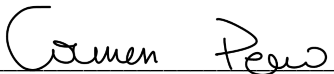
Il/La sottoscritto, con l'autoarchiviazione della propria tesi di dottorato nell'Archivio Istituzionale ad accesso aperto del Politecnico di Bari (POLIBA-IRIS), pur mantenendo su di essa tutti i diritti d'autore, morali ed economici, ai sensi della normativa vigente (Legge 633/1941 e ss.mm.ii.),

**CONCEDE**

- al Politecnico di Bari il permesso di trasferire l'opera su qualsiasi supporto e di convertirla in qualsiasi formato al fine di una corretta conservazione nel tempo. Il Politecnico di Bari garantisce che non verrà effettuata alcuna modifica al contenuto e alla struttura dell'opera.
- al Politecnico di Bari la possibilità di riprodurre l'opera in più di una copia per fini di sicurezza, back-up e conservazione.

Luogo e data Saarbrücken, 06/11/2024

Firma





Politecnico  
di Bari

Department of ELECTRICAL AND INFORMATION  
ENGINEER (DEI)

PH.D. PROGRAM  
SSD. ING-INF/04-AUTOMATICA

Final Dissertation

---

# Design, Modelling, and Control of a high voltage driving circuit for dielectric elastomer actuators

---

by

Carmen Perri

Referees:

Prof.

Prof.

Supervisors:

Prof. Ing. David Naso

Jun.-Prof. Gianluca Rizzello

*Coordinator of Ph.D. Program:  
Prof. Mario Carpentieri*

---

*Course n° 36, 01/11/2020–31/07/2024*



Politecnico  
di Bari

Department of ELECTRICAL AND INFORMATION  
ENGINEER (DEI)

PH.D. PROGRAM  
SSD. ING-INF/04-AUTOMATICA

Final Dissertation

---

# Design, Modelling, and Control of a high voltage driving circuit for dielectric elastomer actuators

---

by

Carmen Perri

Referees:

Prof.

Prof.

Supervisors:

Prof. Ing. David Naso

Jun.-Prof. Gianluca Rizzello

*Coordinator of Ph.D. Program:*

*Prof. Mario Carpentieri*

---

Course n° 36, 01/11/2020-31/07/2024



*To those who have always been there.*

*To those who are not here anymore.*

*To those who have believed in me from the beginning.*

*And until the end.*

*To my beloved family.*

# Acknowledgments

I would like to thank my supervisor Prof. David Naso from Politecnico di Bari for motivating me and my work, for giving me the opportunity of amplifying my research interests through my Ph.D. years, and for letting me support his teaching activities.

I would also like to express my gratitude to my co-supervisor, Jun.-Prof. Gianluca Rizzello from Universität des Saarlandes, for his unwavering guidance, support of my ideas and work, and the numerous scientific discussions that significantly enhanced my research.

My thanks also go to Prof. Stefan Seelecke from Universität des Saarlandes for hosting me in his laboratory and inspiring my interest in smart materials.

My thanks go personally to Benedikt Holz, Thomas Würtz, and Dr. Paolo Massenio for their help and constant support with my research topic.

I would like to extend my personal thanks to everyone at the Intelligent Material Systems Laboratory of Universität des Saarlandes for their warm welcome, inspirational ideas, and, most importantly, their support both professionally and personally. I have found not only colleagues but, more significantly, friends among them.

I would like to thank my friend Nadia Triki. Her presence and enthusiasm have greatly contributed to make this experience more enjoyable. She became for me the perfect travel companion, the best confidant, a lovely sister.

I am personally grateful to my friend Domenico Bevilacqua for his constant presence through those years, always reminding me of *home*. The word 'friend' does not fully describe the importance of his role in my life; he has been so much more. By always being there for me, I could not have wished for a better person by my side.

I want to express my deepest gratitude to my boyfriend, Andreas Meyer, for his unwavering encouragement and understanding. He has been not only my partner in countless discussions about my research but also my partner in life, bringing patience, support, and love to every step of this journey. His support has been a source of strength and comfort, a gentle reassurance that has carried me through even the toughest times. Words can scarcely convey how profoundly grateful I am for him, his love, his belief in me, and the comfort he brings to my heart. Thank you, my love.

The most significant acknowledgment is reserved for my mother, my father, and my sister for always believing in me, for their precious support, which has enabled me to achieve everything I have. To the three of them I devote my work.

# Contents

<b>1</b>	<b>Introduction</b>	<b>3</b>
1.1	Motivation . . . . .	3
1.2	Thesis outline and contributions . . . . .	4
<b>2</b>	<b>Dielectric Elastomers (DEs)</b>	<b>7</b>
2.1	ElectroActive Polymers (EAPs) . . . . .	7
2.2	DEs: Feature and Applications . . . . .	9
2.3	Dielectric Elastomer Actuators (DEAs) . . . . .	11
2.4	Literature review . . . . .	16
2.4.1	Literature review on DEAs . . . . .	16
2.4.2	Literature review on HV circuits . . . . .	16
2.4.3	Literature review on modeling of HV circuits . . . . .	19
2.4.4	Literature review on control of HV circuits . . . . .	20
<b>3</b>	<b>High Voltage circuit (HV circuit)</b>	<b>23</b>
3.1	Circuitry design . . . . .	23
3.2	Charging stage operating principle . . . . .	25
3.2.1	Resonant circuit . . . . .	25
3.2.2	Greinacher circuit . . . . .	26
3.3	Discharging stage operating principle . . . . .	28
3.3.1	Passive discharging circuit . . . . .	28
3.3.2	Active discharging circuit . . . . .	28
<b>4</b>	<b>Modeling</b>	<b>30</b>
4.1	Modeling problem statement . . . . .	30
4.2	Control-oriented model . . . . .	31
4.2.1	Equivalent components models . . . . .	32
4.2.2	Charging stage model . . . . .	34
4.2.3	Discharging stage model . . . . .	46
4.2.4	Switching model . . . . .	48
4.3	Average model . . . . .	49
4.3.1	Switching model sensitivity for time-varying load . . . . .	49
4.3.2	Average model . . . . .	52
4.4	Validation in simulation . . . . .	52
4.4.1	Switching model - Validation in simulation . . . . .	53
4.4.2	Average model - Validation in simulation . . . . .	56
4.5	Experimental validation . . . . .	56

4.5.1	Experimental setup . . . . .	56
4.5.2	Experimental results . . . . .	57
<b>5</b>	<b>Control</b>	<b>65</b>
5.1	Linear voltage control . . . . .	65
5.1.1	Linearized model . . . . .	66
5.1.2	Linear controller . . . . .	66
5.2	Nonlinear voltage control . . . . .	70
5.2.1	Linear Parameter-Varying system (LPV system) and Linear Matrix Inequality optimization (LMI optimization) . . . . .	72
5.2.2	State observer . . . . .	75
5.3	Voltage controllers validation in simulation . . . . .	76
5.3.1	Linear voltage control - Validation in simulation . . . . .	76
5.3.2	Nonlinear voltage control - Validation in simulation . . . . .	79
5.4	Voltage controllers experimental validation . . . . .	82
5.4.1	Linear voltage control - Experimental validation . . . . .	83
5.4.2	Nonlinear voltage control - Experimental validation . . . . .	86
<b>6</b>	<b>Applied case of study: DEAs position control</b>	<b>90</b>
6.1	Nested control: Linear voltage and DEA's position controllers . . . . .	90
6.2	Experimental validation . . . . .	92
<b>7</b>	<b>Conclusions</b>	<b>95</b>
	<b>Bibliography</b>	<b>98</b>



# Abbreviations

The following Table 1 describes the significance of various abbreviations and acronyms used throughout the thesis. The page on which each one is defined or first used is also given.

List of abbreviation	Meaning	Page
DE	Dielectric Elastomer	3
DEA	Dielectric Elastomer Actuator	3
HV	High Voltage	3
DC	Direct Current	3
LPV	Linear Parameter Varying	5
LMI	Linear Matrix Inequality	5
EAP	Electro-Active Polymer	7
IPMC	Ionic Polymer-Metal Composite	8
CNT	Carbon Nanotube	8
DES	Dielectric Elastomer Sensor	10
VHB	Very High Bonding	11
HASEL	Hydraulically Amplified Self-healing Electrostatic	11
MEMS	Micro Electromechanical System	12
SIP	Strip In-Plane	14
LBS	Linear-Bias Spring	14
NBS	Nonlinear-Bias Spring	14
COP	Circular Out-of-Plane	15
MFC	Macro-Fiber Composite	17
MOSFET	Metal-Oxide-Semiconductor Field-Effect Transistor	17
AC	Alternate Current	18
DAB	Dual Active Bridge	19
PID	Proportional-Integral-Derivative	20
PWM	Pulse Width Modulation	21
DCM	Discontinuous Conduction Mode	21
CCM	Continuous Conduction Mode	21
MISO	Multiple Input Single Output	34
SIMO	Single Input Multiple Output	34
LTI	Linear Time-Invariant	41
ZOH	Zero-Order Hold	41
LCR	Inductance (L) - Capacitance (C) - Resistance (R)	49

<b>List of abbreviation</b>	<b>Meaning</b>	<b>Page</b>
LPV	Linear Parameter-Varying	72
RMS	Root Mean Square	83

Table 1: Table of abbreviations.

# Chapter 1

## Introduction

### 1.1 Motivation

Dielectric Elastomers (DEs) represent a class of electroactive polymers characterized by their ability to undergo significant deformation in response to an applied electric field. These materials have attracted considerable attention in recent years due to their potential for use in a variety of advanced applications, including soft robotics, adaptive optics, and energy harvesting devices. Among the various implementations of DEs, Dielectric Elastomer Actuators (DEAs) stand out as particularly promising due to their unique combination of high energy density, large strain capabilities, and mechanical flexibility. Dielectric elastomer actuators operate on the principle of electrostatic attraction. When High Voltage (HV) is applied across a thin film of dielectric elastomer sandwiched between two compliant electrodes, an electrostatic force is generated. This force causes the elastomer to compress in thickness and expand in the planar directions, resulting in a large and reversible deformation. The intrinsic properties of the dielectric elastomer, such as its high dielectric constant and low elastic modulus, play a critical role in determining the actuator's performance. These properties enable the DEA to achieve strains of up to 100% or more, making them highly efficient in converting electrical energy into mechanical work. The importance of high voltage in the operation of dielectric elastomer actuators cannot be overstated. The electrostatic stress that drives the deformation of the elastomer is directly proportional to the square of the applied electric field. Consequently, achieving significant actuation requires the application of relatively high voltages, typically in the range of several kilovolts. This high voltage is necessary to generate the substantial electrostatic forces needed to overcome the elastomer's inherent mechanical resistance and produce the desired strain.

The main focus of this thesis is on high-voltage driving circuits, covering different aspects from design to modeling and control. The HV needed to actuate DEAs represents one of their most critical aspects. For commercial DE membranes with thickness within the range 20 - 50  $\mu\text{m}$ , such as the commercially available Wacker Elastosil®2030, the typical voltage ranges are between 1 and 3.5 kV, and up to 5 kV in some particular cases, while the current is in the order of  $\mu\text{A}$ . HV control of DEAs is usually achieved via off-the-shelf amplifiers, featuring a DC output up to 20 kV. However, such devices are generally meant for laboratory purposes, as they

are bulky, heavy, and expensive (on the order of several thousands of \$). The design of electronic components, which generate the required driving signals in a cost- and size-effective way, is challenging. Because the performance of the DEA, in terms of displacement, stroke, and energy saving, is strictly related to the applied HV, the goal of this work is to develop a voltage control algorithm for a self-designed HV driving circuit. To achieve this goal, three main aspects are required:

- **Design:** To better include DEAs in application industrial-oriented, it is of great importance that their power supply is efficient in terms of both cost and size, to be easily transported and integrated into different systems.
- **Modeling:** To understand the behavior of the HV driving circuit, including the nonlinearities of several dynamic components, and to describe the relationship between input and the high output voltage.
- **Control:** Based on a control-oriented mathematical model, to develop a feedback voltage control law for the HV circuit to improve its performance (e.g., bandwidth). The voltage controller will subsequently be integrated with a the DEA's position controller to ensure that the high-voltage driving circuit performs comparably to commercial voltage amplifiers in applications that demand precise actuator positioning, such as pumps and valves.

## 1.2 Thesis outline and contributions

The organization of the thesis and the content of each chapter are summarized.

- **Chapter 2:** In this chapter the DE material will be presented. Consequently, one of the principal applications will be introduced, namely the actuator. It will be illustrated the working principle of DEAs, and their properties, and several examples of DEA's application will be presented. Moreover, one of the main problems will be introduced, specifically the need for high voltage as the voltage source. Finally, an extensive literature review on the dielectric elastomer actuators, the state of art of HV circuits for capacitive loads, their mathematical representations and control techniques will be presented.
- **Chapter 3:** In this chapter the author will introduce the HV circuit designed to drive capacitive loads, such as DEAs. At the beginning, the major focus will be on the design of the HV circuit, which is the subject of this work's model and control algorithms. To drive capacitive loads, the circuit needs to provide high voltage to charge the load and a discharging path to allow the current in the load to flow when the voltage decreases. Therefore, the general structure of the circuit is characterized by a charging and discharging stage, which will be discussed in great detail.
- **Chapter 4:** This chapter introduces the mathematical model developed to describe the behavior of the HV circuit. In particular, the input voltage - output voltage relationship is modeled. The chapter will discuss separately the modeling of each circuit stage (charging and discharging). Later, these two

separate models will be combined into one model, which describes the switching behavior of the circuit between the charging and discharging phases. This model is referred to as *Switching model* indeed. Due to the complex nature of the model, the switching model will be then converted into an average model, to facilitate the development of control algorithms. The average model describes the circuit's average behavior during the two phases. After introducing the experimental setup, an experimental campaign to validate the model will be presented. Furthermore, these two models will be subject to validation. The work in this chapter has also been reported in conference papers [1] and journal paper [2].

- **Chapter 5:** In this chapter, several feedback control strategies for the HV driving circuit will be presented. Initially, a linearized version of the average model will be introduced to account for small voltage oscillations for feedback voltage control. The first voltage controller is a feedback control law based on the linearized model. The goal of this strategy will be to control the circuit output voltage to follow a desired trajectory up to 100 Hz, keeping the error below a certain threshold in a tracking bandwidth of interest. Since this approach is based on a linear model, it is most suitable for applications in which only small output voltage signals are needed. A nonlinear control law is necessary for applications where large-amplitude voltage signals are needed. Indeed, this chapter will continue with the development of a feedback nonlinear control strategy based on the average model. The key idea of this method is to compensate part of the nonlinearities with the controller, while dealing with residual nonlinearities via a Linear Parameter Varying (LPV) of the model. A Linear Matrix Inequality (LMI) optimization algorithm will be used to find control gains to ensure that the partially compensated closed-loop system remains stable while satisfying additional dynamic specifications. Since the controller will be defined such that it tracks the trajectory on the state  $x^*(t)$ , an observer will be developed to predict the behavior of the state by measuring the output voltage. The two controllers will be validated in simulation and via experimental campaigns. The work in this chapter is also reported in the conference paper [3] and another one which is currently in preparation and it will be submitted to IEEE Transactions on Control Systems Technology.
- **Chapter 6:** In this chapter, the linear controller developed in Chapter 5 will be applied to a case of study, namely the position control of a DEA. For this investigation, small-amplitude signals in the range of 0.2 mm will be considered as desired trajectories. The linear control law will be applied and included in an outer feedback position control scheme presented in [4]. The results will show that the circuit performance, when controlled by the combination of voltage and position control laws, is greatly improved and is comparable to the performance of an off-shelf voltage amplifier, such as an UltraVolt. The work in this chapter is also reported in the conference paper [3].
- **Chapter 7:** This chapter concludes the thesis by discussing some possible

future research directions in the area of control of HV driving circuits for DEAs.

This thesis has been developed in a collaboration between the Electrical and Information Engineering Department of Politecnico di Bari, Bari, Italy, the Intelligent Material Systems Lab and the Adaptive Polymer Systems group, both at Universität des Saarlandes, Saarbrücken, Germany. The theory and the experimental results presented in this thesis have also been reported in the author's conference papers [1, 3] and in the journal paper [2]. The conference paper [1] introduces an earlier version of the HV circuit proposed in this thesis, along with a control-oriented mathematical model. Unlike the updated design, the HV circuit in [1] lacks a discharging path for the capacitive load. The mathematical model describes the relationship between input and output circuit voltages and reformulates the switching dynamics of the electrical network in an averaged context. The accuracy of the derived dynamic model is validated through comparative simulations in *LTSpice IV*. The journal paper [2] introduces the updated HV circuit design and its improved control-oriented mathematical model. This revised design includes both charging and discharging stages, and the model captures the circuit's switching dynamics between these phases. A thorough experimental campaign validates the model's accuracy across a range of input signals with different amplitudes and frequencies, achieving a *FIT%* above 79% in all tests. The conference paper [3] explores closed-loop positioning of a DEA, where the HV driving signal is produced by the custom-designed electronics introduced in [2] and in this thesis. An inner voltage control loop enhances the precision and bandwidth of the HV circuit, while an outer position control loop is designed by modeling the controlled amplifier as a static gain. Three control architectures are then experimentally compared, in which the high-voltage command signal determined by the outer position controller is applied to the DEA via:

1. The custom HV circuit operating in open-loop
2. The custom HV circuit with an inner voltage regulation loop
3. A commercial high-voltage amplifier.

Results show that the custom-developed HV circuit in combination with an inner voltage loop represents an effective means to develop accurate and cost-effective DEA motion control systems.

# Chapter 2

## Dielectric Elastomers (DEs)

This chapter aims to introduce general concepts related to Dielectric Elastomer (DE) transducers. The class of soft material which DEs belong to will be described in Section 2.1. The principle characteristics and the field of applications will be discussed in Section 2.2. A list of several prototypes published in recent literature will be also discussed. Section 2.3 provides an overview of actuators based on DEs. Their functioning will be discussed as well as their applications and their need for high-voltage power supply. Finally, in Section 2.4, an extensive literature review will be conducted. This review will cover the description of DE systems, with a particular focus on DEAs, highlighting their advantages and disadvantages. It will also address the state of the art in high voltage circuits designed for capacitive loads, their mathematical representations, and the control algorithms developed to date.

### 2.1 ElectroActive Polymers (EAPs)

ElectroActive polymers (EAPs) are a class of materials that exhibit significant changes in shape or size when stimulated by an electric field. These materials combine the properties of polymers with the ability to perform mechanical work, making them ideal for a range of applications such as actuators, sensors, and artificial muscles. EAPs can be broadly categorized into electronic EAPs, which respond through electronic mechanisms, and ionic EAPs, which involve the movement of ions. Their versatility, lightweight nature, and ability to produce large strains make EAPs a promising area of research and development in the field of smart materials and devices. Electronic EAPs are categorized into electrostrictive elastomers, ferroelectric polymers, and Dielectric Elastomers (DEs) (Figure 2.1). Each of these EAP polymers has its own advantages and disadvantages, making them suitable for various applications. Below follows a brief description of each of them [5, 6]:

- **Ionic EAPs**

Ionic EAPs are materials that can generate displacement driven mainly by the transportation of ions or solvents, or both under electrical stimulation.

- **Polymer gels:** Their actuation principle is based on the change in gel volume, which depends on the ability of the gel network to absorb and

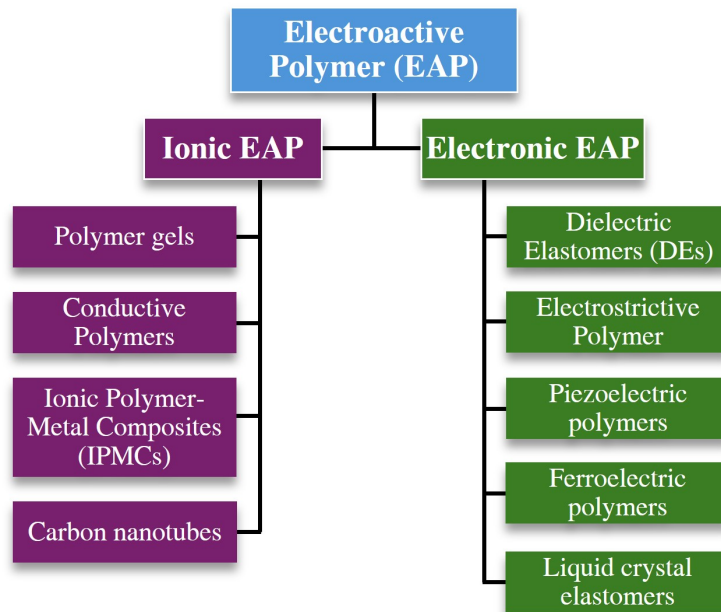


Figure 2.1: Electroactive Polymer classification

remove the solvents under electrical simulations, for instance, shape distortion.

- **Conductive polymers:** The actuation mechanism is based on the migration of ions and solvents molecules between the electrolyte and polymer during electrochemical reactions. One of their main characteristic is the low operation voltage.
- **Ionic Polymer-Metal Composites (IPMCs):** IPMCs are composed of laminated thin ionically conductive polymer film and two compliant metal electrodes. They are characterized by low working voltages, light weight, and low cost.
- **Carbon Nanotube (CNT):** Carbon nanotube-based ionic EAPs have been developed based on traditional IPMCs to some extent, to overcome the failures that characterize the traditional IPMCs, such as, large strain resistance of metal in traditional IPMC and the low combination force between the electrode and the electrolyte layer. The actuation principles are based on the unique interactions between the CNTs and the polymer matrix when subjected to an electric field.

#### • **Electronic EAPs**

Electronic EAPs material are electrically field active materials, due to the rearrangement of the electrostatic force (Coulomb force) on the polymer molecular chain to achieve the expansion and contraction of the volume in each dimension. The conversion process is a physical process, including an electrostrictive and Maxwell effect.



- **Dielectric elastomers:** DEs consist of a soft, stretchable elastomeric material sandwiched between two compliant electrodes. When subjected to an electric field, electrostatic forces compress the elastomer, causing it to expand in the plane perpendicular to the electric field. These polymers are characterized by very high deformation capability, low weight, fast response time, and high energy density. Thanks to their nature and capabilities, DEs can be used as generators, sensors, and actuators.
- **Electrostrictive polymers:** Electrostrictive polymers have similar functional properties to DEs. The distinction lies in their mechanism: Their response is determined by the alignment of electrically induced crystal or semi-crystalline structures within the material.
- **Piezoelectric polymers:** Piezoelectric polymers are materials that generate an electrical charge in response to mechanical stress, or conversely, change shape when subjected to an electric field. These polymers possess piezoelectric properties due to their internal molecular structure, which allows them to convert mechanical energy into electrical energy and vice versa.
- **Ferroelectric polymers:** Ferroelectric polymers are a class of materials that exhibit spontaneous electric polarization. After the polarization, a sufficiently large reverse electric field must be applied to reverse the polarization, which leads to a large amount of energy being consumed.
- **Liquid crystal elastomers:** Liquid crystal elastomers are advanced materials that combine the properties of liquid crystals with the flexibility of elastomers. These materials can change shape in response to external stimuli such as temperature, light, or electric fields due to their unique molecular alignment and liquid crystalline order.

## 2.2 DEs: Feature and Applications

Dielectric Elastomers (DEs) are a subclass of EAPs renowned for their remarkable ability to undergo substantial deformation when subjected to an electric field. These materials are soft, flexible, and capable of converting electrical energy into mechanical work, making them highly suitable for various applications, including actuators, sensors, and artificial muscles. Dielectric elastomers are composed of a polymer matrix sandwiched between two compliant electrodes. Common materials used for the polymer matrix include silicone, acrylic, and polyurethane, chosen for their high dielectric strength and flexibility. The compliant electrodes, often made from carbon-based materials or conductive grease, must be capable of deforming along with the elastomer without losing conductivity. A list of figures of merit of the best DE transducers is reported in Table 2.1 [7].

One of the critical advantages of DEs is their ability to generate large strains (up to 300%) and high energy densities, making them efficient at converting electrical energy into mechanical motion. This high performance, combined with their lightweight nature and relatively simple manufacturing processes, positions DEs as

promising candidates for innovative applications in robotics, medical devices, and adaptive structures as sensors, generators, or actuators.

A DE is essentially a compliant capacitor. When an external force is applied, its capacitance changes according to the geometry. Indeed, the increasing electrode area and the decreasing thickness of the dielectric cause the capacitance to increase. This principle makes the DE suitable for capacitive sensors capable of measuring displacement and force. When the membrane is deformed, the area increases, its thickness decreases, and, if the membrane is incompressible, the volume remains constant. Therefore, the overall capacitance increases. We also point out that the principle that allows the use of DEs as sensors does not depend on Maxwell stress but relies on the nature of the compliant capacitor. In [8], the capacitive sensing capabilities of a sensor based on a circular membrane DE are investigated. The proposed sensor, suitable for pump and valve applications, is experimentally validated under mechanical loading conditions. Initial results of a dual sensing and actuating DE system are also presented. In [9] DE sensor technology is applied to monitor the leg motion of a diver. The goal was to accurately measure leg joint angles thereby determining the position of each leg relative to the hip. The experimental setup and results are also presented and discussed. More recently the work in [10] presents a range of advanced designs for Dielectric Elastomer Sensors (DESs). It includes an explanation of the operational principles of these sensors, detailing their performance in terms of capacitance relative to deformation or applied load. Additionally, the paper discusses the impact of sensor design on their characteristics, highlighting methods to enhance measurement sensitivity. Among its characteristics, DE can convert electrical energy into mechanical energy and vice versa. The transduction mode employed in a DE can convert mechanical energy into electrical energy, making DEs highly suitable for use as generators. The mechanism of dielectric elastomers as generators relies on their ability to undergo significant mechanical deformation, which induces changes in capacitance and generates an electrical potential when

Property	Value		Unit
	Acrylics DE	Silicone DE	
Maximum actuation strain	380	120	[%]
Maximum actuation stress	8.2	3	[MPa]
Maximum frequency response	> 50	> 50	[kHz]
Maximum energy density	3.4	0.75	[MJ/m <sup>3</sup> ]
Maximum electric field	440	350	[MV/m]
Relative permittivity (@1 kHz)	4.5÷4.8	2.5÷3	[-]
Dielectric loss factor (@1 kHz)	0.005	< 0.005	[-]
Mechanical loss factor	0.18	0.05	[-]
Young's Modulus	0.1÷3	0.1÷2	[MPa]
Maximum electro-mechanical coupling	0.9	0.8	[-]
Maximum overall efficiency	> 80	> 80	[%]
Durability	> 10 <sup>7</sup>	> 10 <sup>7</sup>	[cycles]
Operating range	-10÷90	-100÷260	[°C]

Table 2.1: Performance of best acrylic and silicone DEs [7].

electrical charges are placed on the film. When the DE is allowed to relax, elastic stresses in the film work against electrical field pressure, thus increasing electrical energy. On a microscopic level, opposite charges on the two electrodes are pushed farther apart as the film contracts and increases in thickness, while similar charges are brought closer together as a result of the decreasing area of the elastomer, thus increasing energy density. Electrically, these changes increase the voltage of the charge, and the created energy can be harvested [11]. Moretti et. al presents an overview of DE generators, such as the design of hardware architectures, power electronics, and control, concerning the different application targets. The work [12] focuses on studying the amount of energy that can be converted by using a DE generator based on Very High Bonding (VHB) material. It shows that, by varying material parameters, energy conversion can be increased above  $1.0 \text{ J/g}$ . On one hand DE generators represent a great opportunity to develop soft, high-energy density generators, on the other they are subject to two major drawbacks: The current setups necessitate rigid frames to keep the dielectric elastomer in a pre-stretched condition, and achieving high energy densities has resulted in a shorter lifespan. In [13] those two aspects are overcome by creating a self-supporting stacked generator configuration which does not require a rigid frame. Furthermore, to ensure sustainable power generation, they introduce a mathematical model for designing the generator's electronic control, which optimizes energy output.

The generator mode is the reverse of the actuator mode. Dielectric elastomers in the actuator mode convert electrical to mechanical energy because the electric field pressure acts to exert work on the material and load. Electrically, the actuator mode brings opposite charges close together and like charges further apart as the film contracts in thickness and expands in area. The operation and characteristics of DEAs are described in detail in the following section.

## 2.3 Dielectric Elastomer Actuators (DEAs)

Among the actuators that leverage electrostatic forces to achieve large strains and high energy density, Hydraulically Amplified Self-healing Electrostatic (HASEL), DEAs, and zipping actuators are gaining more notoriety. HASEL actuators are stretchable, soft artificial muscles, with self-healing properties and muscle-like performance. They have, with  $70 \text{ J/kg}$ , greater specific energies than natural muscle, and have achieved specific powers of  $614 \text{ W/kg}$  and linear strains of  $124\%$ . HASEL actuators comprise a stretchable dielectric shell that is coated with compliant electrodes and filled with a liquid dielectric. Upon electrical activation, they expand in-plane. Two mechanisms of deformation are observed: elastic stretching of the shell and electrohydraulic “zipping”, where the electrodes progressively come together [14]. The electrostatic forces are determined by the Maxwell pressure,  $P \propto \epsilon E^2$ , where  $\epsilon$  is the dielectric permittivity and  $E$  is the magnitude of the electrical field. This pressure forces fluid into the uncovered portion of the pouch, causing this region to transition from a flat cross section toward a more circular one. Because the shell is inextensible, this transition results in linear contraction of the actuator. The theoretical maximum strain is  $\sim 36\%$  in the contracting area [15]. The activation voltage reaches values around  $8 - 10 \text{ kV}$ . Thank to their high force output and rapid

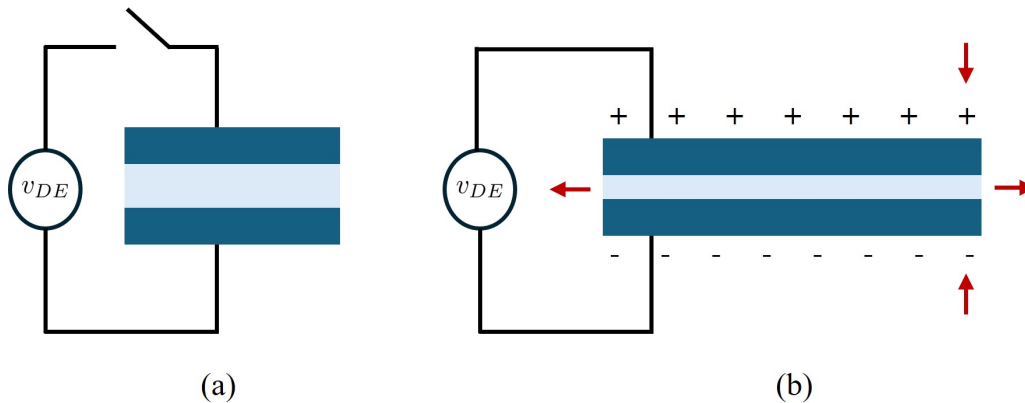


Figure 2.2: Operating principle of a DE actuator. (a) The actuator is in its initial condition since no voltage is applied; (b) Voltage  $v_{DE}$  is applied, causing the consequent area expansion and thickness reduction of the actuator.

response times, HASEL actuators are used in various applications such as artificial muscles, adaptive optics, and soft robotic systems. Among the electrostatic actuators, we can allocate the zipping actuators. This actuators consists of a single soft electrode attracted by the electrostatic force toward a fixed one. Zipping actuators allow reaching both high forces and large stable displacements at low voltages thanks to the use of a few  $\mu\text{m}$  thick high-quality rigid dielectric onto which a conducting flexure (usually silicon) is unrolled or zipped. Indeed, these actuators operate by applying a voltage across the layers, causing them to attract each other and "zip" together, resulting in precise and controlled motion. This mechanism allows for high-speed actuation and fine-tuned positioning, making zipping actuators ideal for applications requiring rapid, precise movements such as Micro-Electromechanical Systems (MEMS), adaptive optics, and haptic devices [16].

DEAs represent a promising and innovative class of soft actuators, distinguished by their lightweight, high energy density, and remarkable flexibility. At the core of DEAs is a dielectric elastomer, typically a soft polymer, sandwiched between two compliant electrodes. In this work, it is considered a DEA based on silicone membrane as soft material, namely the commercially available Wacker Elastosil®2030 [17] with a thickness of  $50 \mu\text{m}$ , and Carbon Black for the electrodes. When a voltage is applied to the electrodes, charges flow from one electrode to the other through an external circuit. The combination of attractive electrostatic forces between charges on opposite electrodes and repulsive electrostatic forces between charges of equal sign on the same electrode result in a membrane squeezing, which causes a reduction in thickness and a consequent expansion in area. The operating principle is shown in Fig. 2.2. The equivalent compressive stress induced by the electric field is known in the literature as Maxwell stress [7] and is given by

$$\sigma_{Max} = -\epsilon_0 \epsilon_r E^2, \quad (2.1)$$

where  $\sigma_{Max}$  is the Maxwell stress, which is proportional by the void permittivity  $\epsilon_0$  and the elastomer relative permittivity  $\epsilon_r$  to the square of the electric field  $E$  resulting from the application of an external voltage. The Maxwell stress' sign is

always negative as the film is being compressed. Eq. (2.1) represents the electro-mechanical transduction principle of a DE and puts also in evidence its nonlinear nature. By replacing the electric field  $E$  with the ratio between applied voltage  $v_{DE}$  and the membrane thickness  $z$ , equation (2.1) can be rewritten as follows:

$$\sigma_{Max} = -\varepsilon_0 \varepsilon_r \left( \frac{v_{DE}}{z} \right)^2. \quad (2.2)$$

From equation (2.2) it can be seen that the electrically induced stress is proportional to the square of the applied voltage. From the Maxwell stress in (2.2) a simple model for DEA can be derived [18] by assuming that the material behaves as a linear spring. The stress and the strain in the thickness direction denoted as  $\sigma_z$  and  $\varepsilon_z$  respectively, are related by

$$\sigma_z = Y \varepsilon_z, \quad (2.3)$$

where  $Y$  is the Young modulus of the material. The actual thickness  $z$  can be expressed as a function of the not-deformed thickness  $z_0$  and the thickness strain as

$$z = z_0(1 + \varepsilon_z). \quad (2.4)$$

By assuming  $\sigma_z = \sigma_{Max}$  and replacing (2.3) and (2.4) in (2.2) we obtain

$$Y \varepsilon_z = -\varepsilon_0 \varepsilon_r \left[ \frac{v_{DE}}{z_0(1 + \varepsilon_z)} \right]^2. \quad (2.5)$$

For small deformations ( $|\varepsilon_z| \ll 1$ ), equation (2.5) can be approximated to

$$\varepsilon_z = -\varepsilon_0 \frac{\varepsilon_r}{Y z_0^2} v_{DE}^2. \quad (2.6)$$

Furthermore, the thickness strain  $\varepsilon_z$  can be expressed in terms of the in-plane strain  $\varepsilon_x$  (assuming isotropic and small deformation, that  $\varepsilon_x = \varepsilon_y$ ) by using the incompressibility assumption (which is typically true for DE material) as

$$(1 + \varepsilon_x)^2(1 + \varepsilon_z) = 1. \quad (2.7)$$

If deformations are small, equation (2.7) can be approximated as

$$\varepsilon_x = -\nu \varepsilon_z, \quad (2.8)$$

where the Poisson's ratio is  $\nu = 0.5$ . The relationship between voltage and in-plane strain results then in

$$\varepsilon_x = 2\varepsilon_0 \frac{\varepsilon_r}{Y z_0^2} v_{DE}^2. \quad (2.9)$$

Equations (2.6) and (2.9) describe the basic behavior of a DEA operating in contraction ( $\varepsilon_z < 0$ ) and expansion mode ( $\varepsilon_z > 0$ ). They highlight the fact that a larger strain can be obtained for the same voltage if the material permittivity is large and both Young modulus and initial thickness are small. In practice, the thickness  $z_0$  cannot be reduced arbitrarily because doing so would increase the electric field to levels nearing the material's dielectric strength, thereby compromising system stability. Additionally, a smaller thickness would complicate the manufacturing process

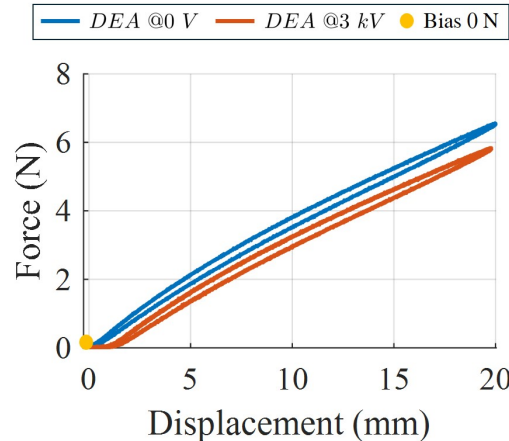


Figure 2.3: Force-Displacement characteristic of a SIP DEA.

and reduce the material's lifespan. The relative permittivity  $\epsilon_r$  and the Young modulus  $Y$  can be tuned during the manufacturing process of the material, up to certain limits. However, decreasing the material stiffness leads to less actuation force, while increasing the permittivity results in an increase of the capacitance with a consequent increment of both power requirement and electrical response time.

In the case of membrane DEAs, one possible way to increase the stroke consists of pre-loading the polymeric film with a mechanical biasing system. Moreover, it is important to mention at this point that for a DEA characterized by  $Y = 1$  MPa,  $\epsilon_r \simeq 3$  and  $z_0 \simeq 50$   $\mu\text{m}$  voltage levels of several kV are requested to achieve significantly large strain. Fig. 2.3 shows the mechanical characteristic force-displacement of a Strip In-Plane (SIP) DEA when the actuator is subjected to  $v_{DE} = 0$  V and  $v_{DE} = 3000$  kV and no bias is coupled. It represents a graphical method in steady-state to determine the actuation stroke. At equilibrium, the DE membrane force must be equal to the biasing force, therefore the intersections between the DE curves and the biasing characteristics determine the achievable stroke. When no bias is applied, i.e. no load applied, it is easy to notice that no stroke is created since the intersection between the DE curves and the bias curve is on 0 N. Instead, if the DE is loaded with a bias system, the actuator generates a certain stroke which differs depending on the bias system used. Fig. 2.4 gives an overview of a DEA system, i.e. a SIP DE loaded with a mass, a Linear-Bias Spring (LBS), and a Nonlinear-Bias Spring (NBS) respectively. If the membrane is loaded with a mass (constant force), the membrane exhibits a stroke which depends on the applied weight. As the DE curves tend to separate more as the force increases, larger masses usually lead to larger strokes. However, increasing the stroke by applying a large mass is not always an optimal approach, since larger masses require space and tend to increase both response time and oscillations. An alternative is the use of a linear spring. By tuning its stiffness and the pre-deflection, it is possible to change the slope and the offset of its mechanical characteristic, so tuning the achievable stroke. However, neither a mass nor a linear spring can exploit the large strain of the material, as the resulting displacement is usually only a small fraction of the overall deformation range. A large actuation stroke can be obtained by using an element whose mechanical characteristic fits between the DEA's curves, so an

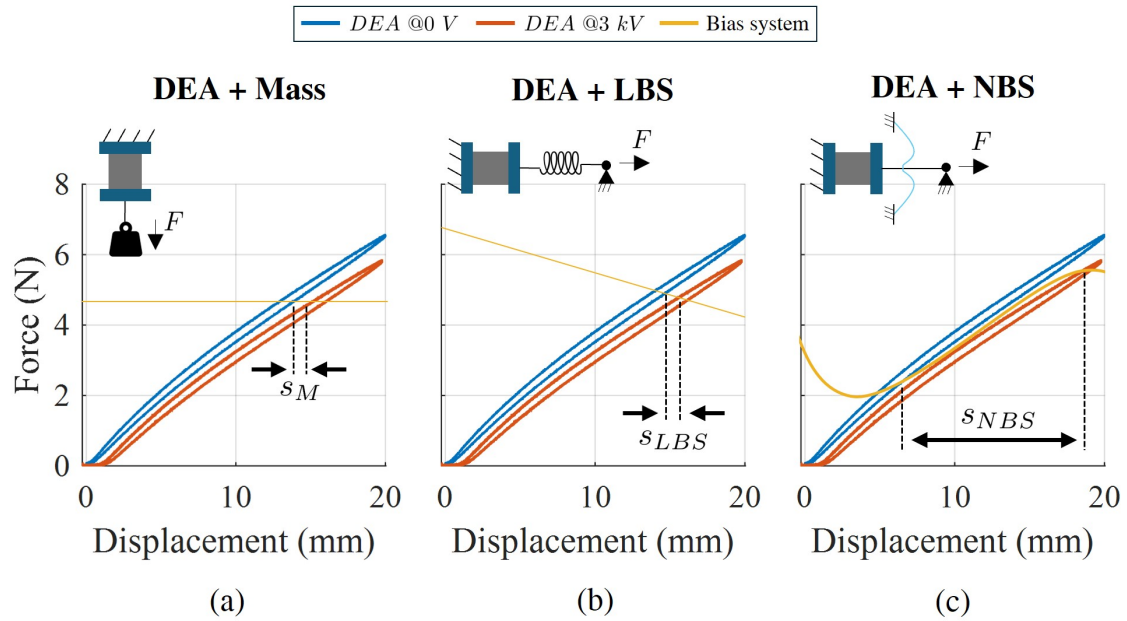


Figure 2.4: DEA performance for different kinds of mechanical biasing system. (a) Bias: Mass; (b) Linear-Bias Spring; (c) Nonlinear-Bias Spring.

element characterized by a "negative stiffness". The first model and experimental validation of such an element was made by Hodgins et al. in [19]. In this work, the NBS was coupled to a Circular Out-of-Plane (COP) DE. Later, an experimental comparison of the three different bias systems paired to a COP was carried out and presented in [20], while in [21] the system SIP + NBS is realized and characterized.

## 2.4 Literature review

This section will provide an extensive literature review on DEAs, HV circuits for capacitive loads, and the mathematical models and control algorithms developed for these systems.

### 2.4.1 Literature review on DEAs

Other than high deformation and low power consumption, the main advantages of DEAs are their flexibility and scalability, which enable the manufacturing of several actuator configurations. The actuation principle described previously for an elementary membrane can be further extended and characterized for many possible geometries, generating a large variety of actuation modes [22, 23]. Several DEA configurations have been proposed in recent literature, including diaphragm actuators [24], helical actuators [25], bimorph actuators [26], circular actuators [27], roll actuators [28], cylindrical actuators [29], out-of-plane actuators [20], rotary actuators [30], and stacked actuators [31]. Several prototypes of DEA devices have been proposed for a large variety of applications, ranging from standard industrial ones, like robots or valves, to less conventional ones, like tunable lens elements and loudspeakers. In the following, some notable examples of DEAs presented in recent literature are shortly presented.

In [32] an electronic-free dielectric elastomer oscillator driving a bio-inspired robot is presented. The robot mimics the crawling of a caterpillar and the DEAs are integrated as artificial nervous system. Thus, all functional and supporting parts of the robot are made of polymer material and carbon. The design and validation of a cone DEA driving a pneumatic diaphragm pump are presented in [33]. Compared to the pumps in literature, the proposed pump achieves the maximum pressure and flow rate while requiring at the same time the smallest amount of voltage. The work [34] presents optical lenses driven by DEA with tunable focal lengths. The authors show that this tunable lens exhibits a 29% change in focal length from 33.6 mm to 26.1 mm under a dynamic driving voltage signal. Finally, different acoustic applications have been developed based on DEA. An example of the design and validation of such actuators is presented in [35]. The high deformation capability of these actuators depends also on the applied voltage. As mentioned above, to achieve significant mechanical strokes, a high voltage of around 1 – 3.5 kV for a membrane of 50  $\mu\text{m}$  thickness is required. This latter represents the major limitation of DE technology in actuator applications.

### 2.4.2 Literature review on HV circuits

The high voltage needed to actuate DEAs represents one of their most critical aspects. For commercial DE membranes with thickness within the range 20 – 50  $\mu\text{m}$ , such as the Wacker Elastosil®2030 [17], the typical voltage ranges are between 1 and 3.5 kV, and up to 5 kV in some particular cases [36], while the current is in the order of  $\mu\text{A}$ . HV control of DEAs is usually achieved via off-the-shelf amplifiers [37, 38], featuring a DC output of up to 20 kV. However, such devices are generally meant for laboratory purposes, as they are bulky, heavyweight, and expensive (on the order



of several thousands of \$). Designing circuits for capacitive loads, such as DEAs, is demanding due to the need to manage voltage stability, reactive power, frequency response, energy losses, switching transients, and control complexity. Addressing these challenges involves careful component selection, advanced control techniques, and robust design practices to ensure reliable and efficient operation. Additionally, the design of driving circuits, which generate the required driving high-voltage signals in a cost- and size-effective way, is challenging.

In literature, many examples are given of HV circuits designed for capacitive loads, such as piezoelectric actuators, HASEL actuators, and DEAs. To enable peak-to-peak actuation of piezocomposite devices to perform shape control of structures, Bilgen et al. in [39] developed a solid-state electrical circuit employing diodes and resistors. The circuit allows a single bipolar amplifier to control a bimorph composed of two piezoceramic composite actuators known as Macro-Fiber Composite (MFC), which has an asymmetric actuation range of  $-500$  to  $1500$  V. The work characterizes the circuit experimentally, showing the input/output voltage relationship. In [40] an efficiency-improved power amplifier derived from a complementary class B stage is proposed. The circuit was developed to drive piezoelectric motors. It uses an additional capacitor to recover up to one half of the charge stored in the actuator whenever the actuator is being discharged. In the experiment, a power-loss reduction of 47% was achieved in comparison with a class B stage. Mitchell et al. in [41] present a 10-channel high voltage power supply, which independently addresses each channel up to 10 kV. The circuit is characterized by a relatively small size and low weight, and it employs a high voltage amplifier to reach such high voltage levels. An experimental campaign was carried out, where the electronic powered an array of HASELs. The output of the circuit reaches 8 kV while powering a 5 nF actuator. Moreover, an high gain converter for driving HASEL actuators is developed in [42]. The circuit topology employs a unique hybrid combination of a high-gain switched magnetic element and a diode and capacitor-based voltage multiplier rectifier to enable compact magnetic elements, and adjustable output voltage capability with simple duty-cycle modulation. The work [43] proposes and validates topologies of dual coupled inductor hybrid converters that are capable of supporting high conversion ratios up to  $\sim 2700X$  and output voltage up to  $\sim 4-9$  kV from a very low voltage supplied. It consists of two pulse current sources and a diode-capacitor-based voltage multiplier rectifier. From 3.3 V in input, it can generate an output voltage up to 9 kV.

The state-of-the-art electronics so far presented have been specifically developed for either piezoelectric or HASEL actuators, each with distinct requirements. Piezoelectric actuators typically require moderate voltages (a few hundred volts), making the associated electronics unsuitable for DEAs, which require much higher operating voltages. Conversely, HASEL actuators generally demand very high voltages, often exceeding 6 kV. In contrast, DEAs usually do not require such extreme voltage levels. In [44] a pulsed transformer gate driver is used to drive series-connected MOSFET generating up to 16 kV and 200 mA drain current. At those high voltage levels, a drastic voltage unbalance is revealed upon the MOSFETs. To overcome this problem, a balancing method using additional capacitors was proposed and validated. As proof of concept, a half-bridge bidirectional converter was designed from

this switch technology and drove an actual stacked DEA of 200  $\mu\text{m}$  at 16 kV. The realized switch can generate very high voltage at the expense of cost and size of the circuit. Indeed, the used MOSFETs are bulky and expensive compared to the price of the overall actuator. The work in [45] focuses on a novel power converter that can efficiently drive DEAs. The DC/DC high-gain boost stage achieves output voltage levels up to 600 V, which makes the circuit unusable in high-capacitance DEA. Furthermore, the specialized components and advanced external control mechanisms may lead to higher initial costs, which could be a barrier to widespread adoption in cost-sensitive applications. In [46] a linear amplifier was developed, capable of providing a high-voltage single-ended output for capacitive loads of 20 – 50 pF. The circuit consists of a ladder of twelve high-voltage MOSFETs controlled analogically. Small-signal performances (input signal of 10 mV) are examined for a load equal to 50 pF, showing the capability of the circuit of generating an output voltage with a gain that varies only by  $\pm 0.5$  dB around the value of 50 dB up to 1 MHz. Despite those satisfactory results, this circuit presents some limitations. Above all, distortions in the signal are evident for higher values of high voltage and the losses generated by the high-voltage MOSFETs cannot be neglected. For more industrial applications, S. Schlatter et al. [47] developed the so-called "Peta-pico-Voltron", a low-current high-voltage power supply for DEAs. The electronic can generate up to 5 kV in DC and AC mode with a frequency range between 1 mHz and 1 kHz. The main protagonists of this electronic are the EMCO module used as high-voltage DC-DC converter and the optocouplers as fast output switch. Thus, it is evident that the cost of the electronic is 100 times more than the actuator. Generally, it is a common practice to use transformers on high-voltage circuits to ensure electrical insulation capabilities, AC operation modes, and high-frequency applications. In [48], the author presents a current-fed push-pull parallel inverter specifically tailored for efficiently driving capacitive loads. The key aspects of this work include the development of a sinusoidal power source that can automatically adjust its parameters to maintain optimal performance, even when the load characteristics change. The power source can dynamically adjust its output to adapt to variations in the capacitive load, ensuring consistent performance and efficiency. The self-adjusting mechanism and control algorithms add complexity to the design and implementation of the power source. This complexity can make the system more difficult to design, build, and troubleshoot. For applications where high power is required, R. P. Massey et al. developed in [49] a DC-DC single-ended half-wave transformer-coupled converter. The circuit can generate 130 Watt at 1800 V with an efficiency of 82 %. The disadvantage of this electronic is the lack of an active discharging path for the load. Indeed, the only path is a high-ohmic resistor.

The most common configuration for high-voltage circuits is the Flyback converter, since it guarantees electrical insulation as well as the generation of high-voltage with a minimal number of components. In [50] a high-voltage DC-DC converter topology for bi-directional energy transfer between a low-voltage DC source and a high-voltage capacitive load is described. The circuit can convert 24 V into 2.5 kV and discharge it to 0 V. The converter operates with 80 – 85 % charging and 70 – 75 % discharging energy efficiency. The downside is the high-voltage 4 kV MOSFET. This latter is quite delicate, thus a careful design of the circuit is required

to avoid damaging the MOSFET, and the cost of such a component is not negligible. The work of Mottet et al. in [51] shows that a design reducing key parasitic capacitances of the coupled inductor combined with the use of stacked MOSFETs on the secondary side of a bidirectional flyback allows the converter to supply 7 kV to a capacitive load from a 12 V power supply. The power stage has been experimentally validated while driving a planar DEA of around 2.4 nF. It shows that it is possible to reach the 7 kV with a rising time of 7.5 ms and efficiency of 58 %, and back to 0 V with a falling time similar to the rising and efficiency of 54 %. The problem of this electronic is the amount of noise in the output signal. It is shown a noise level of 600 V over 4 kV, probably due to the switching behavior of the stacked MOSFETs.

### 2.4.3 Literature review on modeling of HV circuits

High voltage circuits presented in literature still face several unresolved challenges. One significant issue is generating high voltage while maintaining a compact and cost-effective design. Many current solutions require large, expensive components that are not suitable for applications where space and budget constraints are critical. Additionally, the quality of the output signal often suffers from excessive noise, which can impair the performance and precision of the actuators. This noise issue is particularly problematic in applications requiring smooth and accurate actuation. Moreover, the complexity of existing HV circuits is another open problem. These circuits often involve intricate designs and numerous components, leading to increased chances of failure and making them difficult to troubleshoot and repair. As a result, there is a clear need for simpler, more robust high voltage circuit designs that can provide clean, stable signals and provide an adequate discharging stage for the load, both without significantly increasing size or cost. Addressing these issues is essential for advancing the practical use of DEAs.

In literature, many mathematical models have been developed for different high-voltage circuit topologies. The work in [52] presents a Hamiltonian representation of different switching power converters, including boost, buck, and flyback converters. In [53] a Dual Active Bridge (DAB) and its mathematical model representation are presented. The circuit contains two full-bridge semiconductor circuits in H-configuration connected through a transformer and an inductor. The developed model predicts the circuit's behavior at each switching period, assuming the phase shift of the current in the DEA as input and the average value of the same current as output.

Among all the circuits introduced in the literature, the closer in design to the HV circuit proposed in this work is the flyback converter. Therefore, more attention is given to the modeling approaches of this circuit. An analytical switching cycle modeling of a bidirectional high voltage flyback converter for capacitive load is developed in [54]. The circuit presents a charging and a discharging stage modeled separately. First, an estimated model is achieved, by neglecting the effect of core loss of the transformer. Afterwards, an accurate model that includes the effect of core loss and the parasitic elements is developed. The analytical model well represents the behavior in one switching cycle for both the charging and discharging stages. Finally, the models have been separately experimentally validated. Other

examples of modeling analysis of flyback converters are given by [55, 56]. The authors present two different equivalent models of flyback transformer, based on the mechanism that the primary and the secondary currents of the converter do not appear at the same time. The analysis is developed in both continuous conduction mode and discontinuous conduction mode. An equivalent model of the transformer is used for theoretical calculation as well as for simulations. The models have been validated in simulation and experimentally. Ravi et al. in [57] present an energy-based model for a flyback converter feeding a resistive load. It is known that one of the dominant factors that influence these converters' operation is the parasitic capacitance since a significant portion of the input energy is utilized in charging the parasitic capacitances of the circuit, which is circulated back to the source at the end of every switching cycle. This energy transfer phenomenon involving parasitic capacitances results in less energy reaching the load in every cycle. The model proposed by the authors includes parasitic capacitances and exploits the latter to achieve zero voltage switching, thus minimizing the turn-ON loss. The model is validated in simulation and experimentally for resistive loads.

Besides the switching mathematical representation of those circuits, other models have been developed based on different techniques, such as averaging and linearization. The work in [58] presents two average-value models including the conduction losses and using the circuit averaging and the state space averaging approaches, respectively. The models are verified for large signal time-domain analysis transients and small-signal frequency-domain analysis in continuous and discontinuous conduction modes. In [59] an average model of a flyback converter is developed only for continuous conduction mode. In [60] a dynamic model for a single-stage single-switch parallel boost-flyback converter is developed by the linearization of its large signal equations. The author will overcome the modeling uncertainty due to the variation of the operating point of the circuit by controlling the system in closed-loop. Irving et al. presented in [61] a small-signal model of a variable-frequency flyback converter. An average model is first developed and then linearized by considering only ac-signals contribution in the average model equations. Another example is given in [62], where a small-signal model is derived for a second-order flyback converter.

Although modeling of high voltage driving circuits for DEAs has been addressed in the literature, no author has investigated control-oriented modelling of the circuitry here proposed, to the best of our knowledge.

#### 2.4.4 Literature review on control of HV circuits

As DEAs exhibit complex nonlinearities, feedback controllers are useful to handle these complex phenomena. In literature there are several examples of controllers developed to improve the operation of DEAs.

In [63], a Proportional-Integral-Derivative (PID) closed-loop voltage control system with quasi-digital characteristics is designed to regulate the actuation voltage of a DE actuator constructed from 3M VHB 4930. The feedback control system integrates an embedded sensing mechanism to measure capacitance and current inputs derived from the actuation signal output. This quasi-digital PID control method effectively oversees the analogue/Pulse Width Modulation PWM applied voltage

to precisely manage the voltage across the DEA. Experimental validations confirm the feasibility of using the DE actuator in practical applications. In their work on a positioning system based on DEAs in [64], Rizzello et al. formulate a detailed nonlinear model that accurately characterizes the intricate dynamics of the system. Subsequently, the research proposes a model-based controller tailored specifically to achieve precise tracking of step signals across a spectrum of amplitudes. Central to their controller design is a novel nonlinear PID configuration, which represents a fusion of a conventional linear PID controller cascaded with a square root term. This innovative structure is strategically devised to effectively mitigate the inherent nonlinearities of the actuator's response, influenced by the quadratic nature of the applied voltage. In their pursuit of converter control, the study in [65] introduces a PWM controller tailored for a flyback converter predominantly operating in Discontinuous Conduction Mode (DCM). The controller's parameters are meticulously tuned to steer the converter towards critical conduction mode operation. Central to this approach is the strategic utilization of high and low power pulses to achieve precise regulation of the output voltage. In [66] and [67] a primary side control for flyback converters is realized. The first developed a primary side control suitable for both discontinuous and continuous conduction modes. The controller is implemented on micro controller. The second work presented a constant current digital control method for an active-clamp flyback converter. The converter operates in DCM mode, employing a modified active-clamp technique to achieve soft-switching. Addressing nonlinearity in secondary diode current via primary-side regulation, the paper introduces an output current estimation algorithm based on the charge balance principle. The work in [68] and [69] proposed a digital control scheme for bidirectional flyback converter. Xu et al. in [68] developed a digital controlled sampling method to sample the output voltage in DCM and Continuous Conduction Mode (CCM). The algorithm is based on a digital ramp sampling method and it aims to the improvement of constant voltage accuracy. In the work [69] a digital controller is developed to improve the efficiency and charge/discharge speed using the valley switching technique during both charge and discharge process. The work [70] outlines a detailed design of a sliding-mode controller for flyback converters, emphasizing the formulation of the sliding surface and the development of tests for transversality, reachability, and equivalent control. The controller's design integrates considerations such as perturbation magnitude, period, and maximum switching frequency. Moreover, to ensure the attainment of the reachability test, a filter is incorporated into the design process to limit this derivative. In [62] a sliding mode controller is designed to regulate the output voltage of DC-DC flyback converters in response to line, load and set point variation. The controller is implemented using voltage and current error to get regulated output voltage and better dynamic response. The closed-loop system is validated in simulation and results show that the sliding mode controller provides regulated output with low steady state error. Hoffstadt and Maas in [71] utilizes the flyback converter's unique capability of providing nearly constant power for charging and discharging purposes, employing a sliding-mode control strategy for position control. Initially, a two-point controller is developed and later expanded into a three-point controller with hysteresis to notably reduce switching frequency. To enhance control performance and energy efficiency

further, an adaptive approach is implemented for inner power converter control, adjusting the hysteresis thresholds of the three-point controller accordingly. Experimental validation using a prototype silicone DE stack actuator and bidirectional flyback converter confirms that the adaptive three-point controller achieves high dynamics and accuracy with increased efficiency, thanks to significantly minimized switching frequencies.

In this work, we present a novel HV driving circuit for DEAs composed of two stages, namely the charging and discharging stages. The first consists of a resonant converter and a Greinacher doubler-rectifier element coupled via a transformer. Each stage is described in detail in Chapter 3.1. To predict and optimize the DEA system's behavior under various operating conditions, developing a mathematical model for the driving electronic is crucial. This enables precise control strategies to be implemented, ensuring the actuator's performance is accurate and consistent.

# Chapter 3

## High Voltage circuit (HV circuit)

This chapter will introduce and discuss the developed HV driving circuit for DEAs. A general description of the circuitry design will be given in Section 3.1. Following, Sections 3.2 and 3.3 will describe in detail the circuit stages, namely the charging and discharging stages, respectively. The design of the circuit is reported in the conference author's paper [1].

### 3.1 Circuitry design

In this section, the design of the proposed HV circuit is discussed. To effectively amplify a low-voltage DC input of 0 - 6 V by a factor of 500, and send the resulting signal to the DEA, a DC-DC converter concept is required, ensuring a charging and discharging path for the capacitive load. Figure 3.1 and 3.2 show the schematic and a picture of the discussed HV circuit, respectively. The circuit specifications are the followings:

- Input voltage: 0 to 6 V DC
- Input power: up to 0.12 Watt
- Control input signal: Two PWM signals, one aimed to control the charging stage, the second to control the discharging stage
- Output voltage: 0 to 3000 V
- Output current: up to 200  $\mu$ A
- DC-DC gain: 500
- Noise level: 1% over 3000 V
- Open-loop bandwidth: up to 40 Hz
- Dimensions: 130 mm  $\times$  50 mm
- Weight: 48 g

The PWM signals are generated via microcontroller and enable to drive the circuit with only DC low-voltage and control it digitally. Indeed, the PWM signals modulate at 15 kHz the input trajectory, i.e. modulating signal, ensuring that the output voltage follows the desired pattern. The circuit consists of a cascade of a charging and a discharging stage. A microcontroller interface, consisting mainly of a half-bridge driver, is needed to power and control the circuit. Indeed, the stages can be switched on and off by the microcontroller interface and a transistor  $T_3$  driven by the two complementary PWM signals. The charging stage includes a resonant converter and a doubling-rectifying circuit, denoted as Greinacher circuit, coupled together through a three-coil transformer  $TR$ . This topology has the advantage of modularity since more stages of Greinacher circuit can be included, giving the possibility of reaching theoretically any output voltage. In this work only one Greinacher circuit is considered, making the maximum achievable output voltage equal to 3000 V. The transformer has a primary coil made by the two coils,  $L_{p1}$  and  $L_{p2}$ , on a common core, a secondary coil,  $L_s$ , and a feedback coil,  $L_{fb}$ . Between  $L_{p1}$  and  $L_{p2}$  a center tapping provides the supply to  $TR$ . The turn ratio between the primary and secondary coil is  $1 : n_s$ , with  $n_s = 100$ , while it is  $1 : n_{fb}$ , with  $n_{fb} = 0.25$ , between the primary and feedback coil. The discharging stage is realized by the series of 6 medium-voltage MOSFETs,  $M_1, \dots, M_6$ , followed by a transistor,  $T_3$ , which allows the DEA current to flow in a low ohmic resistor so that the discharging time becomes small (on the order of  $\mu s$ ). The two PWM signals driving the two stages must be perfectly synchronized and complementary, to avoid the discharging and charging stages leading simultaneously and the DEA would not have enough current to reach the desired voltage.

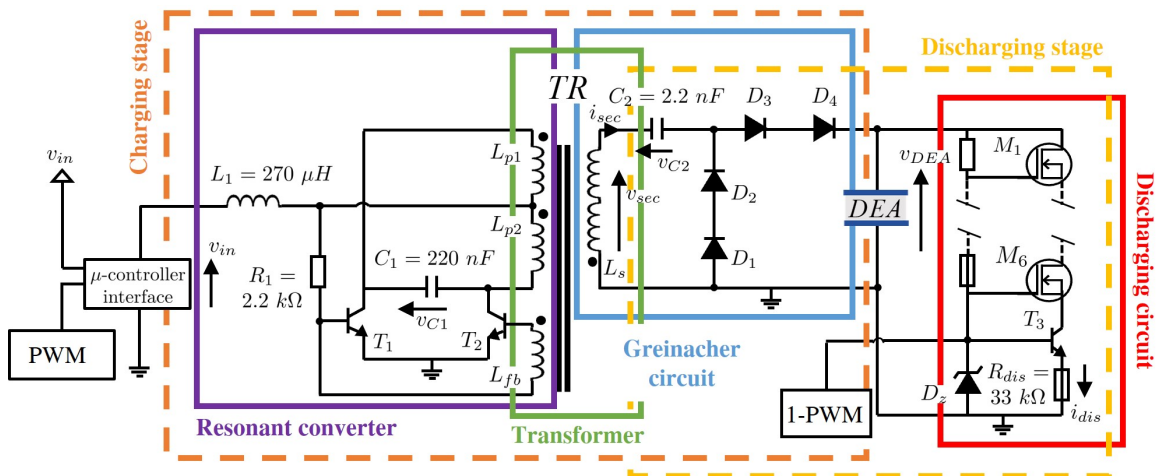


Figure 3.1: High voltage circuit schematic

The basic principle of this HV circuit is the charging and discharging of the capacitive load, namely the DEA. The corresponding stages are shown in Fig. 3.1: the charging stage in the orange dashed box, while the discharging in the yellow dashed box. It is important to note that those two stages can never simultaneously lead. On the contrary, they must be perfectly synchronized to ensure the correct generation of the high voltage without creating current loops. This is guaranteed by the signals PWM and 1-PWM.



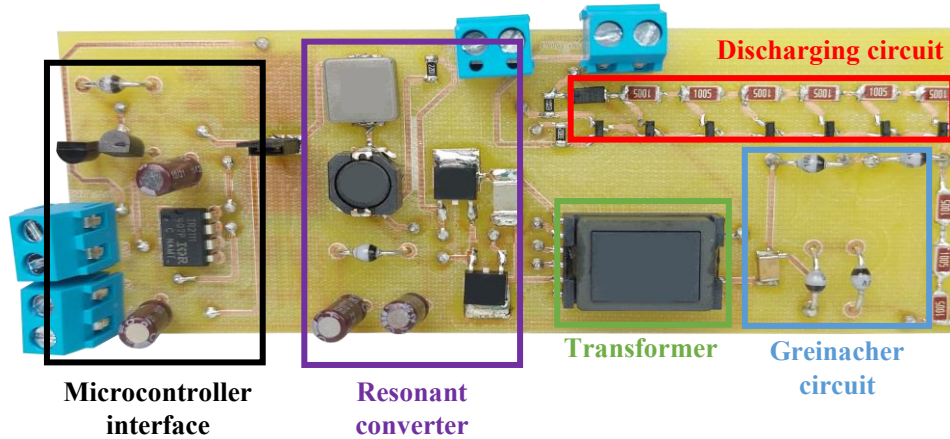


Figure 3.2: High voltage circuit

Compared to the HV circuits in literature, the proposed HV circuit provides a charging and a discharging path for the load, maintaining the number of components and the size, as well as the cost, of the circuit very low. Thanks to the combination of resonant converter, transformer, and voltage doubler and rectifier circuits, the electronic is characterized by a high gain. In addition, its modular structure allows to reach higher voltage (up to 4500 V), by adding few components. Furthermore, the microcontroller interface allows the possibility to control the circuit digitally.

## 3.2 Charging stage operating principle

The HV circuit is designed ad-hoc to drive capacitive loads, such as DEAs. Therefore, it is important to charge the load efficiently to decrease the losses. Thus, this work proposes a combination of a resonant circuit and a voltage doubler-rectifier circuit, connected via a three-coil transformer. During the charging phase, the PWM signal on the half-bridge driver is high, while the complementary signal 1-PWM is low.

### 3.2.1 Resonant circuit

A resonant circuit, also known as a tuned circuit, is an electrical circuit that consists of inductance and capacitance connected to allow the circuit to oscillate at a particular frequency, called the resonant frequency. The resonant circuit in question, shown in Fig. 3.1 in the violet box, is a parallel of the capacitor  $C_1$  and the primary side of a three-coil transformer  $TR$  on a common core. The primary coil has a center tapping that provides the power supply to  $TR$  and divides the coil into two parts,  $L_{p1}$  and  $L_{p2}$ . The resonant circuit is characterized by the following resonant frequency

$$f_r = \frac{1}{2\pi\sqrt{L_p C_1}}, \quad (3.1)$$

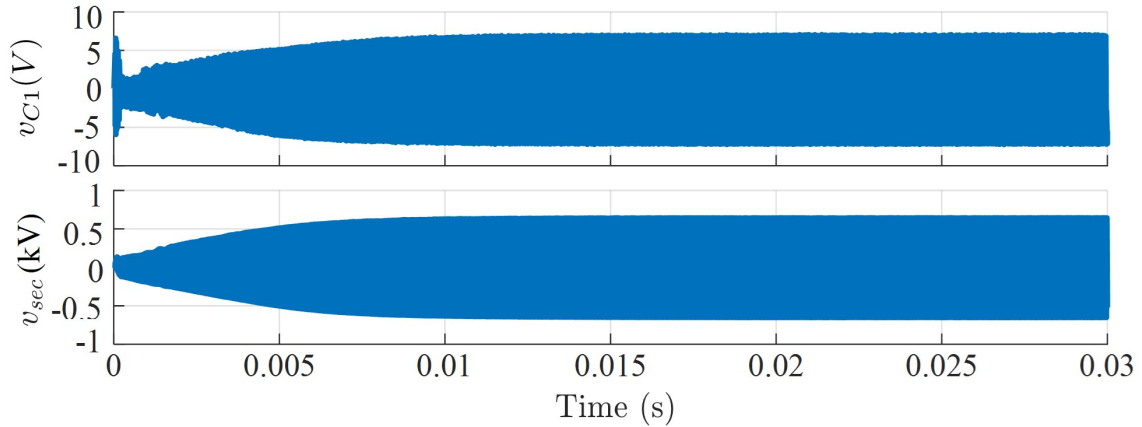


Figure 3.3: Behavior of the resonant circuit's main quantities of interest during the charging phase.

with  $L_p = 2L_{p1} + 2L_{p2}$ . The input current, which is filtered by the input inductance  $L_1$ , is minimum at the resonant frequency, as most of the current flows through the inductance and capacitor branches. At resonance, the impedance of a parallel resonant circuit is at its maximum, while below and above the resonant frequency, the impedance decreases, and the current increases. The voltage drop over resistor  $R_1$  and the small voltage over the feedback winding, induced accordingly to the turn ratio primary-feedback coil 1 :  $n_{fb}$  with  $n_{fb} = 0.25$ , trigger the two transistors  $T_1$ , and  $T_2$ , thus keeping the circuit in resonance. Therefore, the two transistors work alternately. When the oscillation circuit is activated, the resulting sinusoidal voltage on the capacitor  $v_{C1}$  is transferred to the secondary side according to the corresponding turn ratio primary-secondary coil 1 :  $n_s$  with  $n_s = 100$ , generating the voltage  $v_{sec}$ . The voltage overshoot, as well as the frequency and the current within the resonant circuit mainly depends on the pairing of coil and capacitor. A small capacitor results in a higher voltage overshoot and therefore generates a higher output voltage, but also a lower output current. In reverse, a large capacitor results in a lower output voltage, but is capable of driving higher loads. This concept only requires five components, thus keeping the system complexity low. In Fig. 3.3 a simulation of the resonant circuit during the charging phase is reported, showing the behavior of  $v_{C1}$ , and  $v_{sec}$  when an input voltage  $v_{in} = 3$  V is applied. Such a simulation was made in the *OrCAD Capture* software.

### 3.2.2 Greinacher circuit

The voltage generated at the secondary side of  $TR$  cannot be directly applied to the DEA for two main reasons:

1. The amplitude of the signal does not fall within the useful voltage range for driving DEAs. Indeed, they need mainly a supply voltage between 1 – 3.5 kV.
2. The signal frequency is too high. To appreciate the movement of the actuator, the frequency should be below a couple of kHz.

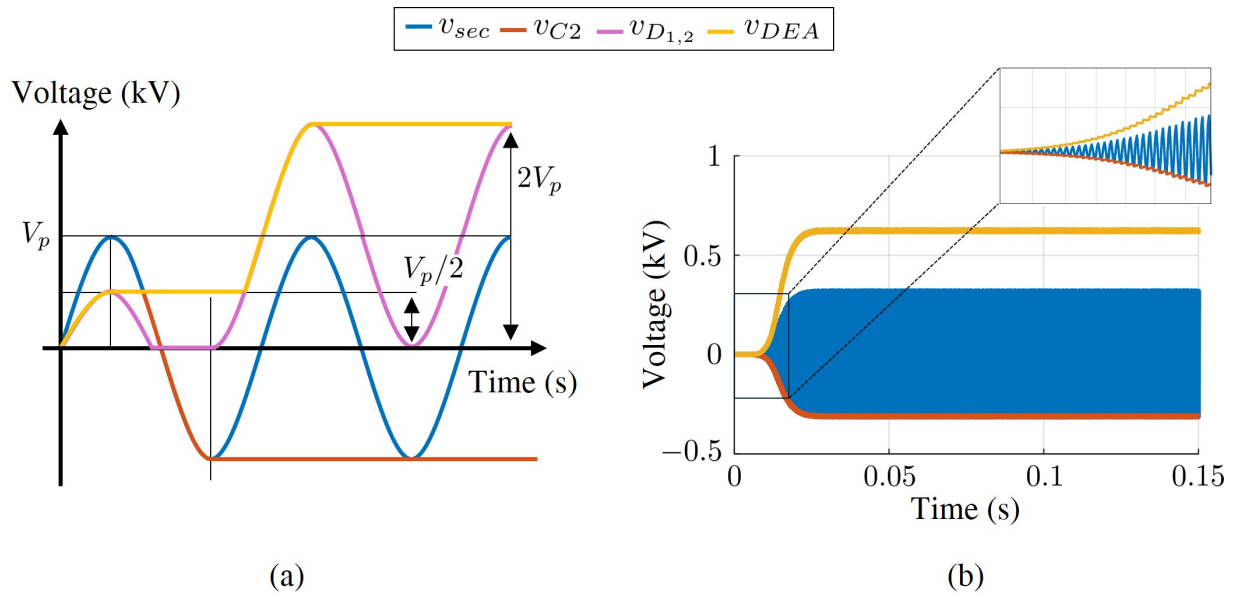


Figure 3.4: Greinacher circuit. (a) Qualitative behavior; (b) Simulation results.

For those reasons, it is necessary to rectify and double the voltage  $v_{sec}$ . This work exploits a particular design called the Greinacher circuit, shown in Fig. 3.1 in the blue box. This circuit consists of diodes and capacitors. In the case of study of this thesis, the second capacitor is exactly the DEA. Furthermore, SF1600 high-voltage diodes are used; since the breakdown voltage of those diodes is 1600 V, they are placed in series to handle the 3000 V needed by the actuator.

The input voltage is the output voltage of the resonant circuit, so the alternating voltage  $v_{sec}$ . During half the positive half-wave of the input voltage,  $D_1$  and  $D_2$  remain off while  $D_3$  and  $D_4$  conduct. The input voltage is divided between the two capacitors in equal parts. During the second half of the positive half-wave, the input voltage decreases:  $D_3$  and  $D_4$  remain off and the two capacities remain charged at  $V_p/2$ . As long as the input voltage is greater than the voltage at  $C_2$  capacitor heads,  $D_1$  and  $D_2$  are off-limits. As soon as the input voltage is equal to the value of the voltage at the capacitor  $C_2$ ,  $D_1$  and  $D_2$  conduct. The voltage  $v_{C2}$  follows the input voltage until the first half of the negative half-wave. After passing the first negative peak of the input voltage,  $D_1$  and  $D_2$  polarize inversely and the voltage on  $C_2$  is  $v_{C2} = -V_p$  and  $v_{D_{1,2}} = v_{sec} + V_p$ . Finally, after the second positive peak,  $v_{sec} = V_p$ , the output voltage  $v_{DEA}$  remains permanently anchored to the value  $v_{DEA} = 2V_p$ . The qualitative behavior of  $v_{C2}$ ,  $v_{D_{1,2}}$  and  $v_{DEA}$  is shown in Fig. 3.4 (a), while simulation results are shown in Fig. 3.4 (b). To better appreciate the qualitative shape of the circuit response, a resonance frequency  $f_r = 6.62$  kHz was chosen for simulation purposes only. To achieve such a frequency, parameter  $C_1$  was chosen equal to 12 mF, since the value of  $L_p$  is strictly dictated by the choice of the transformer (cf. equation (3.1)). It is pointed out, however, that the true value of the resonance frequency used in the circuit is equal to  $f_r = 54$  kHz.

### 3.3 Discharging stage operating principle

When the load of a circuit is capacitive, it is important to guarantee a discharging path for the load itself. Among the many reasons that explain the importance of a discharging stage, the ones more outcoming involve energy saving. Indeed, the leakage current of the DEA can result in gradual energy loss over time without a discharge path. A controlled discharge path helps manage and mitigate this leakage. Furthermore, in power supply circuits, appropriately discharging capacitors can help improve energy efficiency by ensuring that energy is not wasted.

The discharging stage presented in this work (Fig. 3.1, yellow dashed box) consists of the combination of the Greinacher circuit and a discharging circuit. The input voltage of this stage is  $v_{sec}$ , which is considered equal to 0 since the charging and discharging stages cannot lead at the same. There are two possibilities for unloading a capacitor, passively or actively. Both are better described below.

#### 3.3.1 Passive discharging circuit

Passively discharging a capacitor means providing a high-ohmic path for the current to go through so the load can discharge itself. In this case, a high-ohmic resistor is the easiest choice, placed in parallel to the load. A high value of the resistance is necessary to avoid the flow of unwanted currents during the charging phase of the load. Despite the easy implementation, this solution does not allow for control of the discharging time of the load, thus the name "passive". Indeed, the discharging time is dictated only by the capacitance value of the load and the value of the resistor. The higher the resistance, the less current would flow in during the charging phase but the greater the discharging time constant. In this work, a discharging resistor  $R_{dis,p} = 30 \text{ M}\Omega$  is considered. For a DE with nominal capacitance  $C_{DEA} = 600 \text{ pF}$  (usually the capacitance of a one layer DE  $30 \text{ mm} \times 30 \text{ mm} \times 50 \text{ }\mu\text{m}$ ), the resulting discharging time constant  $\tau_{dis}$  is

$$\tau_{dis} = R_{dis,p}C_{DEA} = 0.018s. \quad (3.2)$$

With this value of  $\tau_{dis}$  a working frequency bigger than 20 Hz would be quite difficult to achieve. Fig. 3.5 shows the design configuration and a simulation result of a passive discharging circuit. It is taken into account that the PWM signal at  $T_3$  switches high at  $t = 0.1 \text{ s}$ .

#### 3.3.2 Active discharging circuit

To be able to control the discharging time of the actuator, an active discharging circuit is necessary. The active discharging circuit exploited in this work is shown in Fig. 3.1 in the red box. The discharging circuit is realized by the series of six HV MOSFETs,  $M_1, \dots, M_6$ , whose breakdown voltage is 600 V. Each MOSFET is activated by the current provided by the  $10 \text{ M}\Omega$  resistors at their gates. Following the cascade, there is a small-signal transistor,  $T_3$ , which allows the DEA current to flow in a low-ohmic resistor  $R_{dis}$ .

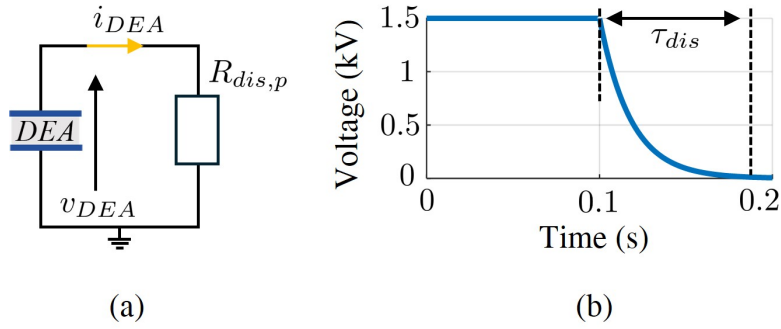


Figure 3.5: Passive discharging circuit. (a) Circuitual configuration; (b) Simulation result.

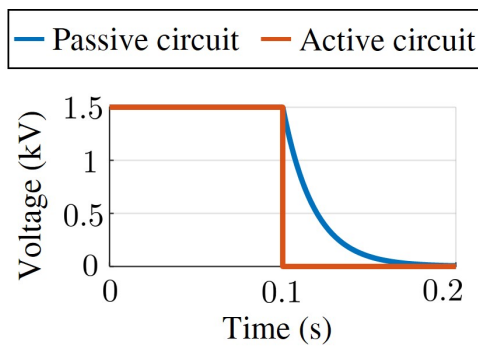


Figure 3.6: Discharging time comparison in simulation.

When the PWM signal on the half-bridge driver is low, so the 1-PWM signal on  $T_3$  is high, the charging stage ends and the discharging process is triggered. Such a process is essential in case  $v_{DEA}$  needs to be quickly decreased. During the discharging phase, the resistor  $R_{dis}$  regulates the constant amount of drained current,  $i_{dis}$ , computed as

$$i_{dis} = \frac{v_{D_z}}{R_{dis}}, \quad (3.3)$$

where  $v_{D_z} = 15$  V is the voltage on the zener diode  $D_z$ . For  $R_{dis} = 33$  k $\Omega$ , considering the same DE's capacitance as above, the discharging time constant is now  $\tau_{dis} = C_{DEA}R_{dis} = 0.198$  ms, which is  $10^3$  times less than in the case of a passive discharging circuit. Figure 3.6 presents a comparison of discharging times for both passive and active discharging circuits.

# Chapter 4

## Modeling

To control the HV delivered to the DEA in a fast and precise way, model-based closed-loop control plays an essential role. For this reason, a control-oriented dynamic model will be developed in this work to describe the relationship between the low-voltage input signal and the HV output during both the charging and discharging phases of the DEA. The developed model will open up feedback control strategies to tightly regulate the HV signal delivered to the DEA. The development of a model which is accurate but also simple enough to be used in real-time implementations is highly challenging, due to the presence of nonlinear and switching components. Firstly an overview on the modeling problem will be presented, Section 4.1. Secondly, in Section 4.2, two models (i.e., one for the charging stage and one for the discharging stage) will be developed and combined in a single *switching model*. An average model will later be developed and presented in Section 4.3. Finally, the models will be validated in simulation in Section 4.4 and via an extensive experimental campaign in Section 4.5, showing a high accuracy over a wide range of input frequencies (0 – 100 Hz). The theory and results presented in this chapter are reported also in the author’s conference paper [1] and journal paper [2].

### 4.1 Modeling problem statement

As the circuit model developed in this thesis will be primarily used for control applications, it will naturally be described in terms of a set of differential equations in state-space form. The model equations will relate the modulated input voltage  $v_{in}$  to the output voltage  $v_{DEA}$ . A black box representation of the model is shown in Fig. 4.1. In this thesis, the focus is on modeling the circuit, taking into account the nonlinear behavior of dynamic components. As the model is based on state-

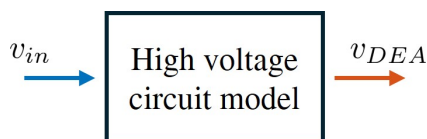


Figure 4.1: General structure of the high voltage circuit model. Input is colored in blue, output in red.

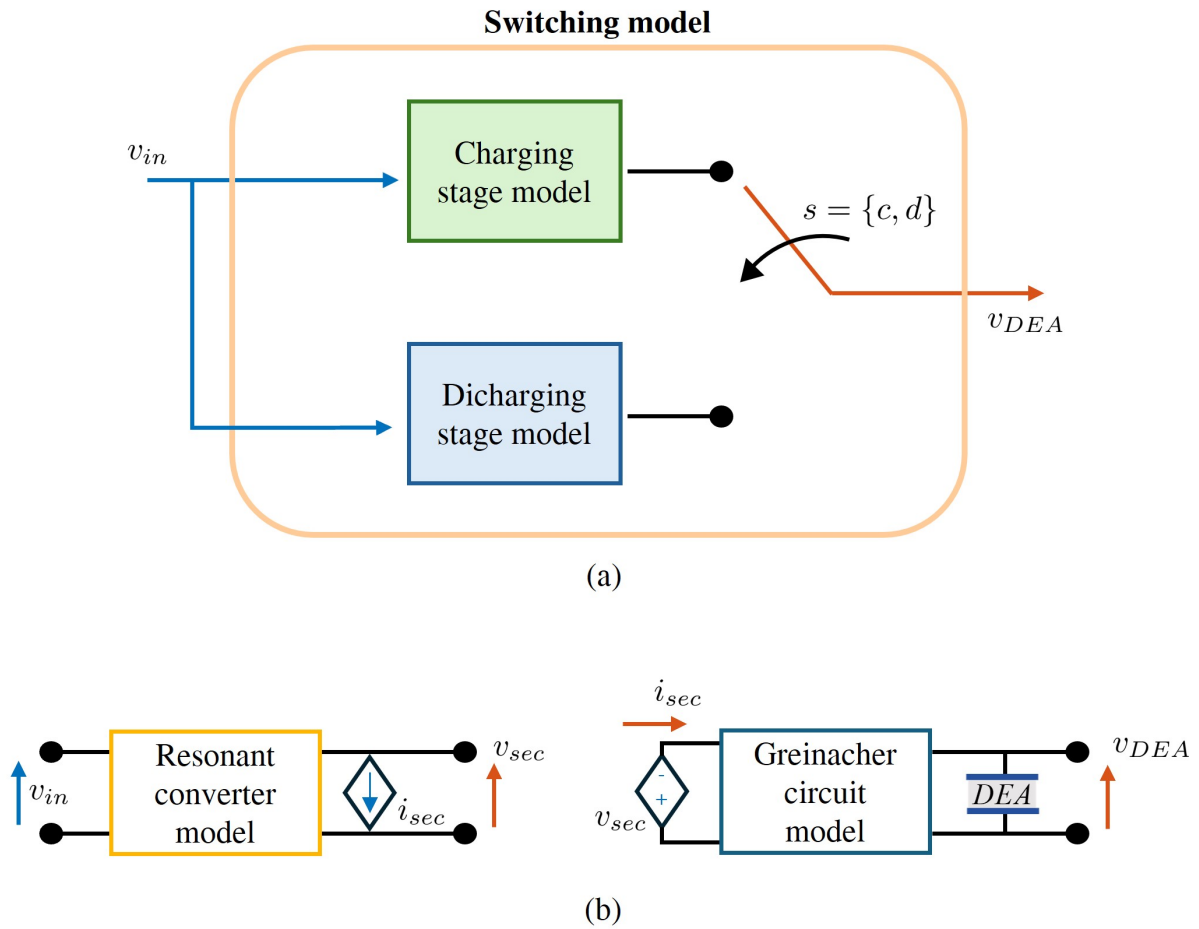


Figure 4.2: Block diagrams. (a) Block diagram of the switching model, in blue the input and in red the output; (b) Block diagram of the charging stage model, in blue the inputs and in red the outputs.

space representation, it is naturally described in terms of some state variables which characterize the internal behavior of the circuit. Figure 4.2 (a) shows an example of a block diagram of the circuit model. The model named the switching model for the switching nature of the circuit consists of an alternated combination of the charging stage and discharging stage models. The variable  $s = \{c, d\}$  represents the switching variable, where  $c$  and  $d$  stand for charging and discharging respectively. In Fig. 4.2 (b) the block diagram of the charging model is shown. It embodies the resonant converter and the Greinacher circuit models via external and internal inputs and outputs. More detail on this latter model will be discussed in 4.2.2.

## 4.2 Control-oriented model

In this section, a control-oriented dynamic model of the proposed circuit will be developed. First, based on the equivalent circuit schemes of the dynamic components, the state-space models describing the DEA charging and discharging phase will be derived as two separate systems. Both models have  $v_{in}$  as input and  $v_{DEA}$  as

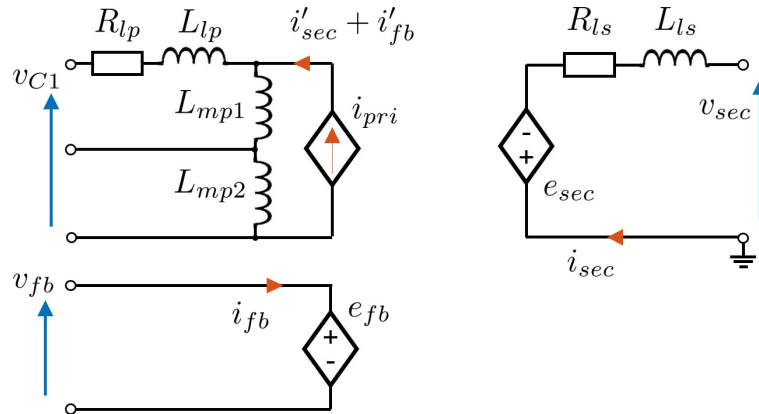


Figure 4.3: Equivalent model for the three-coil transformer.

output. Then, the two models will be combined in a *switching model*. This mathematical model will be developed for future feedback control applications, in which we aim at regulating the output voltage  $v_{DEA}$  to an arbitrary reference value. This, in turn, will make the developed electronic operate as an ideal voltage source, thus enabling the implementation of accurate motion control strategies, e.g., as in [4]. In this work, the DEA capacitance is considered as a varying parameter for the model.

### 4.2.1 Equivalent components models

The author includes equivalent models of the dynamic components to focus on the key characteristics that impact system performance. Using equivalent models simplifies complex components into more manageable forms, making analyzing and understanding the overall system easier. Furthermore, accurately representing each component makes the behavior prediction more reliable and realistic. These equivalent models will be also used in the simulation environment, making the analysis more efficient and faster. The models of dynamic elements, i.e. transformer  $TR$ , transistors, diodes, and MOSFETs, are described below.

#### Transformer equivalent model

Fig. 4.3 shows the equivalent model of the transformer  $TR$ , considering the quantities reported to the primary side and the stray and ohmic losses of the primary side,  $R_{lp}$  and  $L_{lp}$ , and secondary side,  $R_{ls}$  and  $L_{ls}$ . Due to the center tapping at the primary side, the magnetizing inductance of the primary coil is divided into two equal parts  $L_{mp1}$  and  $L_{mp2}$ .

#### Transistor equivalent model

Since transistors  $T_1$  and  $T_2$  are alternately switched on and off at the resonant frequency of the oscillator circuit ( $f_r = 54$  kHz (3.1)), it is important to study their dynamic behavior. For this purpose, for modeling  $T_1$  and  $T_2$  the  $\pi$ -hybrid equivalent circuit is used. This latter is particularly useful for analyzing the behavior of transistors in the mid-frequency range. The equivalent model is shown in Fig



4.4, where the resistance between the base and emitter  $r_\pi$ , representing the input resistance of the transistor, is calculated as

$$r_\pi = \frac{\beta + 1}{g_m}, \quad (4.1)$$

with transconductance  $g_m = i_c/v_T$ ,  $i_c$  is the collector current given by the product between the common-emitter current gain  $\beta$  and the base current  $i_b$ . The thermal voltage of the transistor is  $v_T = 25$  mV.

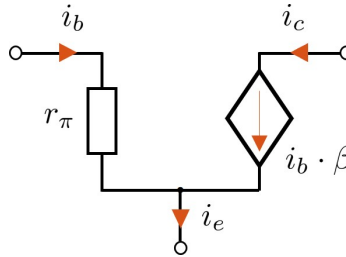


Figure 4.4:  $\pi$ -hybrid equivalent circuit for transistors  $T_1$  and  $T_2$ .

### MOSFET equivalent model

To better estimate the discharging time constant, each MOSFET in the active discharging circuit,  $M_1, \dots, M_6$ , is replaced by the equivalent circuit shown in Fig. 4.5. The equivalent circuit includes the parasitic capacitance and the output resistance  $r_{o,i}$ , which are the same for each MOSFET as they undergo the same voltage difference  $\Delta v$ . Therefore, the resistances  $r_{o,i}$ , with  $i = 1, \dots, 6$ , and their resulting series  $r_{o,Tot}$  are expressed as:

$$r_{o,i} = \frac{\Delta v}{i_{dis}} \quad r_{o,Tot} = \sum_{i=1}^6 r_{o,i}, \quad (4.2)$$

with  $i_{dis}$  calculated as in (3.3).

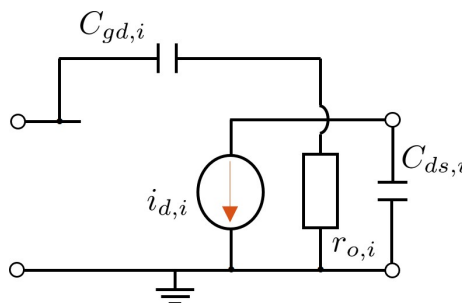


Figure 4.5: Equivalent model of high voltage MOSFET.

Finally, each output capacitance appears to be in series to each other, resulting in a capacitance series  $C_{oss,Tot}$  calculated as

$$C_{oss,Tot} = \frac{1}{\sum_{i=1}^6 \frac{1}{C_{oss,i}}}, \quad (4.3)$$

where  $C_{oss,Tot}$  is the output capacitance of the  $i$ -th MOSFET, calculated as

$$C_{oss,Tot} = C_{gd,i} + C_{ds,i}, \quad (4.4)$$

with  $C_{gd,i}$  and  $C_{gs,i}$  as constructive values from the datasheet. The parameter values are shown in Table 4.1.

Symbol	Unit	Value
$\beta$		120
$r_\pi$	$\Omega$	16.805
$L_{mp1}$	$\mu H$	9.625
$L_{mp2}$	$\mu H$	9.625
$L_{lp}$	$\mu H$	5
$R_{lp}$	$m\Omega$	208
$L_{ls}$	$mH$	180
$R_{ls}$	$\Omega$	675
$C_{ds,i}$	$pF$	24
$C_{gd,i}$	$pF$	2
$C_{oss,i}$	$pF$	26
$r_{o,i}$	$\Omega$	330

Table 4.1: Equivalent circuitual scheme's parameters.

## 4.2.2 Charging stage model

With reference to Fig. 4.2 (b), the HV circuit's charging stage consists of the cascade of two types of converter: The resonance converter and the Greinacher circuit. A methodology for determining its mathematical model is to develop firstly the mathematical models of the two converters separately and secondly an overall mathematical model that unites them. The resonant converter can be represented by a Multiple Input Single Output (MISO) model, whereas the Greinacher circuit can be represented by a Single Input Multiple Output (SIMO) model, with the output voltage of the resonant converter,  $v_{sec}$ , serving as the input to the Greinacher circuit. The two converters have distinct dynamic characteristics, making it essential to determine their ON/OFF time intervals. Transistors  $T_1$  and  $T_2$  are considered in the ON state when their collector-emitter voltages are below the corresponding saturation value, while the diode  $D_{1,\dots,4}$  are in the ON state when their voltages are  $> 0$ . Taking a switching period  $T$  of  $v_{sec}$  it can be noticed that it can be divided in four quarters  $Q_i$ , with  $i = 1, \dots, 4$ . The two transistors never lead at the same time. The diodes can be in the OFF state simultaneously, but never conducting together. Moreover, Fig. 4.6 shows that the two circuits are not perfectly synchronized, i.e.  $t_b \neq t_0 + \frac{T}{4}$  and  $t_d \neq t_0 + \frac{3T}{4}$ . The results in Fig. 4.6 were carried in *OrCAD* simulation environment. Both models will be developed for each quarter  $Q_i$ , with  $i = 1, \dots, 4$ ; then, they will be merged by exploiting average techniques into one model.

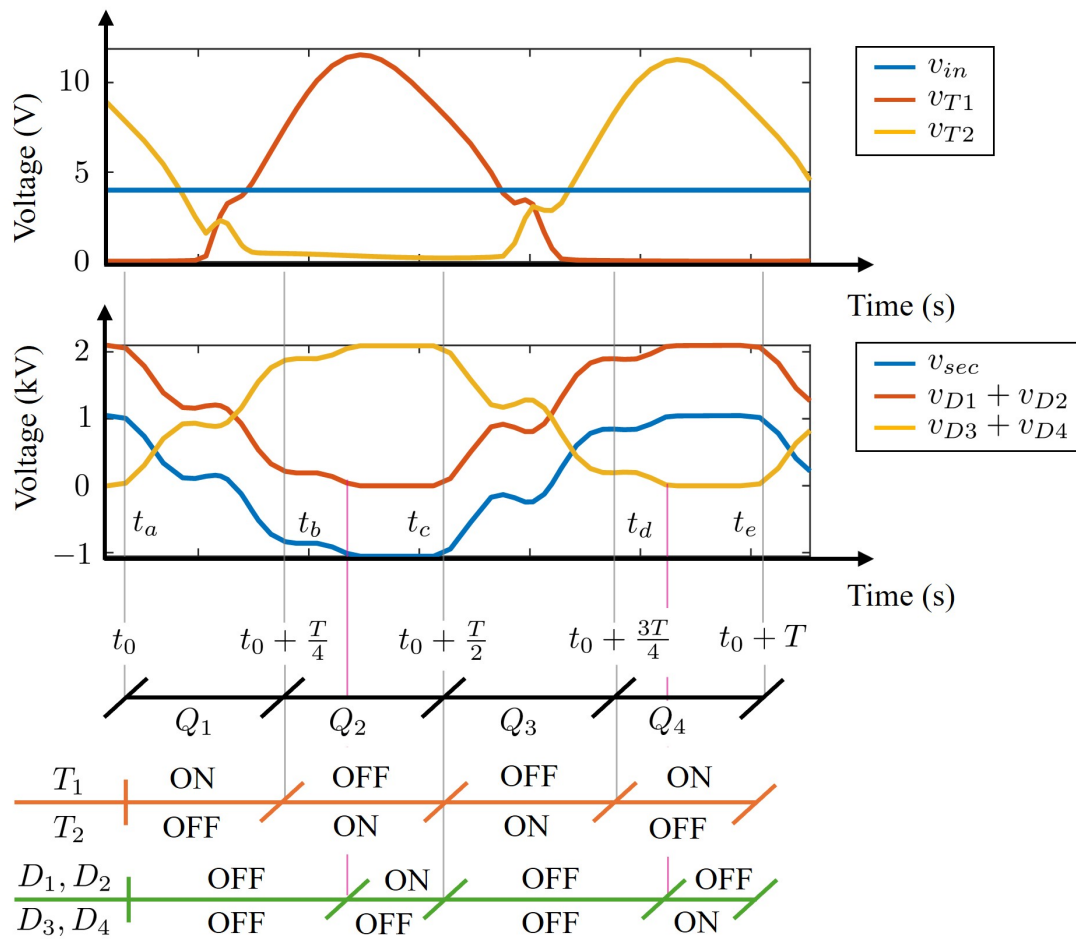


Figure 4.6: Topological stages during a switching period. (a) Trend of  $v_{in}$ ,  $v_{T1}$ ,  $v_{T2}$ . (b) Trend of  $v_{sec}$ ,  $v_{D1} + v_{D2}$ ,  $v_{D3} + v_{D4}$ .

## Resonant converter model

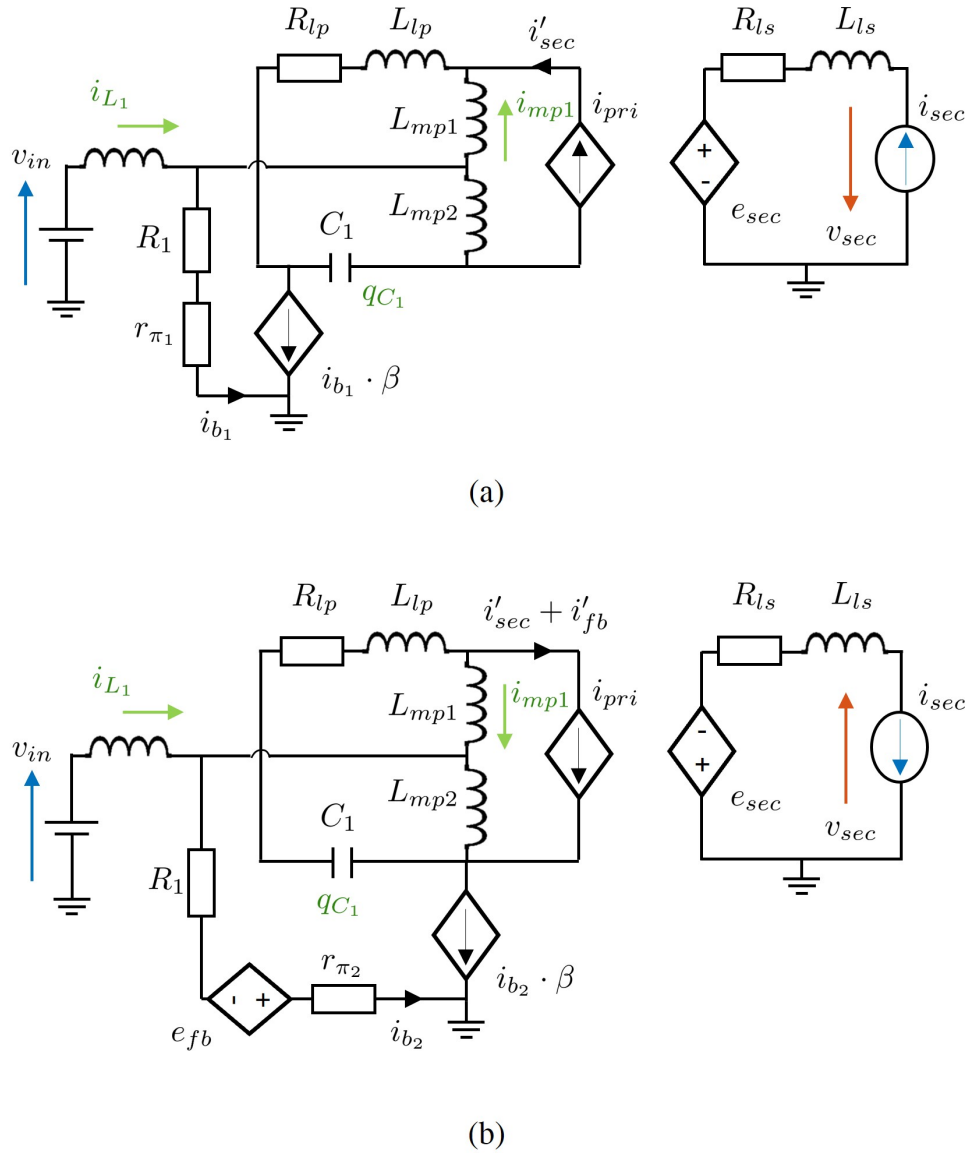


Figure 4.7: Resonant converter configuration during one switching period  $T$ . (a) Circuitual scheme for  $T_1$  On and  $T_2$  OFF; (b) Circuitual configuration for  $T_1$  OFF and  $T_2$  ON. Input signals in blue, output signal in red, and state space variable signals in green.

The resonant circuit is modeled during each quarter  $Qi$ , with  $i = 1, \dots, 4$ . With reference to Fig. 4.2 (b),  $v_{in}$  and  $i_{sec}$  are considered input signals, while  $v_{sec}$  is the output signal. Considering Fig. 4.3, the equations describing the behavior of transformer  $TR$  can be written. The capacitor  $C_1$  is in parallel to the primary side of  $TR$ , therefore  $v_{C_1} = v_{pri}$ . Thus, we obtain:

$$\begin{aligned} v_{sec} &= n_s v_{C_1}, \\ v_{fb} &= n_{fb} v_{C_1}. \end{aligned} \quad (4.5)$$

As regards the currents, it is given:

$$i_{pri} + n_s i_{sec} + n_{fb} i_{fb} = 0. \quad (4.6)$$

Therefore, the current at the primary side is given by

$$i_{pri} = -n_s i_{sec} - n_{fb} i_{fb}. \quad (4.7)$$

From Fig. 4.6 it can be noticed that  $T_1$  and  $T_2$  never lead together. Indeed,  $T_1$  leads during the half-positive wave of  $v_{sec}$  (quarters  $Q_1, Q_4$ ), while  $T_2$  during half-negative wave (quarters  $Q_2, Q_3$ ). Therefore, the resonant converter shows a switching behavior between two configurations,  $[T_1, T_2] = [ON, OFF]$ , and  $[T_1, T_2] = [OFF, ON]$ . For both configurations two state space models are developed, having in common the state space variables  $\xi = [\xi_1 \ \xi_2 \ \xi_3]^T = [i_{mp1} \ i_{L1} \ q_{C1}]^T$ , the input signal  $v_{in}$  and  $i_{sec}$ , and the output signal  $v_{sec}$ . The two circuitual configurations are shown in Fig. 4.7. The input signals are marked in blue, the output signal in red, and the state space variable signals in green.

### Configuration $T_1$ ON and $T_2$ OFF

When transistor  $T_1$  leads, the converter configuration, the electrical closed-loops and the nodes are shown in Fig. 4.8.

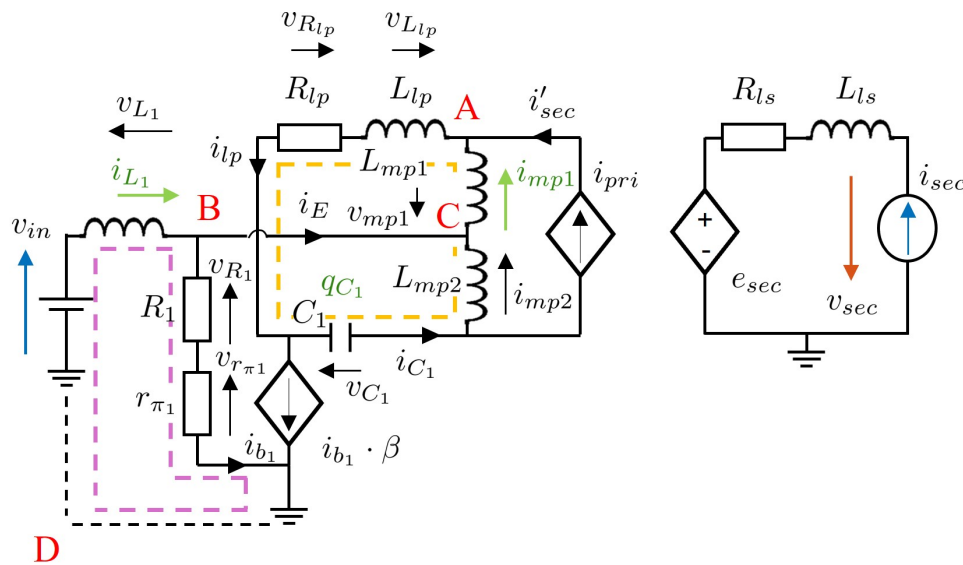


Figure 4.8: Resonant converter circuitual configuration when  $T_1$  leads, showing electrical closed-loops and nodes.

In node A, for Kirchoff's current law we have

$$i_{lp} = i_{mp1} + i'_{sec} = i_{mp1} + \frac{1}{n_s} i_{sec}. \quad (4.8)$$

Knowing that  $L_{mp1} = L_{mp2}$ , for Kirchoff's voltage law at the yellow dashed closed-loop, it holds true

$$2v_{mp1} = -R_{lp} i_{lp} - L_{lp} \dot{i}_{lp} - v_{C1}. \quad (4.9)$$

In one switching period  $T$  the current at the secondary side can be considered constant,  $\dot{i}_{sec} = 0$ . Substituting (4.8) in (4.9), and considering that for a generic capacitor  $C$  and generic inductance  $L$  it holds true that  $v_C = \frac{q}{C}$  and  $v_L = L\dot{i}_L$ , respectively, we obtain:

$$\begin{aligned} 2L_{mp1}\dot{i}_{mp1} &= -R_{lp}i_{mp1} - \frac{R_{lp}}{n_s}i_{sec} - L_{lp}\dot{i}_{mp1} - \frac{q_{C_1}}{C_1}, \\ a_1\dot{i}_{mp1} &= -R_{lp}i_{mp1} - \frac{q_{C_1}}{C_1} + b_1i_{sec}, \end{aligned} \quad (4.10)$$

where the variables  $a_1$  and  $b_1$  are:

$$\begin{aligned} a_1 &= 2L_{mp1} + L_{lp}, \\ b_1 &= -\frac{R_{lp}}{n_s}. \end{aligned} \quad (4.11)$$

For Kirchhoff's voltage law at the purple dashed closed-loop, we obtain

$$v_{L_1} = -v_{R_1} - v_{r_{\pi_1}} + v_{in}. \quad (4.12)$$

Considering that for a generic inductance  $L$  the voltage is  $v_L = L\dot{i}_L$ , equation (4.12) becomes:

$$L_1\dot{i}_{L_1} = c_1i_{L_1} + v_{in}, \quad (4.13)$$

where  $c_1 = -\frac{R_1+r_{\pi_1}}{\beta+1}$ . In node B, the sum of the currents is

$$i_E = i_{L_1} - i_{\beta_1}, \quad (4.14)$$

in node C, the sum is

$$i_{mp2} = i_{mp1} - i_E = i_{mp1} - i_{L_1} + i_{\beta_1}, \quad (4.15)$$

in node D, the sum is

$$i_{L_1} = i_{\beta_1} + \beta i_{\beta_1}. \quad (4.16)$$

In node C, considering (4.15), (4.16), and that for a generic capacitor  $C$  the current is  $i_C = \dot{q}_C$ , it holds true

$$\begin{aligned} i_{C_1} &= i_{mp2} + i'_{sec} = i_{mp1} - i_{L_1} + i_{\beta_1} + \frac{1}{n_s}i_{sec} \\ \dot{q}_{C_1} &= i_{mp1} + d_1i_{L_1} + \frac{1}{n_s}i_{sec}, \end{aligned} \quad (4.17)$$

where  $d_1 = \left(\frac{1}{\beta+1} - 1\right)$ . From (4.5), the voltage at the secondary side  $v_{sec}$  can be linked to the charge  $q_{C_1}$  on capacitor  $C_1$  as follows:

$$v_{sec} = n_s v_{C_1} = \frac{n_s q_{C_1}}{C_1}. \quad (4.18)$$

Finally, imposing that  $\xi = [\xi_1 \ \xi_2 \ \xi_3]^T = [i_{mp1} \ i_{L_1} \ q_{C_1}]^T$  and considering (4.10), (4.13), and (4.17), the state space model of the resonant converter in configuration  $T_1$  ON can be written as:

$$\begin{cases} \dot{\xi}(t) = A_{T_1}\xi(t) + B_{T_1,v}v_{in}(t) + B_{T_1,c}i_{sec}(t) \\ v_{sec}(t) = C_{T_1}\xi(t), \end{cases} \quad (4.19)$$

The state space matrices are the following:

$$A_{T_1} = \begin{bmatrix} \frac{-R_{lp}}{a_1} & 0 & -\frac{1}{C_1 a_1} \\ 0 & \frac{c_1}{L_1} & 0 \\ 1 & d_1 & 0 \end{bmatrix}, \quad B_{T_1,v} = \begin{bmatrix} 0 \\ \frac{1}{L_1} \\ 0 \end{bmatrix}, \quad (4.20)$$

$$B_{T_1,c} = \begin{bmatrix} \frac{b_1}{a_1} \\ 0 \\ \frac{1}{n_s} \end{bmatrix}, \quad C_{T_1} = \begin{bmatrix} 0 & 0 & \frac{n_s}{C_1} \end{bmatrix},$$

with  $B_{T_1,v}$  is the input state space matrix in relation to the input voltage  $v_{in}$ , and  $B_{T_1,c}$  is the input state space matrix in relation to the secondary side current  $i_{sec}$ .

### Configuration $T_1$ OFF and $T_2$ ON

When transistor  $T_2$  leads, the converter configuration, the electrical closed-loops and the nodes are shown in Fig. 4.9.

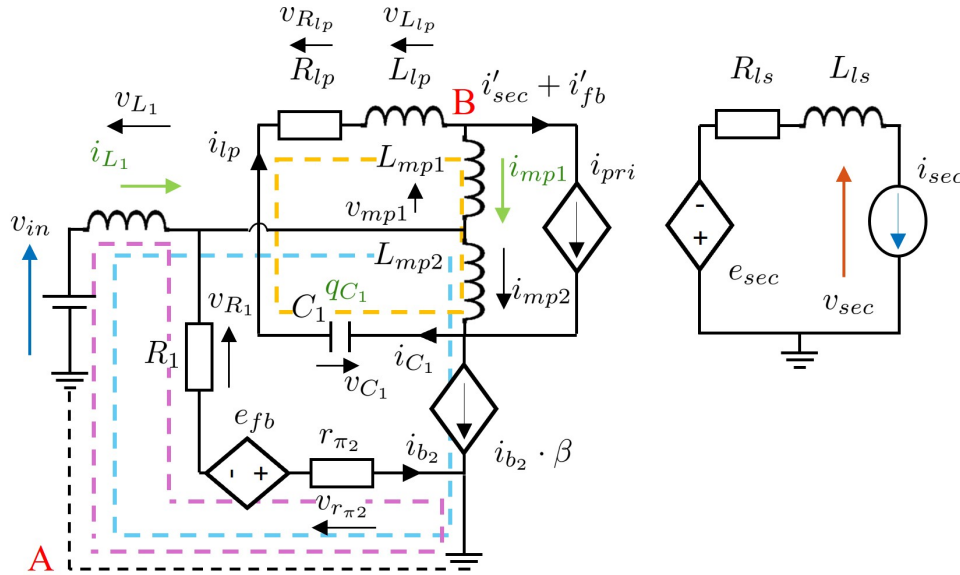


Figure 4.9: Resonant converter circuit configuration when  $T_2$  leads, showing electrical closed-loops and nodes.

In node A, for Kirchoff's current law we have

$$\begin{aligned} i_{L_1} &= i_{fb} + \beta i_{fb} \\ i_{fb} &= \frac{i_{L_1}}{1 + \beta}. \end{aligned} \quad (4.21)$$

In node B, considering (4.21), we have:

$$i_{lp} = i_{mp1} + i'_{sec} + i'_{fb} = i_{mp1} + \frac{i_{sec}}{n_s} + \frac{i_{L_1}}{n_{fb}(1 + \beta)}. \quad (4.22)$$

As before, in one switching period  $T$  the current at the secondary side can be considered constant,  $\dot{i}_{sec} = 0$ . Substituting (4.21) in (4.22), and considering that

for a generic capacitor  $C$  and generic inductance  $L$  it holds true that  $v_C = \frac{q}{C}$  and  $v_L = L\dot{i}_L$ , respectively, the Kirchhoff's voltage law at the yellow dashed closed-loop is:

$$\begin{aligned} 2v_{mp1} &= -v_{C_1} - L_{lp}\dot{i}_{lp} - R_{lp}i_{lp} \\ (2L_{mp1} + L_{lp})\dot{i}_{mp1} &= -R_{ls}i_{mp1} - \frac{L_{ls}}{n_{fb}(1+\beta)}\dot{i}_{L1} - \frac{R_{lp}}{n_{fb}(1+\beta)}i_{L1} \\ &\quad - \frac{q_{C_1}}{C_1} - \frac{R_{lp}}{n_{sec}}i_{sec}. \end{aligned} \quad (4.23)$$

The sum of the voltages at the blue dashed closed-loop is:

$$\begin{aligned} v_{L1} &= -v_{mp1} + v_{in} \\ \dot{i}_{L1} &= \frac{L_{mp1}}{L_1}\dot{i}_{mp1} + \frac{v_{in}}{L_1}. \end{aligned} \quad (4.24)$$

Substituting (4.24) in (4.23), it can be obtained

$$a_2\dot{i}_{mp1} = -R_{lp}i_{mp1} + b_2i_{L1} - \frac{q_{C_1}}{C_1} + c_2v_{in} + d_2i_{sec}, \quad (4.25)$$

with  $a_2 = 2L_{mp1} + L_{lp} - \frac{L_{lp}L_{mp1}}{n_{fb}L_1(1+\beta)}$ ,  $b_2 = -\frac{R_{lp}}{n_{fb}(1+\beta)}$ ,  $c_2 = -\frac{L_{lp}}{n_{fb}L_1(1+\beta)}$ , and  $d_2 = -\frac{R_{lp}}{n_{sec}}$ . From Kirchhoff's voltage law at the purple dashed box, the following equations can be written, considering (4.5) and (4.21),

$$v_{L1} = -v_{R_1} - v_{r\pi_2} - e_{fb} + v_{in} = -\frac{R_{L1}}{1+\beta}i_{L1} - \frac{r\pi_2}{1+\beta}i_{L1} + f_2q_{C_1} + v_{in}, \quad (4.26)$$

$$L_1\dot{i}_{L1} = e_2i_{L1} + f_2q_{C_1} + v_{in},$$

with  $e_2 = -\frac{R_{L1}}{1+\beta}$ ,  $f_2 = -\frac{n_{fb}}{C_1}$ . From Fig. 4.9, the current through capacitor  $C_1$  is equal to the current  $i_{lp}$ , thus the charge  $q_{C_1}$  can be derived as follows:

$$\dot{q}_{C_1} = i_{mp1} + g_2i_{L1} + \frac{i_{sec}}{n_{sec}}, \quad (4.27)$$

where  $g_2 = \frac{1}{n_{fb}(1+\beta)}$ .

Finally, imposing that  $\xi = [\xi_1 \ \xi_2 \ \xi_3]^T = [i_{mp1} \ i_{L1} \ q_{C_1}]^T$  and considering (4.25), (4.26), and (4.27), the state space model of the resonant converter in configuration  $T_2$  ON can be written as:

$$\begin{cases} \dot{\xi}(t) = A_{T_2}\xi(t) + B_{T_2,v}v_{in}(t) + B_{T_2,c}i_{sec}(t) \\ v_{sec}(t) = C_{T_2}\xi(t). \end{cases} \quad (4.28)$$

The state space matrices are the following:

$$\begin{aligned} A_{T_2} &= \begin{bmatrix} \frac{-R_{lp}}{a_2} & \frac{b_2}{a_2} & -\frac{1}{C_1a_2} \\ 0 & e_2 & f_2 \\ 1 & g_2 & 0 \end{bmatrix}, \quad B_{T_2,v} = \begin{bmatrix} \frac{c_2}{a_2} \\ \frac{1}{L_1} \\ 0 \end{bmatrix}, \\ B_{T_2,c} &= \begin{bmatrix} \frac{d_2}{a_2} \\ 0 \\ \frac{1}{n_s} \end{bmatrix}, \quad C_{T_2} = \begin{bmatrix} 0 & 0 & \frac{n_s}{C_1} \end{bmatrix}, \end{aligned} \quad (4.29)$$



with  $B_{T_2,v}$  is the input state space matrix in relation to the input voltage  $v_{in}$ , and  $B_{T_2,c}$  is the input state space matrix in relation to the secondary side current  $i_{sec}$ . Equations (4.19) and (4.28) represent the continuous-time Linear Time-Invariant (LTI) models of the resonant converter.

### Resonant converter model

The state space models (4.19) and (4.28) are valid, respectively, during quarters  $Q_1 - Q_4$  and  $Q_2 - Q_3$ . We can further assume that both inputs are constant over a time range  $\frac{T}{4}$ . This assumption is verified in practice for  $v_{in}$ , as  $f_r = 54$  kHz while the frequency of the input signal  $v_{in}$  varies within the range 0 – 100 Hz. For the current at the secondary side  $i_{sec}$  this assumption does not hold true. It can be addressed by considering  $i_{sec}$  as the average current over the period  $T$ , rather than the instantaneous current. With this assumption, a Zero-Order Hold (ZOH) discretization of the two models for each quarter  $Q_i$ , with  $i = 1, \dots, 4$ , can be performed. The equivalent models in the four quarters are the following:

$$(I) \text{ First quarter } Q_1 = \left[ t_0, t_0 + \frac{T}{4} \right]$$

$$Q_1 \rightarrow \begin{cases} \xi[k+1] = \Gamma_1 \xi[k] + \Theta_{1,v} v_{in}[k] + \Theta_{1,c} i_{sec}[k] \\ v_{sec}[k+1] = \Lambda_1 \xi[k], \end{cases} \quad (4.30)$$

$$(II) \text{ Second quarter } Q_2 = \left[ t_0 + \frac{T}{4}, t_0 + \frac{T}{2} \right]$$

$$Q_2 \rightarrow \begin{cases} \xi[k+1] = \Gamma_2 \xi[k] + \Theta_{2,v} v_{in}[k] + \Theta_{2,c} i_{sec}[k] \\ v_{sec}[k+1] = \Lambda_2 \xi[k], \end{cases} \quad (4.31)$$

$$(III) \text{ Third quarter } Q_3 = \left[ t_0 + \frac{T}{2}, t_0 + \frac{3T}{4} \right]$$

$$Q_3 \rightarrow \begin{cases} \xi[k+1] = \Gamma_3 \xi[k] + \Theta_{3,v} v_{in}[k] + \Theta_{3,c} i_{sec}[k] \\ v_{sec}[k+1] = \Lambda_3 \xi[k], \end{cases} \quad (4.32)$$

$$(IV) \text{ Fourth quarter } Q_4 = \left[ t_0 + \frac{3T}{4}, t_0 + T \right]$$

$$Q_4 \rightarrow \begin{cases} \xi[k+1] = \Gamma_4 \xi[k] + \Theta_{4,v} v_{in}[k] + \Theta_{4,c} i_{sec}[k] \\ v_{sec}[k+1] = \Lambda_4 \xi[k]. \end{cases} \quad (4.33)$$

The state space matrices are the following:

$$\begin{aligned}
\Gamma_1 &= \Gamma_4 = e^{A_{T_1} \frac{T}{4}}, \\
\Theta_{1,v} &= \Theta_{4,v} = A_{T_1} \left( e^{A_{T_1} \frac{T}{4}} - I \right) B_{T_{1,v}}, \\
\Theta_{1,c} &= \Theta_{4,c} = A_{T_1} \left( e^{A_{T_1} \frac{T}{4}} - I \right) B_{T_{1,c}}, \\
\Lambda_1 &= \Lambda_4 = C_{T_1}, \\
\Gamma_2 &= \Gamma_3 = e^{A_{T_2} \frac{T}{4}}, \\
\Theta_{2,v} &= \Theta_{3,v} = A_{T_2} \left( e^{A_{T_2} \frac{T}{4}} - I \right) B_{T_{2,v}}, \\
\Theta_{2,c} &= \Theta_{3,c} = A_{T_2} \left( e^{A_{T_2} \frac{T}{4}} - I \right) B_{T_{2,c}}, \\
\Lambda_2 &= \Lambda_3 = C_{T_2}.
\end{aligned} \tag{4.34}$$

The above matrices are always defined as each  $A_{T_i}$  is Hurwitz. Equations (4.30)-(4.33) represent the discrete-time LTI model of the resonant converter.

### Greinacher circuit model

The Greinacher circuit is modeled during each quarter  $Q_i$ , with  $i = 1, \dots, 4$ . With reference to Fig. 4.2 (b),  $v_{sec}$  is considered as input of the model, while  $i_{sec}$  and  $v_{DEA}$  are the outputs. The DEA is the load for the circuit. Neglecting the series resistance of the electrodes, a simplified model for the DEA is shown in Fig. 4.10: Indeed, the DEA can be as a time-variant capacitor in parallel to a high-ohmic resistor, which represents the parallel resistance between the two electrodes. In this work, the resistance  $R_p$  can be neglected since the resistor affects the overall impedance of the circuit at a given frequency  $f_r$  equal to  $e^{-\frac{1}{f_r R_p C_{DEA}}}$ . Thus, modeling the dielectric elastomer as a capacitor alone introduces an error of only  $1 - e^{-\frac{1}{f_r R_p C_{DEA}}} = 0.001$ , which is minimal and often acceptable in practical scenarios. The DEA capacitance,

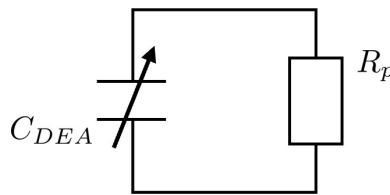


Figure 4.10: Simplified model of a DEA.

$C_{DEA}$ , is modeled as a time-varying load. However, it can be assumed approximately constant during a switching period  $T$ , since its changes directly depend on the applied voltage  $v_{DEA}$  which, in turn, follows the dynamic of the input voltage  $v_{in}$  [1]. From Fig. 4.6 it can be noticed that the diodes present in the Greinacher circuit are not synchronized with the transistors  $T_1, T_2$ . Thus, the current  $i_{sec}$  transferred during each quarter from the Resonant converter to the Greinacher circuit has to be determined. Since the diodes are considered as ideal switches,  $i_{sec}$  only changes in an impulsive way in quarter  $Q_2, Q_4$  and it is 0 in the other quarters. For modeling

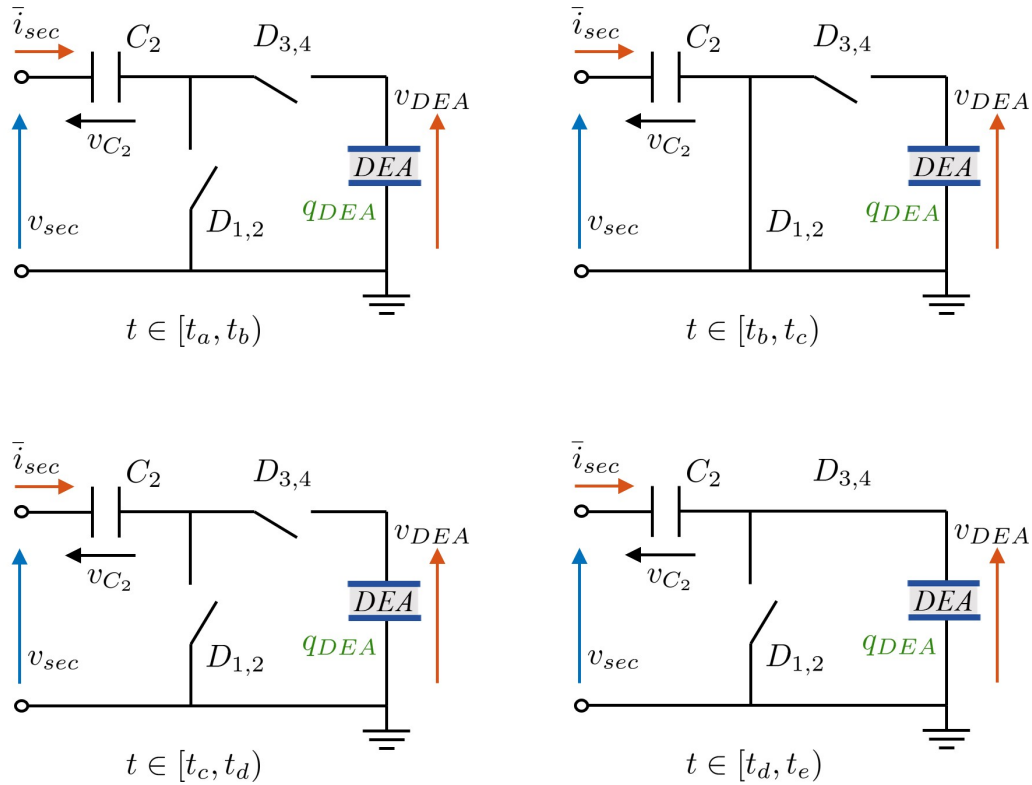


Figure 4.11: Greinacher circuit configuration during one switching period  $T$ . Input signal is in blue, output signals in red, and state space variable in green. (a) First phase; (b) Second phase; (c) Third phase; (d) Forth phase.

purposes, the instantaneous current  $i_{sec}$  is replaced with its average value  $\bar{i}_{sec}$  during each quarter  $Q_i$ , with  $i = 1, \dots, 4$ , in such a way to ensure that the same amount of charge is transferred during each quarter.

Greinacher circuit circuitual configurations during each quarter is shown in Fig. 4.11, where the input signal is marked in blue, the output signals in red, and the state space variable in green. The initial condition of the circuit in  $t = t_a$  are the following:

- I. Capacitor  $C_2$  is supposed to be fully charged at the minimum peak of  $v_{sec}$

$$v_{C_2}(t_a) = -\bar{v}_{sec} \quad (4.35)$$

- II. The DEA is supposed to be charged

$$\begin{aligned} q_{DEA}(t_a) &\neq 0 \\ v_{DEA} &= \frac{q_{DEA}(t_a)}{C_{DEA}} \neq 0 \end{aligned} \quad (4.36)$$

- **First phase:**  $t \in [t_a, t_b)$

When  $t \in [t_a, t_b)$ , all diodes are interdicted. Therefore, the voltage over the DEA does not change, neither does the current  $\bar{i}_{sec}$ . When  $t = t_b$ , by neglecting the voltage

drop over  $D_1$  and  $D_2$ , it results that:

$$\begin{aligned} q_{DEA}(t_b) &= q_{DEA}(t_a), & v_{DEA}(t_b) &= v_{DEA}(t_a) \\ v_{C_2}(t_b) &= v_{C_2}(t_a), & \bar{i}_{sec} &= 0 \end{aligned} \quad (4.37)$$

- **Second phase:**  $t \in [t_b, t_c)$

When  $t \in [t_b, t_c]$ , only  $D_1$  and  $D_2$  lead. The voltage  $v_{DEA}$  remains unchanged, while the current  $i_{sec}$  changes impulsively, thus its average value changes. In  $t = t_c$  the followings are verified:

$$\begin{aligned} q_{DEA}(t_c) &= q_{DEA}(t_b), & v_{DEA}(t_c) &= v_{DEA}(t_b), & v_{C_2}(t_c) &= v_{C_2}(t_b) \\ \bar{i}_{sec} &= \frac{\int_{t_b^+}^{t_c^-} i_{sec} dt}{t_c - t_b} = \frac{C_2}{t_c - t_b} \int_{t_b^+}^{t_c^-} \dot{i}_{sec} dt = \frac{C_2}{t_c - t_b} \left( \frac{q_{DEA}(t_a)}{C_{DEA}} - 2\bar{v}_{sec} \right) \end{aligned} \quad (4.38)$$

- **Third phase:**  $t \in [t_c, t_d)$

When  $t \in [t_c, t_d]$ , all diodes are interdicted. Therefore, the voltage over the DEA does not change, neither does the current  $\bar{i}_{sec}$ . When  $t = t_d$  it results that:

$$\begin{aligned} q_{DEA}(t_d) &= q_{DEA}(t_c), & v_{DEA}(t_d) &= v_{DEA}(t_c) \\ v_{C_2}(t_d) &= v_{C_2}(t_c), & \bar{i}_{sec} &= 0 \end{aligned} \quad (4.39)$$

- **Fourth phase:**  $t \in [t_d, t_e)$

Finally, when  $t \in [t_d, t_e)$ ,  $v_{DEA}$  changes as both  $D_3$  and  $D_4$  lead. Capacitor  $C_2$  and the DEA are in series, thus the equivalent capacitance of the circuit is  $C_{eq} = \frac{C_2 C_{DEA}}{C_2 + C_{DEA}}$ . Due to the assumption of constant  $C_{DEA}$ , the charge in the DEA evolves according to:

$$\dot{q}_{DEA}(t) = C_{eq} \dot{v}_{sec}. \quad (4.40)$$

In addition, in  $t = t_d$  it holds true that:

$$v_{sec}(t_d) = v_{C_2}(t_d) + v_{DEA}(t_d) = -\bar{v}_{sec} + v_{DEA}(t_d). \quad (4.41)$$

By integrating both side of (4.40), using (4.41) in the interval  $[t_d, t_e)$ , the value of  $q_{DEA}(t_e)$  is calculated as:

$$q_{DEA}(t_e) = q_{DEA}(t_d) + C_{eq} \left( v_{sec}(t_e) - v_{sec}(t_d) \right) = \frac{C_{DEA}^2}{C_{DEA} + C_2} q_{DEA}(t_a) + 2C_{eq} \bar{v}_{sec}. \quad (4.42)$$

The average value of  $i_{sec}$  is:

$$\bar{i}_{sec} = \frac{C_{eq} \int_{t_d^+}^{t_e^-} \dot{i}_{sec} dt}{t_e - t_d} = -\frac{C_{eq} \left( 2\bar{v}_{sec} - \frac{q_{DEA}(t_a)}{C_{DEA}} \right)}{t_e - t_d}. \quad (4.43)$$

The actual value of  $t_b$  and  $t_d$  differ for each cycle, depending on the actual value of  $v_{sec}$  and  $v_{DEA}$ . For further simplifying the model, it is assumed that  $t_b = t_0 + \frac{T}{4}$  and

$t_d = t_0 + \frac{3T}{4}$ , so that a proper synchronization can be made between the resonant converter and the Greinacher circuit.

By considering (4.37)-(4.43), the discrete-time model describing the Greinacher circuit during the four quarters becomes:

$$\begin{cases} q_{DEA}[k+1] = M_i z[k] + N_i \bar{v}_{sec}[k] \\ v_{DEA}[k] = q_{DEA}[k]/C_{DEA} \\ i_{sec}[k] = O_i q_{DEA}[k] + P_i \bar{v}_{sec}, \end{cases} \quad i = 1, \dots, 4 \quad (4.44)$$

where  $\bar{v}_{sec}$  denotes the positive peak of  $v_{sec}$  over  $T$ , and

$$\begin{aligned} M_{1,2,3} &= 1, \quad M_4 = \frac{C_{DEA}^2}{C_2 + C_{DEA}}, \quad N_{1,2,3} = 0, \quad N_4 = \frac{2C_2 C_{DEA}}{C_2 + C_{DEA}}, \quad O_{1,3} = 0, \\ O_2 &= \frac{4C_2}{TC_{DEA}}, \quad O_4 = \frac{4C_2 C_{DEA}}{T(C_2 + C_{DEA})}, \quad P_{1,3} = 0, \quad P_2 = -\frac{8C_2}{T}, \\ P_4 &= -\frac{8C_2 C_{DEA}}{T(C_2 + C_{DEA})}. \end{aligned} \quad (4.45)$$

### Charging model

In deriving (4.30)-(4.33) and (4.44), it is assumed that the inputs of each model remain constant during the time period of duration  $\frac{T}{4}$ . This is of course an approximation, which is indeed necessary for the development of the full model.

By replacing  $v_{sec}$  from (4.30)-(4.33) in (4.44), and replacing  $i_{sec}$  from (4.44) in (4.30)-(4.33), the combined model with  $i_1, \dots, 4$  can be obtained:

$$Q_i \rightarrow \begin{cases} \zeta[k+1] = F_i \zeta[k] + G_i v_{in}[k] \\ y[k] = H \zeta[k], \end{cases} \quad (4.46)$$

where  $v_{in}[k]$  is assumed constant over the period  $T$ , and:

$$\begin{aligned} \zeta &= \begin{bmatrix} \xi \\ q_{DEA} \end{bmatrix}, \quad y = v_{DEA}, \quad F_i = \begin{bmatrix} \Gamma_i + \Theta_{i,c} P_i \Lambda_i & \Theta_{i,c} O_i \\ N_i \Gamma_i & M_i \end{bmatrix}, \\ G_i &= \begin{bmatrix} \Theta_{i,v} \\ 0 \end{bmatrix}, \quad H = [0 \quad 1/C_{DEA}]. \end{aligned} \quad (4.47)$$

Based on (4.46), the model periodically oscillates between the four quarters  $Q_i$  with a switching period  $T/4$ . By assuming that the system is in  $Q_1$  both at  $t_0$  and  $t_0 + T$ , the four models in (4.46) are combined in the following discrete-time model:

$$\begin{cases} \zeta[k+1] = F \zeta[k] + G v_{in}[k] \\ y[k] = H \zeta[k], \end{cases} \quad (4.48)$$

where the matrices are  $F = F_4 F_3 F_2 F_1$  and  $G = F_4 F_3 F_2 G_1 + F_4 F_3 G_2 + F_4 G_3 + G_4$ .

Model (4.48) represents a discrete-time average representation of the complete circuit dynamics. The sampling time of such a discrete-time realization is given by  $T$ , which is the period of oscillation. This quantity  $T$  usually differs from the

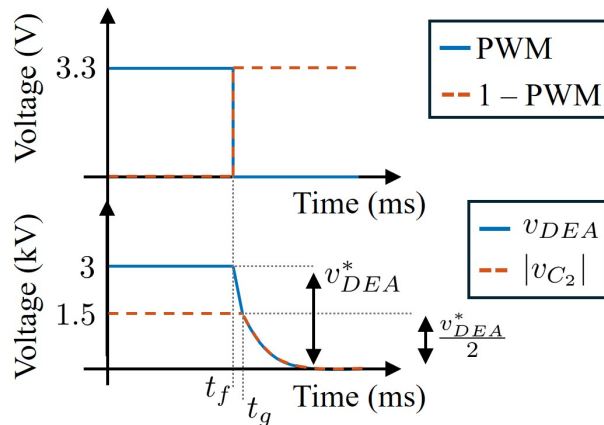


Figure 4.12: Voltages  $v_{DEA}$  and  $v_{C_2}$  during the discharging phase. The wording 1-PWM indicates that the PWM signal to the discharging stage is complementary to the charging PWM signal.

sampling time of the controller  $T_S$ , therefore it is meaningful to convert (4.48) into an equivalent continuous-time model, which is subsequently used for control. By using the inverse equations for the ZOH discretization:

$$\begin{cases} \dot{\zeta}(t) = A_{cha}\zeta(t) + B_{cha}v_{in}(t) \\ v_{DEA}(t) = H\zeta(t), \end{cases} \quad (4.49)$$

with  $A_{cha} = \frac{1}{T}\log(F)$ ,  $B_{cha} = (F - I)^{-1}\left(\frac{1}{T}\log(F)\right)G$ .

### 4.2.3 Discharging stage model

The discharging stage consists of the combination of the Greinacher circuit, when  $v_{sec} = 0$ , and the cascade of HV MOSFETs triggered by the small-signal transistor  $T_3$ , as shown in Fig. 3.1 in the yellow dashed box. The HV MOSFETs are modeled via their equivalent circuit, Fig. 4.5.

The discharging phase is triggered when the PWM signal on  $T_3$  is switched to a high level. In this case, it is assumed that the DEA and capacitor  $C_2$  are charged, i.e.,  $v_{DEA}(t_f) = v_{DEA}^* > 0$ , and  $|v_{C_2}(t_f)| = v_{DEA}^*/2$ , as shown in Fig. 4.12. The discharging stage during the discharge phase find itself in two different configurations, based on conduction time intervals of the diodes. The two configurations are shown in Fig. 4.13, where the output signal is marked in red and the state space variable in green.

- **First phase:**  $t \in [t_f, t_g)$

When  $t \in [t_f, t_g)$  all diodes are OFF, thus,  $v_{C_2}$  remains unchanged, the DEA is in series to the output capacitance  $C_{oss, Tot}$ , the ON-resistance  $r_{o, Tot}$ , and the discharging resistor  $R_{dis}$ . Therefore,  $v_{DEA}$  decreases exponentially until a certain time instant  $t_g$ , where  $v_{DEA}(t_g) = |v_{C_2}(t_g)| = v_{DEA}^*/2$ . Thus, for  $v_{DEA} > \frac{v_{DEA}^*}{2}$ , the following

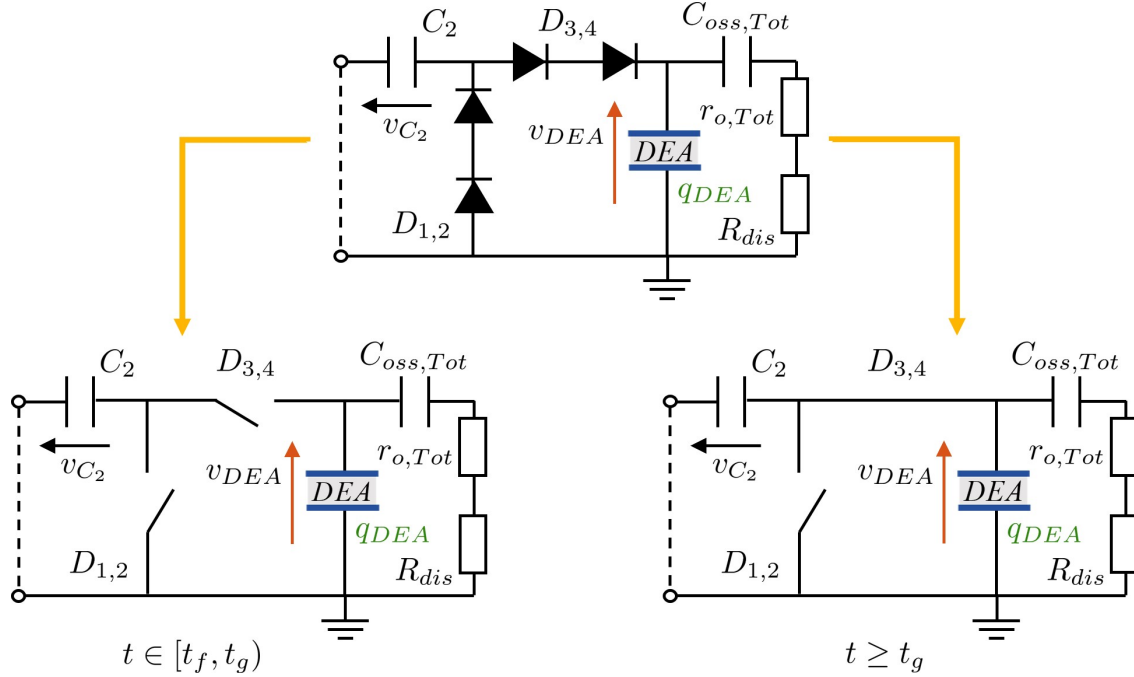


Figure 4.13: Discharging stage configurations. Output signal is marked in red, while the state space variable is in green.

state space model holds true:

$$\begin{cases} \dot{q}_{DEA}(t) = A_{dis,A} q_{DEA}(t) \\ v_{DEA}(t) = C_{dis,A} q_{DEA}(t), \end{cases} \quad (4.50)$$

with initial condition given by  $q_{DEA}(t_f)$  at the moment the discharging phase begins. The matrices are:

$$A_{dis,A} = -\frac{1}{R_{eq}C_{eq,A}}, \quad C_{dis,A} = \frac{1}{C_{DEA}}, \quad (4.51)$$

with  $R_{eq}$  and  $C_{eq,A}$  defined as:

$$R_{eq} = r_{o,Tot} + R_{dis}, \quad C_{eq,A} = \frac{1}{\frac{1}{C_{DEA}} + \frac{1}{C_{oss,Tot}}}. \quad (4.52)$$

- **Second phase:**  $t \geq t_g$

When  $t \geq t_g$  the diodes  $D_3$  and  $D_4$  lead so that the parallel between  $C_2$  and the series of  $C_{DEA}$  and  $C_{oss,Tot}$  is in series with each other and with  $R_{eq}$ . Therefore, both  $v_{DEA}$  and  $v_{C_2}$  decrease exponentially. The following model is valid:

$$\begin{cases} \dot{q}_{DEA}(t) = A_{dis,B} q_{DEA}(t) \\ v_{DEA}(t) = C_{dis,B} q_{DEA}(t), \end{cases} \quad (4.53)$$

with initial condition given by  $q_{DEA}(t_g)$  before the switching between (4.50) and (4.53). The matrices are the following:

$$A_{dis,B} = -\frac{1}{R_{eq}C_{eq,B}}, \quad C_{dis,B} = \frac{1}{C_{DEA}}, \quad (4.54)$$

with  $C_{eq,B}$  defined as:

$$C_{eq,B} = C_2 + \frac{1}{\frac{1}{C_{DEA}} + \frac{1}{C_{oss,Tot}}}. \quad (4.55)$$

The discharging stage presents a switching behavior between the first and the second phase, i.e.,  $t \in [t_f, t_g)$  and  $t \geq t_g$ . Indeed, as shown in Fig. 4.12, the discharging stage is characterized by two discharging time constant. The switching to the second phase occurs if the PWM signal's frequency is smaller than  $\frac{1}{t_g - t_f}$ . In this work we assume that the PWM frequency  $f_{PWM} = 15000 \text{ Hz} > \frac{1}{t_g - t_f}$ . Thus, the discharging stage can be represented only by (4.50).

#### 4.2.4 Switching model

The HV circuit shown in Fig. 3.2, focus of this work, presents a switching behavior between charging and discharging phases. To modeling, two separate state space representations have been developed for the charging and discharging stage respectively, i.e., (4.49) and (4.50). Those two models are now combined into one model, named *Switching model*. For this purpose, let us introduce the variable  $\sigma$ , i.e.,

$$\begin{cases} \sigma = c & \rightarrow \text{Charging phase} \\ \sigma = d & \rightarrow \text{Discharging phase.} \end{cases} \quad (4.56)$$

Equation (4.50) needs to have the same state variables of (4.49), thus the following augmented state realization is set:

$$\begin{cases} \dot{\zeta}(t) = A_{dis}\zeta(t) + B_{dis}v_{in}(t) \\ v_{DEA}(t) = C_{dis}\zeta(t) + D_{dis}v_{in}(t), \end{cases} \quad (4.57)$$

where

$$\begin{aligned} A_{dis} &= \begin{bmatrix} 0_{3 \times 3} & 0_{3 \times 1} \\ 0_{1 \times 3} & A_{dis_A} \end{bmatrix}, & B_{dis} &= 0_{4 \times 1}, \\ C_{dis} &= [0_{1 \times 3} \quad C_{dis_A}], & D_{dis} &= 0. \end{aligned} \quad (4.58)$$

By considering (4.49) and (4.57), the *switching model* describing the overall circuit is:

$$\begin{cases} \dot{\zeta}(t) = A_{\sigma}\zeta(t) + B_{\sigma}v_{in}(t) \\ v_{DEA}(t) = C_{\sigma}\zeta(t) + D_{\sigma}v_{in}(t), \end{cases} \quad (4.59)$$

where  $\sigma \in \{c, d\}$  is the switching variable selecting the charging ( $c$ ) and discharging ( $d$ ) modes, and  $v_{in}$  is the input voltage signal. The state vector  $\zeta \in \mathbb{R}^4$  includes, respectively, the current through the magnetizing inductance at the primary side of the transformer, the current through the input inductance of the resonant converter, the electrical charge on the capacitor of the resonant converter, and the electrical charge of the DEA. The output variable  $v_{DEA}$  represents the output voltage on the DEA. The equation (4.59) represents the LTI state space model describing the behavior of the HV driving circuit for DEA, having as input signal the voltage  $v_{in}$  and as output voltage the voltage applied over the actuator  $v_{DEA}$ .



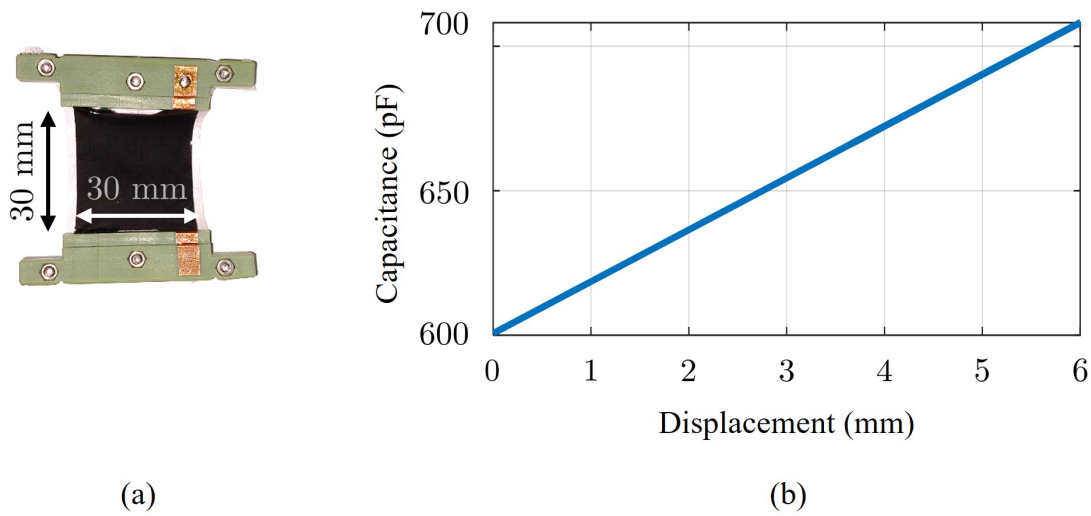


Figure 4.14: (a) Dielectric elastomer actuator; (b) Displacement-capacitance curve, obtained by stretching the DEA with a linear motor at 0.1 Hz.

### 4.3 Average model

The model (4.59) is a *switching model* that well characterizes the circuit's behavior during both the charging and discharging phases. On the other hand it involves high frequency operations and intricate details of on/off states, which can be complex to analyze and simulate, since it requires fine time steps to capture the rapid changes, which can be computationally intensive. Moreover for switching models have complicated structure, making the design of a control algorithm even more harder. For these reasons in this work we propose equivalent models based on average and linear techniques. Average models simplify the analysis by focusing on the overall behavior over a switching period rather than the instantaneous states. In this section the average model will be presented.

#### 4.3.1 Switching model sensitivity for time-varying load

The state-space matrices of the switching model (4.59) depend on the the capacitance of the DEA,  $C_{DEA}$ . For an easier handling, the sensitivity of the model for time-varying load is studied. A DEA of dimensions  $30\text{ mm} \times 30\text{ mm} \times 50\text{ }\mu\text{m}$  is characterized. A tensile test is conducted by deforming the DEA with an AEROTECH ANT-25LA linear actuator, while its capacitance is measured with an HM 8118 LCR meter and its displacement is simultaneously acquired with a laser sensor. The collected data are used to construct a capacitance-displacement map, shown in Fig. 4.14 . Since the adopted LCR meter cannot be used when the DEA is subjected to high voltage, the obtained map permits estimating the DEA time-varying capacitive load based on displacement reading. It can be seen that the DEA capacitance varies linearly at increasing displacement.

A proper transfer function of the model (4.57) cannot be derived, due to its independence to the input  $v_{in}$  (as a result of lack of controllability). Nevertheless,

to quantify its overall dynamics performance in the frequency domain, an equivalent transfer function  $T_e(s)$  from the initial condition  $\zeta(0)$  to the output voltage  $v_{DEA}$  can be derived. From (4.57), considering its initial condition  $\zeta(0)$ , the following relationship in the Laplace domain can be derived

$$V_{DEA}(s) = \frac{C_{dis}\zeta(0)}{sI - A_{dis}}. \quad (4.60)$$

From 4.60, the equivalent transfer function  $T_e(s)$  and, therefore, the equivalent system, are obtained:

$$T_e(s) = \frac{V_{DEA}(s)}{\zeta(0)} = \frac{C_{dis}}{sI - A_{dis}} \quad (4.61)$$

$$\begin{cases} \dot{\zeta} = A_{dis}\zeta + \zeta(0) \\ v_{DEA} = C_{dis}\zeta \end{cases}.$$

It can be noticed that the free response of the system (4.57) with non-zero initial condition coincides to the impulsive response of system (4.61) with zero initial condition. Therefore, we qualitatively quantify the equivalent dynamic performance of the discharge model with the Bode diagram of (4.61) for the ease of comparison with the charging model. The bode diagrams are calculated considering as load

- $C_{DEA} = 600$  pF
- $C_{DEA} = 660$  pF
- $C_{DEA} = 710$  pF,

to study the sensitivity of the models. Figure 4.15 shows that small variations of  $C_{DEA}$  produce negligible changes of the charging and discharging models, thus the switching model. Hence, they are henceforth neglected. For this reason, the state space matrices can be calculated by considering the capacitance nominal value  $C_{DEA} = 600$  pF and are given as follows:

$$\begin{aligned} A_c &= -1080I_4, & A_d &= \begin{bmatrix} 0_{1 \times 3} & 0_{3 \times 1} \\ 0_{1 \times 3} & -103.30 \end{bmatrix} \\ B_c &= [0_{1 \times 3} \quad 1024]^T, & B_d &= [0_{1 \times 4}]^T \\ C_c &= [0_{1 \times 3} \quad 543.13], & C_d &= [0_{1 \times 3} \quad 553], \end{aligned} \quad (4.62)$$

where  $I_n$  is the identity matrix of dimension  $n$ , while  $0_{m \times n}$  denotes an  $m \times n$  matrix made by zeros. The presence of several null elements in matrices  $A_c$  and  $A_d$  is due to numerical reasons, as their values are on the order of less than  $10^{-14}$  and are therefore considered negligible. The matrices in (4.62) will be use from now on.

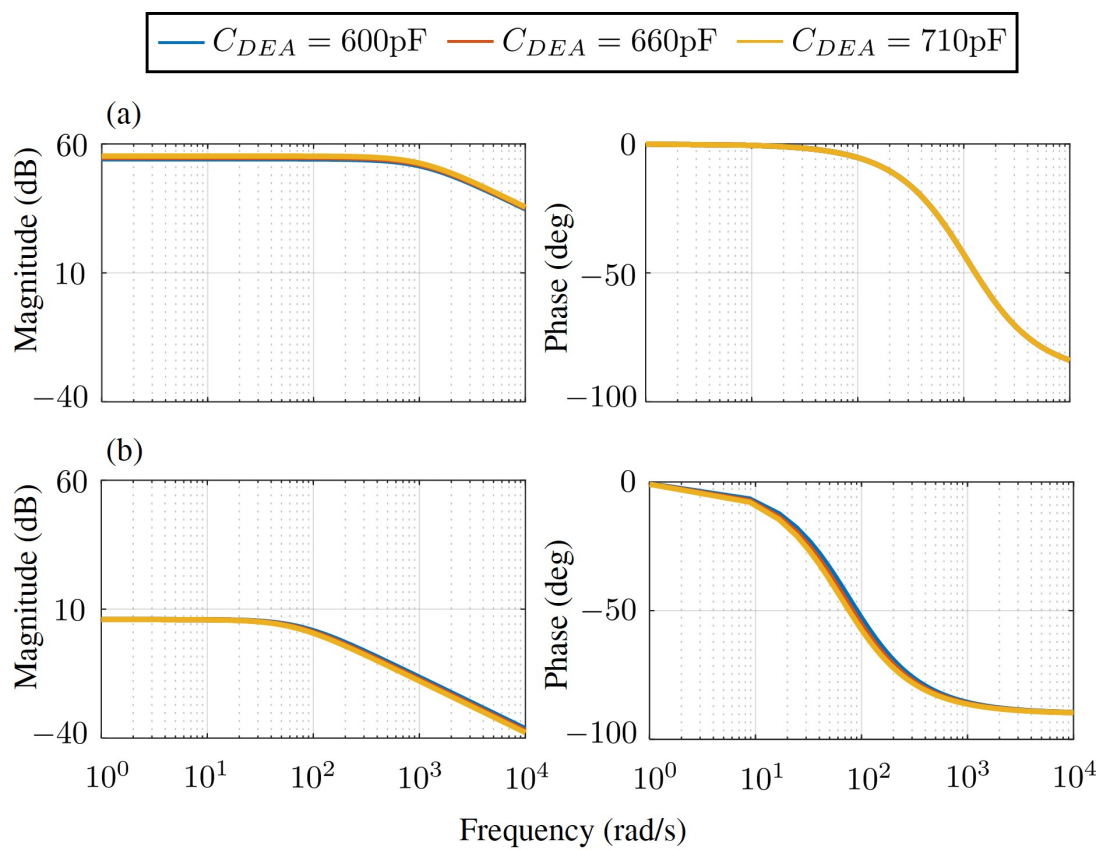


Figure 4.15: Bode diagrams of (a) charging model and (b) discharging model for different value of the load  $C_{DEA}$ .

### 4.3.2 Average model

It can be readily verified that (4.59) is not fully controllable for  $\sigma \in \{c, d\}$ . Indeed, the rank of the controllability matrix is not full,  $rank(\mathbf{C}_\sigma) = 1$ , with  $\mathbf{C}$  is the controllability matrix. The two modes present only one controllable state, i.e., the electrical charge on the DEA. A canonical decomposition of both modes is carried out and it is the following:

$$\begin{cases} \dot{\zeta} &= \begin{bmatrix} A_\sigma^{NC} & 0_{3 \times 1} \\ 0_{1 \times 3} & A_\sigma^C \end{bmatrix} \zeta + \begin{bmatrix} 0_{3 \times 1} \\ B_\sigma^C \end{bmatrix} v_{in}, \\ v_{DEA} &= \begin{bmatrix} 0_{1 \times 3} & C_\sigma^C \end{bmatrix} \zeta, \end{cases} \quad (4.63)$$

where the superscripts  $C$  and  $NC$  stand for controllable and non-controllable. The fully controllable switching model results in:

$$\begin{cases} \dot{\zeta}_4 = A_\sigma^C \zeta_4 + B_\sigma^C v_{in} \\ v_{DEA} = C_\sigma^C \zeta_4 \end{cases} . \quad (4.64)$$

For an easier analysis and control, (4.64) is converted into an average model, as commonly done in power electronics control literature.

The average state-space equations are derived by multiplying the duty-cycle  $\alpha$  and its complement  $1 - \alpha$  with the controllable components of the charging and discharging models, as the input PWM wave with duty-cycle  $\alpha$  determines one of the two circuit modes. Thus, the averaged state-space model is obtained as follows [72]:

$$\begin{cases} \dot{\zeta}_{av} = f(\zeta_{av}, \alpha) \\ v_{DEA,av} = g(\zeta_{av}, \alpha) \end{cases} , \quad (4.65)$$

where

$$\begin{aligned} f(\zeta_{av}, \alpha) &= \left( \alpha A_c^C + (1 - \alpha) A_d^C \right) \zeta_{av} + \left( \alpha B_c^C + (1 - \alpha) B_d^C \right) \bar{v}_{in}, \\ g(\zeta_{av}, \alpha) &= \left( \alpha C_c^C + (1 - \alpha) C_d^C \right) \zeta_{av}. \end{aligned} \quad (4.66)$$

$\zeta_{av}$  is the average electrical charge on the DEA,  $v_{DEA,av}$  is the average output voltage on the DEA, and  $\bar{v}_{in}$  is the maximum applied input voltage  $\bar{v}_{in} = 6$  V. The first-order nonlinear time-invariant model (4.65) describes the average behavior of the HV circuit in a control-oriented fashion.

## 4.4 Validation in simulation

In this section the models (4.59) and (4.65) will be validated in simulation, respectively in 4.4.1 and in 4.4.2. As simulation environment, *Cadence OrCAD Capture* was used, while the models were implemented in MATLAB/Simulink.

### 4.4.1 Switching model - Validation in simulation

To validate the switching model (4.59), eight different scenarios have been investigated:

1. Square wave input  $v_{in}$  of amplitude  $A = 4$  V and frequency  $f = 1$  Hz.
2. Square wave input  $v_{in}$  of amplitude  $A = 6$  V and frequency  $f = 1$  Hz.
3. Square wave input  $v_{in}$  of amplitude  $A = 4$  V and frequency  $f = 2$  Hz.
4. Square wave input  $v_{in}$  of amplitude  $A = 6$  V and frequency  $f = 2$  Hz.
5. Sinusoidal wave input  $v_{in}$  of amplitude peak-peak  $A_{pp} = 4$  V and frequency  $f = 1$  Hz.
6. Sinusoidal wave input  $v_{in}$  of amplitude peak-peak  $A_{pp} = 6$  V and frequency  $f = 1$  Hz.
7. Sinusoidal wave input  $v_{in}$  of amplitude peak-peak  $A_{pp} = 4$  V and frequency  $f = 2$  Hz.
8. Sinusoidal wave input  $v_{in}$  of amplitude peak-peak  $A_{pp} = 6$  V and frequency  $f = 2$  Hz.

The performance of mathematical model (4.59) obtained by running the model on *MATLAB-Simulink*, has been compared to the performance of the circuit simulated in *OrCAD*.

It is important to point out that the PWM signals control the switching between charging and discharging models. If PWM is high (1-PWM is low), the charging stage is ON, thus, the charging model is selected; if PWM is low (1-PWM is high), the discharging model is selected. Thus,

$$\begin{cases} PWM \text{ high} \rightarrow \sigma = c \\ PWM \text{ low} \rightarrow \sigma = d \end{cases} \quad (4.67)$$

For the validation in simulation an ideal capacitor of 440 pF has been chosen as load, as it is the nominal value of the capacitance of the real DEA used for the experimental validation, that will be discussed in the next section. Fig. 4.16 shows the response of the circuit in simulation made in *OrCAD* and from model (4.59) when square wave signals are applied as input. It can be noticed that the circuit's gain is equal to 500. Indeed, at 4 V amplitude of the input signal  $v_{in}$  corresponds 2 kV amplitude of the output voltage  $v_{DEA}$ . Same relation holds true when  $v_{in,max} = 6$  V. Moreover, it is clear that the discharging circuit is characterized by two discharging time constants, as the model (4.50) and (4.53) described.

Fig. 4.17 shows the results of the comparison between the simulation and the switching model (4.59) for sinusoidal wave input signals. Also in those cases, the gain of 500 is respected. It can be seen that, while the simulation does not show any switching behavior of the circuit, the model results clearly show it. For sinusoidal wave signals, the switching between the two models is evident, since at each period of the PWM signal (that change with a frequency of 15 kHz), the two models alternate each other.

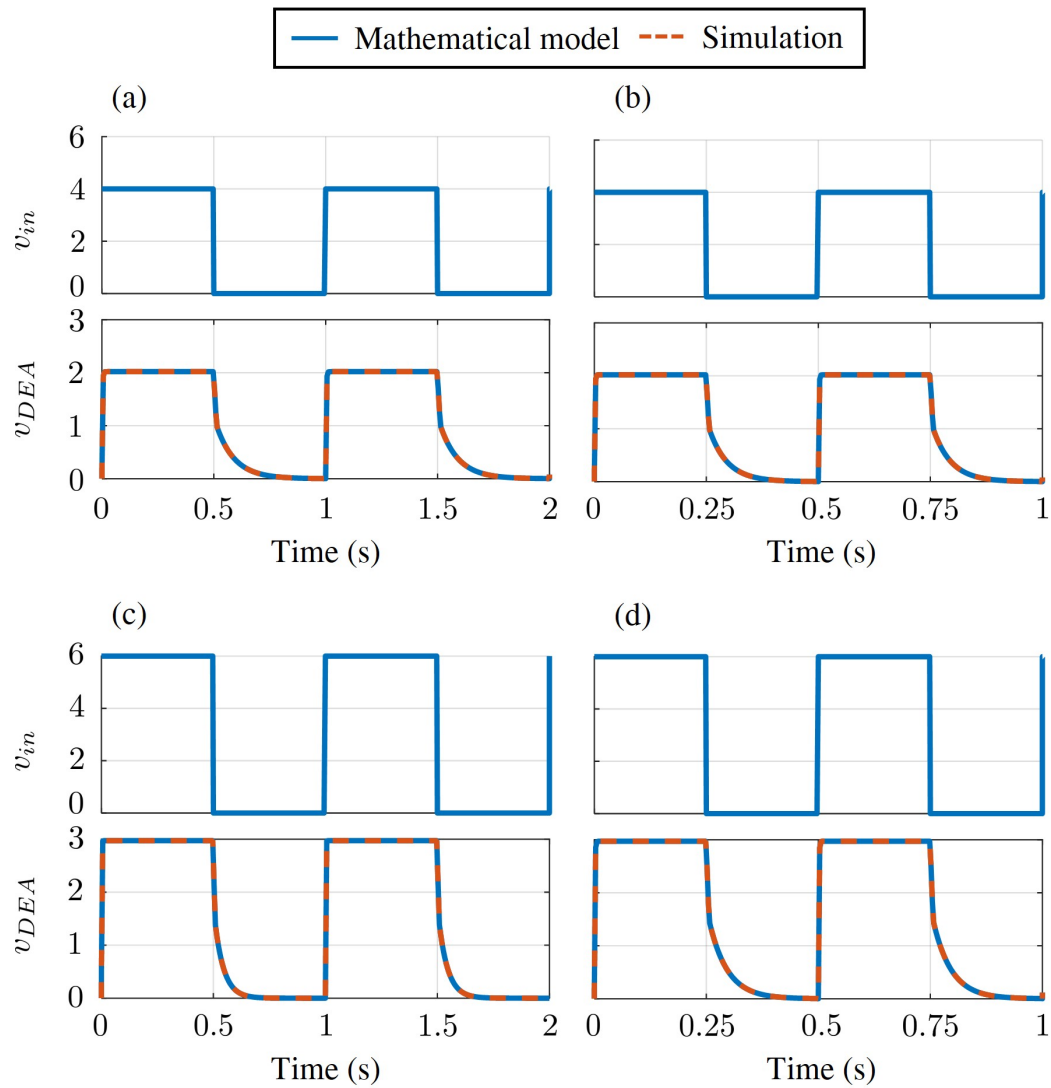


Figure 4.16: Validation in simulation for square wave signals. (a) Square wave signal with amplitude  $A = 4$  V and frequency  $f = 1$  Hz; (b) Square wave signal with amplitude  $A = 4$  V and frequency  $f = 2$  Hz; (c) Square wave signal with amplitude  $A = 6$  V and frequency  $f = 1$  Hz; (d) Square wave signal with amplitude  $A = 6$  V and frequency  $f = 2$  Hz.

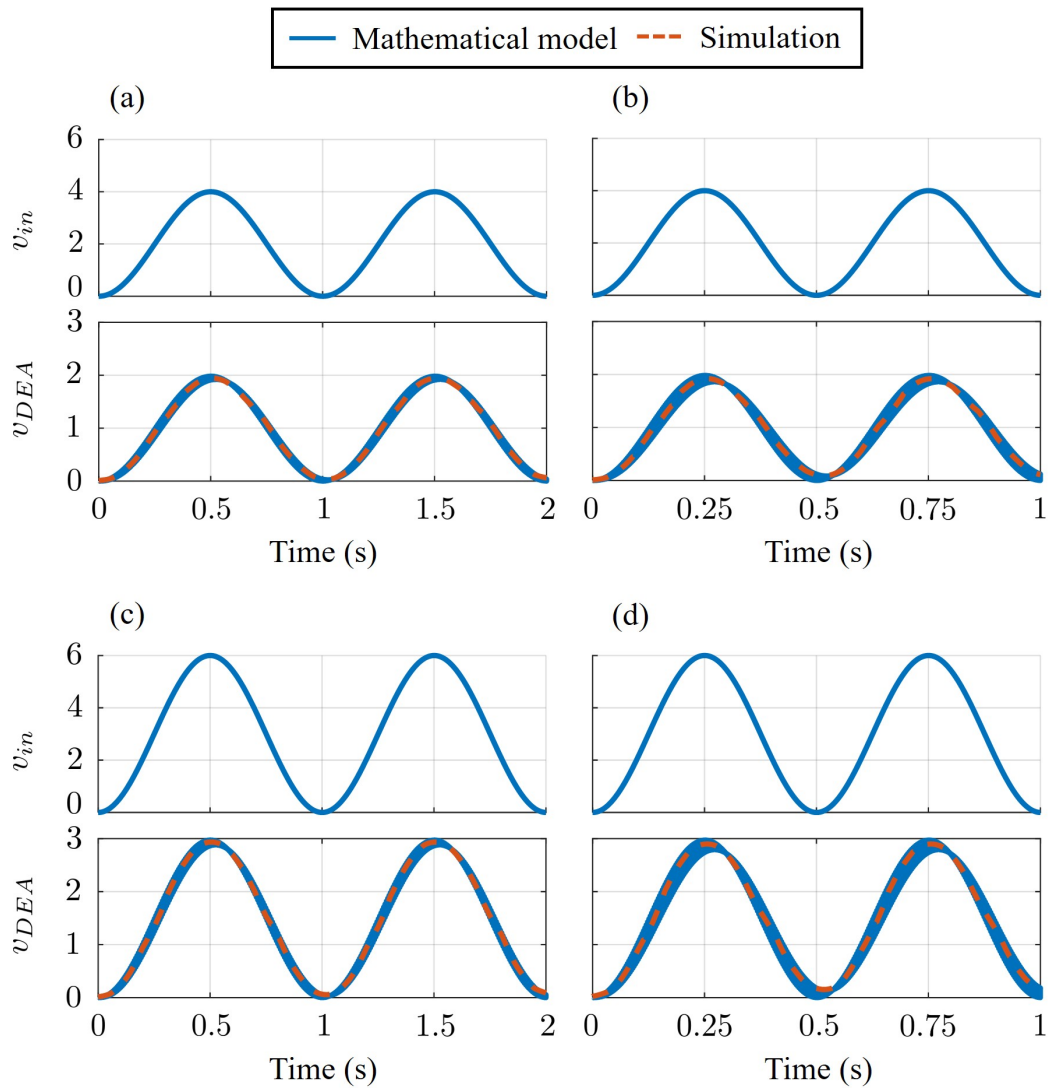


Figure 4.17: Validation in simulation for square wave signals. (a) Sinusoidal wave input signal with peak-peak amplitude  $A = 4 V_{pp}$  and frequency  $f = 1$  Hz; (b) Sinusoidal wave input signal with peak-peak amplitude  $A = 4 V_{pp}$  and frequency  $f = 2$  Hz; (c) Sinusoidal wave input signal with peak-peak amplitude  $A = 6 V_{pp}$  and frequency  $f = 1$  Hz; (d) Sinusoidal wave input signal with peak-peak amplitude  $A = 6 V_{pp}$  and frequency  $f = 2$  Hz.

### 4.4.2 Average model - Validation in simulation

The average model (4.65) is validated in simulation and compared to the switching model. Figure 4.18 shows the response of the two models in different cases: Step response, dynamic behavior in response to sinusoidal wave from 1.2 V to 6 V at different frequencies. The average model equals quite well the switching model for the full range of actuation voltage up to 100 Hz.

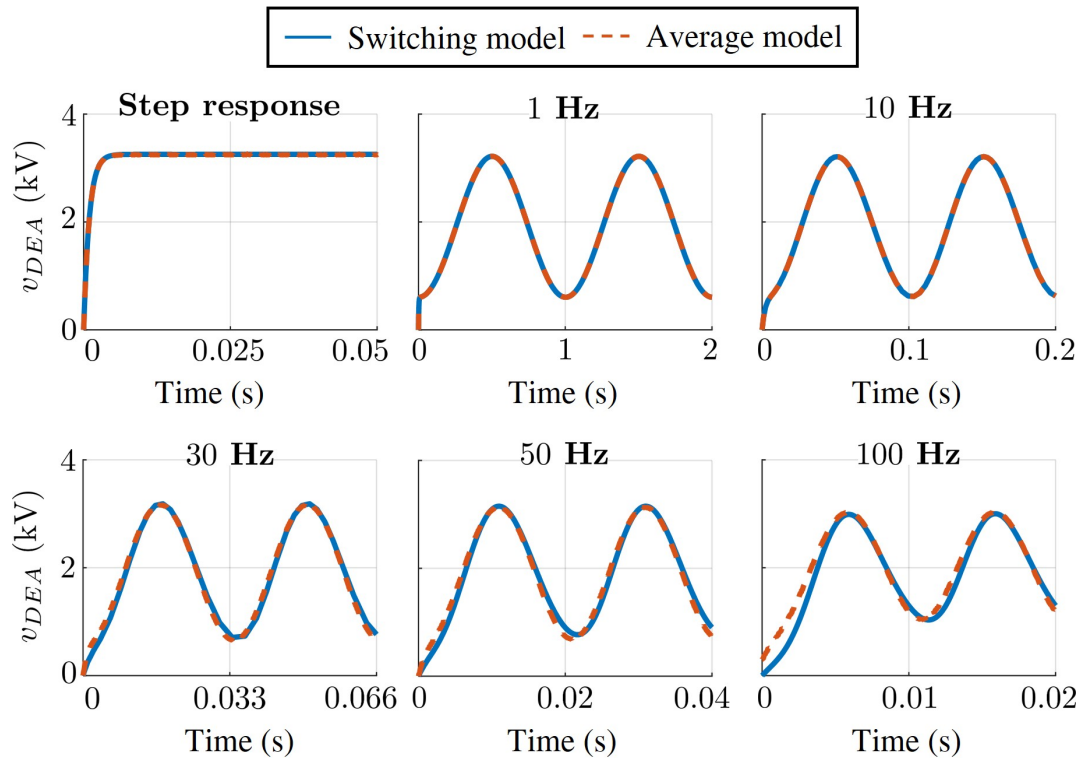


Figure 4.18: Validation in simulation of the average model, compared to the switching model. Different responses are shown: Step response, and dynamic response at 1 – 10 – 30 – 50 – 100 Hz.

## 4.5 Experimental validation

In this section, experiments will be carried out to validate model (4.59). First, the experimental setup will be described. Then, experimental results will be reported and compared with the model.

### 4.5.1 Experimental setup

The employed DEA setup is shown in Fig. 4.19. It consists in one DE strip (30 mm  $\times$  30 mm  $\times$  50  $\mu$ m, made of Wacker ELASTOSIL silicone material), connected to two springs representing the bias system (0.05 N/mm stiffness). This latter causes a 20% pre-stretch in the DEA, with a resulting actuation stroke of 1.8 mm upon activation with 3 kV. Linear springs were chosen as bias system instead of an



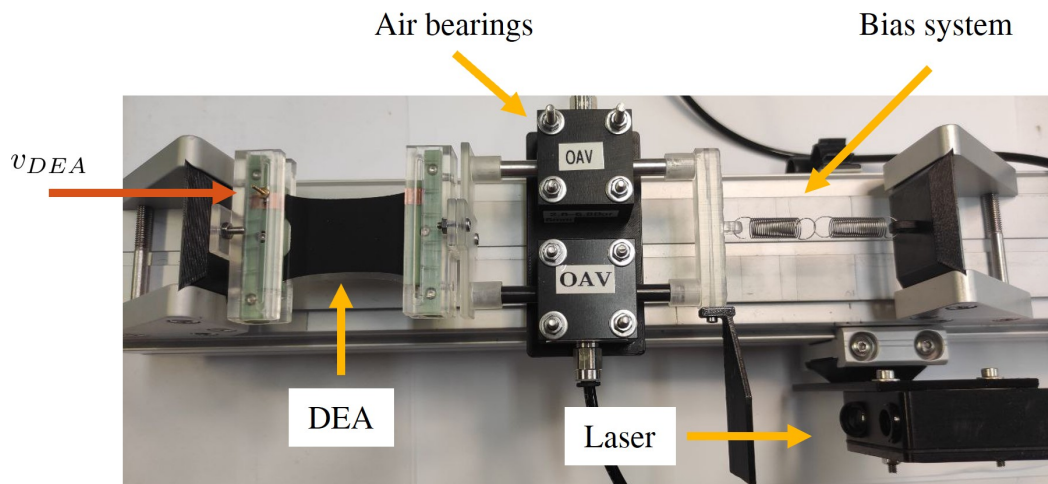


Figure 4.19: DEA linear movement setup.

NBS (discussed in 2.3) for simplicity of implementation, since it is not the primary goal maximizing the DEA's displacement. Two 6 mm Frictionless Air Bushing (OAV006MB) in Aluminum Housing Blocks (MBi0250) are in between the DEA and the springs, providing a frictionless motion. The DEA displacement is measured by a laser sensor (optoNCDT). The reconstructed capacitance in Fig. 4.14 is used as an input parameter to the model.

Fig. 3.1 shows that the command signals of the circuit are the two PWM signals, one to the half-bridge driver, which controls the charging stage, and one to transistor  $T_3$ , which controls the discharging stage. Those signals are generated by the STM32 NUCLEO-F446RE board at a frequency  $f_{PWM} = 15$  kHz.

## 4.5.2 Experimental results

For this validation, two sets of experiments are considered, obtained by modulating a square and sine wave with an input PWM signal of 15 kHz. The maximum fixed voltage in both cases is 6 V. For each experiment, the input voltage is recorded alongside the DEA voltage and displacement, the latter estimates the DEA capacitance. The input voltage and the DEA capacitance are then used in model (4.59). First, two input square waves with amplitude of 4 V and 6 V are considered at 1 and 2 Hz, as in Fig. 4.20 - 4.21. Between the input and output voltage, a static gain of 500 is observed. It can also be noted how the circuit time constant differs between rising and falling fronts, and in particular how the falling front exhibits a dual-phase discharging behavior as outlined in Section 4.2.3. The results show that the developed model well predicts the behavior of both rising and falling fronts of the DEA voltage for different input amplitudes.

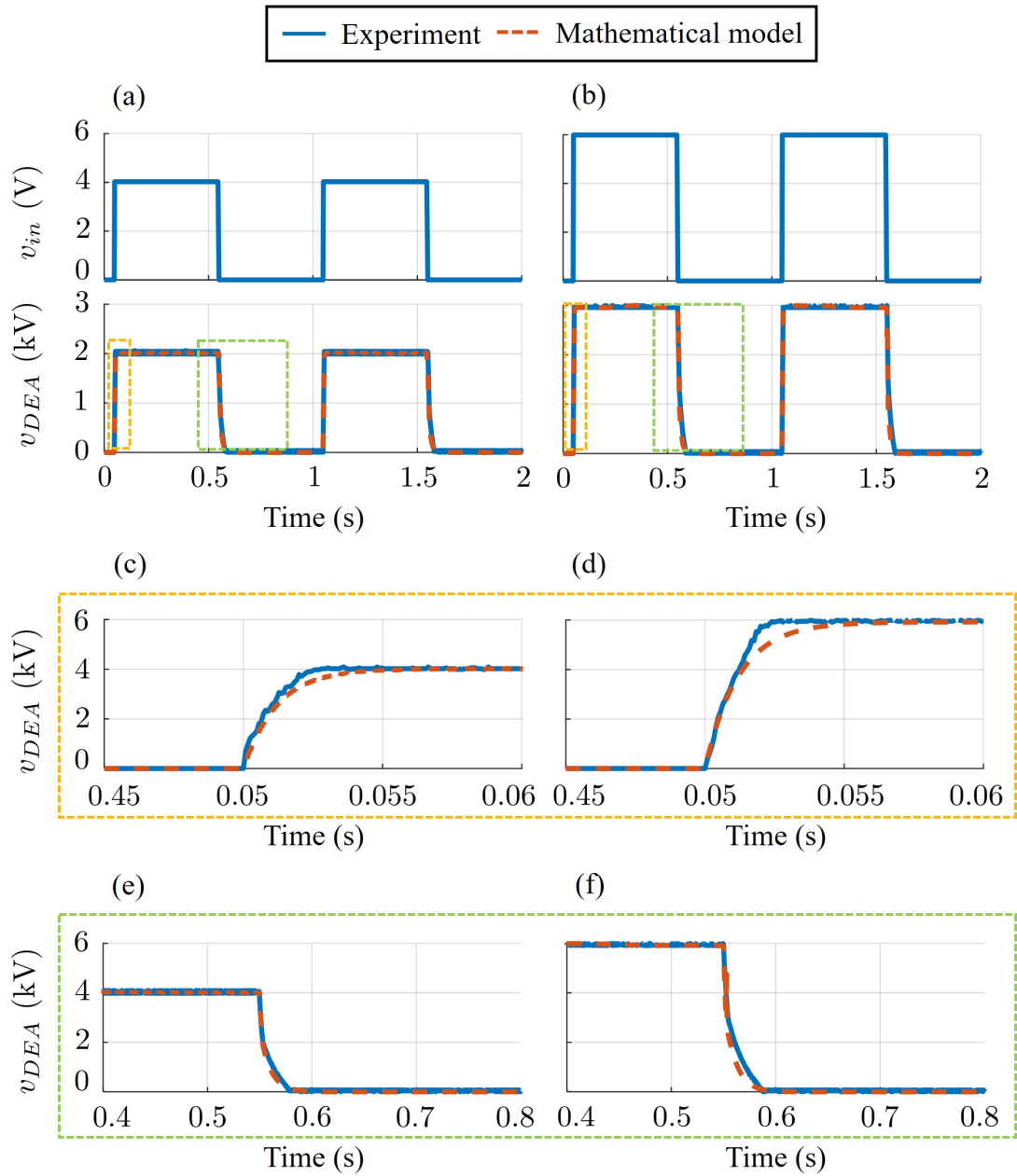


Figure 4.20: Experimental results and mathematical model validation. (a) - (b) Square wave input of 4 V @ 1 Hz and 6 V @ 1 Hz; (c) - (d) Zoom of the rising front; (e) - (f) Zoom of the falling front.

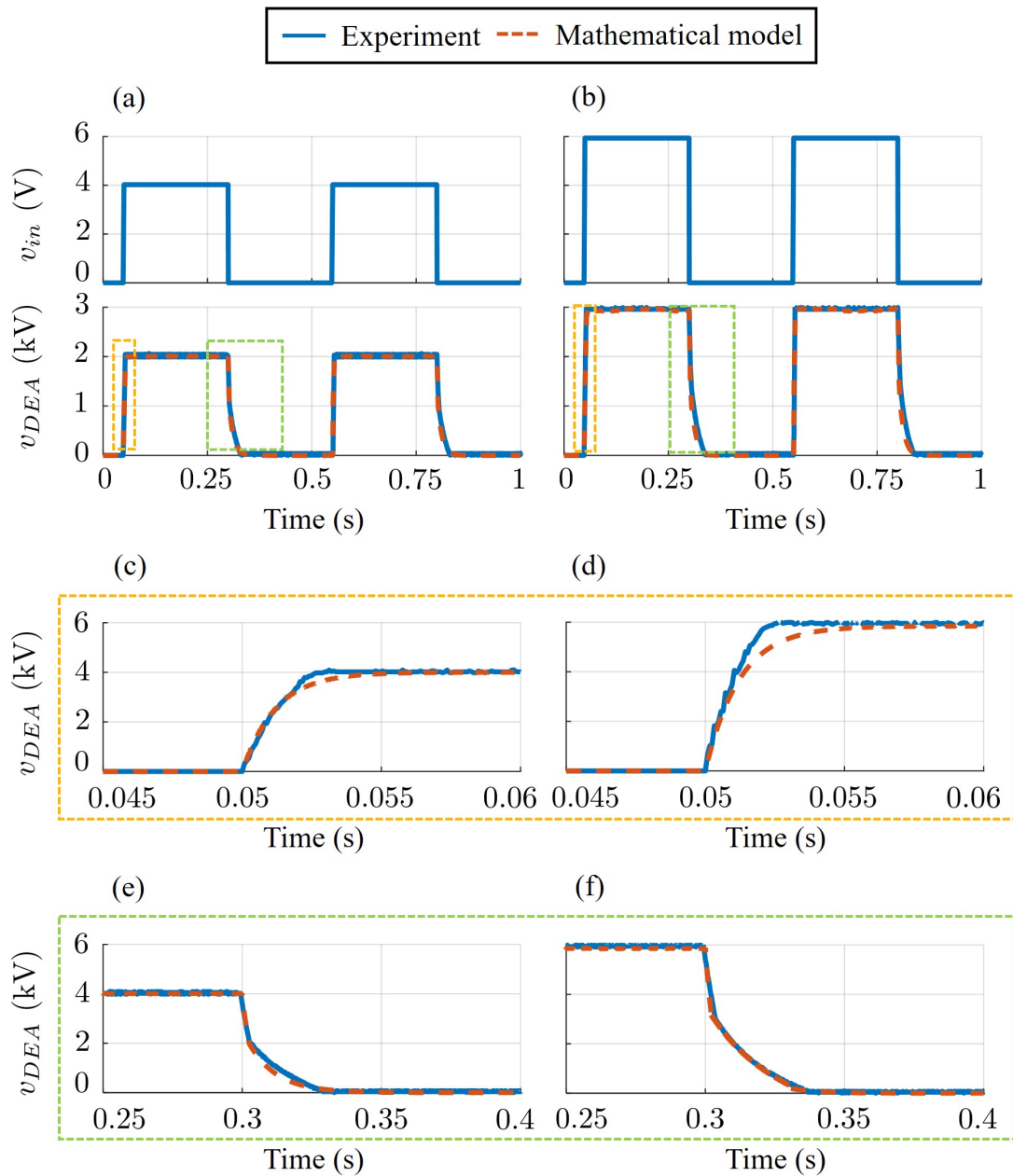


Figure 4.21: Experimental results and mathematical model validation. (a) - (b) Square wave input of 4 V @ 2 Hz and 6 V @ 2 Hz; (c) - (d) Zoom of the rising front; (e) - (f) Zoom of the falling front.

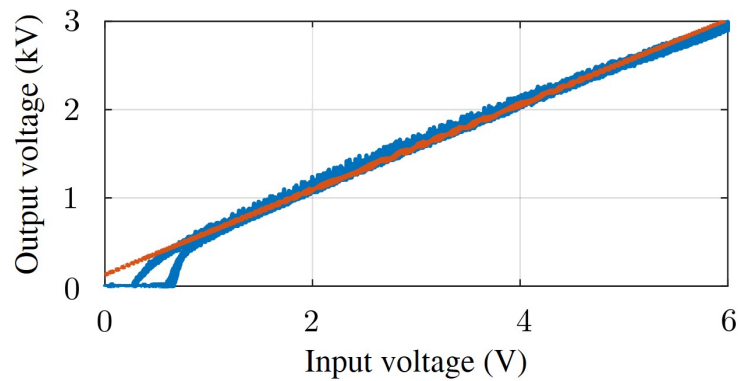


Figure 4.22: Input-output maps of the circuit subjected to a sinusoidal input @ 1 Hz.

A second set of experiments considers a sine wave with varying amplitude and frequency as input voltage. It is important to analyze the conditions under which the circuit is able to follow an input dynamic signal. To obtain a linear input/output relationship, it is essential that the input voltage has the minimum not below  $v_{in} \geq 1.2$  V in the case of dynamic inputs, as shown in Fig. 4.22. The characteristic input/output voltage of the DE employed in the setup was realized by applying a sinusoidal wave at 1 Hz, recording the input and the output voltages. By looking at the design of the circuit, it appears clear that the Greinacher circuit behaves linearly since it only doubles and rectifies the voltage without introducing phase shift thanks to the high voltage fast-switching diodes. Since TR is characterized by the windings relationship, which is linear, we conclude that the linearity of the resonant circuit mainly depends on the working mode of  $T_1$  and  $T_2$ . In particular, to guarantee that the two transistors work in saturation mode, i.e., at their full range, so that they can be considered as short circuits when they are ON, it must hold that  $v_{BE} = 1.2$  V (as from the datasheet). Hence, the input/output relationship is linear only in the case  $v_{in} \geq 1.2$  V. We point out, however, that losing the input voltage range from 0 to 1.2 V is not particularly detrimental for DEA applications. By considering an ideal input voltage range of 0 – 6 V and a practically achievable interval of 1.2 – 6 V, and by assuming that the actuation force is proportional to the square of the DEA voltage (due to the Maxwell stress (2.1)), the resulting 'lost' portion of the actuation force range is estimated to be  $1.2^2/6^2$ , i.e., only 4% of the theoretically achievable range. Based on the above discussion, we consider unipolar sine waves at 1 and 2 Hz with maximum value of 4 V and 6 V and a minimum value of 1.2 V, as in Fig. 4.23. Also in this case the model shows outstanding prediction performances.

Additionally, the circuit's performances have been investigated by considering pseudo-random input signals. To this end, three different voltage signals ranging within 1.5 – 5 V have been considered, each one consisting of the sum of 10 sinusoidal waves with randomly chosen amplitude, phase, and frequency (within 0 – 100 Hz). The corresponding results are shown in Fig. 4.24. It can be seen that the mathematical model matches quite well the experiments in every case.

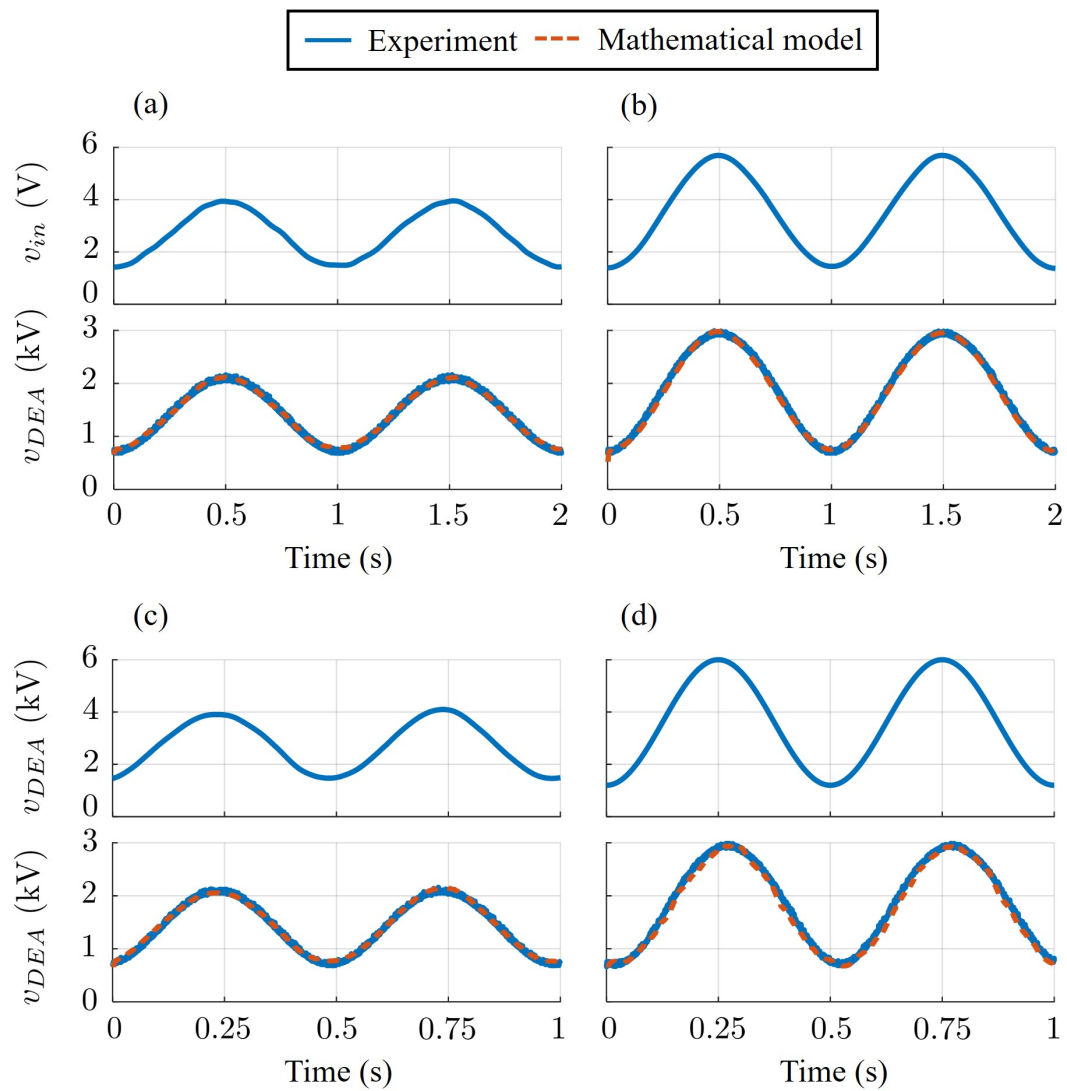


Figure 4.23: Experimental results and mathematical model validation. (a) - (b) Sinusoidal wave input of 4 V and 6 V @ 1 Hz; (c) - (d) Sinusoidal wave input of 4 V and 6 V @ 2 Hz.

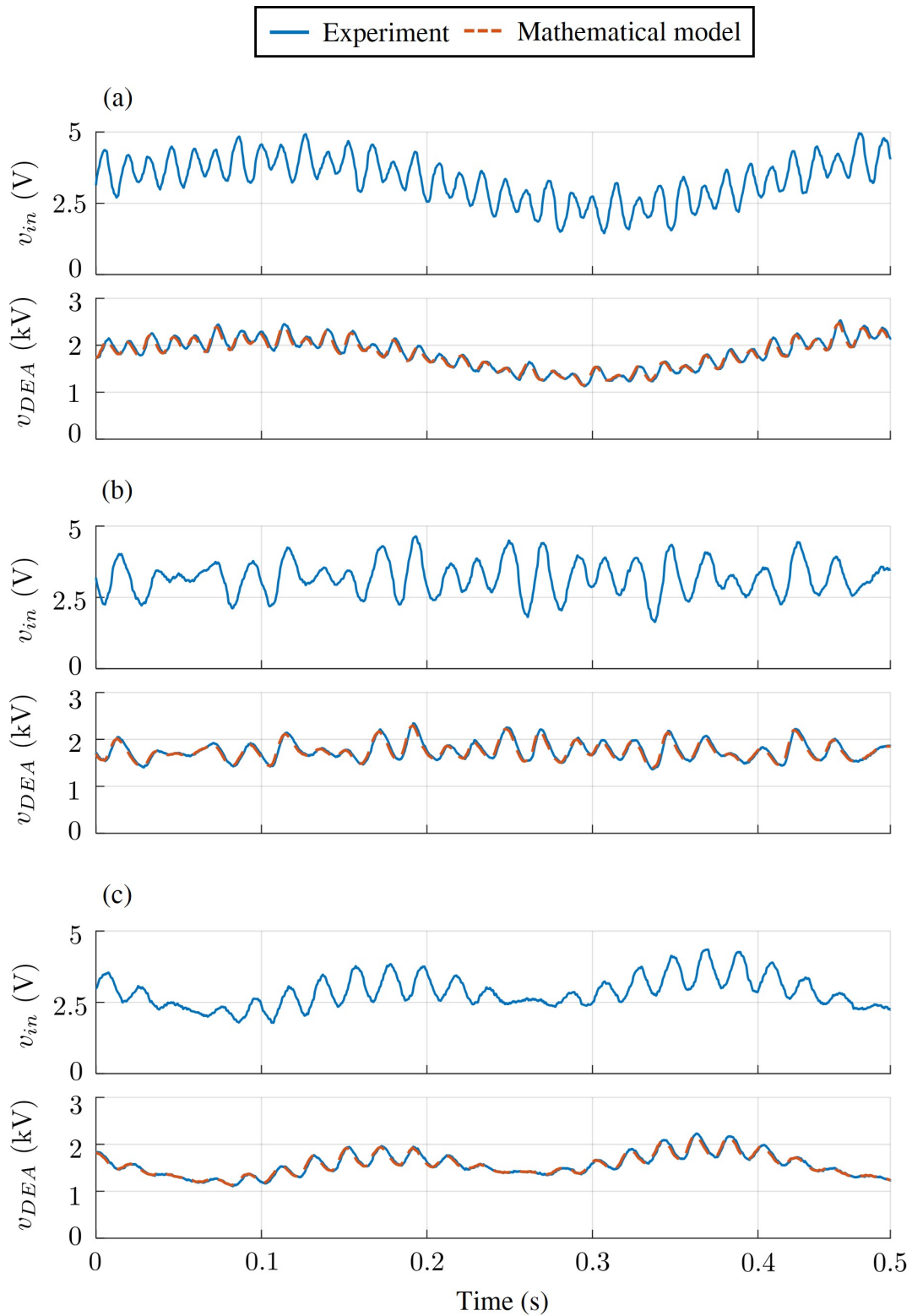


Figure 4.24: Comparison between experiments and mathematical model when multi-amplitude and multi-frequency signals are applied to the circuit. Three different randomly-generated signals are considered in (a), (b), and (c), with the input signals and the corresponding output voltages reported in the upper and lower rows, respectively.

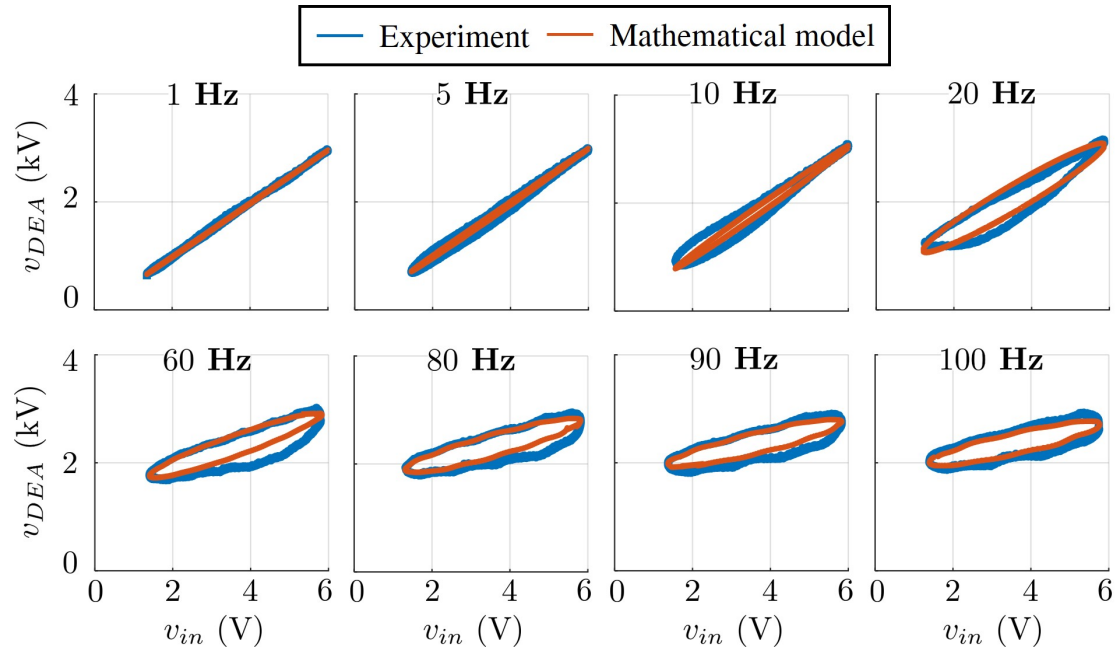


Figure 4.25: Input-output maps of the circuit subjected to sinusoidal inputs at different frequencies, from 1 Hz to 100 Hz.

Moreover, we analyze the performance of the circuit based on the obtained results. By measuring the input-output map of the circuit at different frequencies (up to 100 Hz), as in Fig. 4.25, the cutoff frequency is determined as the frequency at which the amplitude of a sinusoidal output is attenuated by a factor of  $1/\sqrt{2}$  (corresponding to a gain of  $-3\text{dB}$ ) compared to the DC case. According to this definition, the bandwidth of the circuit is about 40 Hz. The energy efficiency of the circuit is also quantified experimentally, based on an input voltage signal transitioning from 0 V to a constant value of 6 V, and considering the capacitive load to be fully discharged at the beginning of the test. The energy efficiency  $\eta$  is quantified as the ratio between the energy stored in the capacitive load,  $E_{out}$ , and the input energy supplied to the circuit,  $E_{in}$ , during the time  $T_{99\%}$  needed to charge the capacitor from 0 V up to 99% of its steady value, according to the following equation:

$$\eta = \frac{E_{out}}{E_{in}} = \frac{\frac{1}{2}C_{DEA}v_{out}^2(T_{99\%})}{\int_0^{T_{99\%}} v_{in}(t)i_{in}(t)dt}. \quad (4.68)$$

The experimentally measured energy efficiency equals 38.5%. In literature, higher efficiency values have been reached, such as 88 – 90% in [69], and 54% in [51]. In those works, however, the focus was on developing high-efficiency electronics, while the aim of this work is to develop and model a small-size/-cost electronic. Taking this fact into account, the obtained energy efficiency value of  $\sim 40\%$  is regarded as acceptable.

Finally, the accuracy of the model is quantified by using the following  $FIT\%$  index, which represents a normalized root mean squared error expressed as a per-

Type	Amplitude (V)	Frequency (Hz)	FIT (%)
Square wave	0 - 4	1	93.63
Square wave	0 - 4	2	92.06
Square wave	0 - 6	1	93.45
Square wave	0 - 6	2	93.69
Sine wave	1.2 - 4	1	93.14
Sine wave	1.2 - 4	2	93.64
Sine wave	1.2 - 6	1	94.54
Sine wave	1.2 - 6	2	93.27
Sine wave	1.2 - 6	5	92.04
Sine wave	1.2 - 6	10	80.85
Sine wave	1.2 - 6	20	79.16
Sine wave	1.2 - 6	60	79.58
Sine wave	1.2 - 6	80	86.26
Sine wave	1.2 - 6	90	86.55
Sine wave	1.2 - 6	100	87.03
Multi-freq. random signal (a)	1.5 - 5	0 - 100	79.52
Multi-freq. random signal (b)	1.5 - 5	0 - 100	82.46
Multi-freq. random signal (c)	1.5 - 5	0 - 100	85.31

Table 4.2:  $FIT_{\%}$  values for each validation experiment.

centage. It is computed as:

$$FIT_{\%} = 100 \left( 1 - \frac{\|y - \hat{y}\|}{\|y - \bar{y}\|} \right), \quad (4.69)$$

where  $y$ ,  $\hat{y}$ , and  $\bar{y}$  are respectively the measured, predicted, and average values of signal  $y$ , while  $\|y\|$  denotes the L2-norm of  $y$ . A  $FIT_{\%}$  higher than 79% is obtained in each test, as reported in Table 4.2, quantitatively confirming the accuracy of our model.



# Chapter 5

## Control

Developing feedback controllers for high voltage driving circuits in dielectric elastomers is crucial for several reasons. The performance of DEAs is highly sensitive to voltage fluctuations and environmental conditions, such as temperature and humidity. Without precise control, these fluctuations can lead to instability, suboptimal performance, or even damage to the elastomers. Feedback controllers help maintain the desired voltage levels and compensate for disturbances, ensuring reliable, safe, and efficient operation.

In this chapter linear feedback voltage control law based on a linearization of the average model and nonlinear feedback voltage control law based on the average model (4.65) will be presented in Section 5.1 and Section 5.2, respectively. The main control design objective is to obtain an accurate tracking of the output voltage  $v_{DEA}$  for arbitrary signals at various amplitudes and frequencies maintaining the error below a certain threshold and within a certain bandwidth. The linear voltage control will be developed by inverting the dynamic of the system and imposing a new one ensuring a voltage error  $\varepsilon < 1\%$  up to 100 Hz. The nonlinear voltage controller will aim of perusing a certain trajectory of the system's state. An LMI optimization will be used to find control gains by solving the LMI on each vertex. The validation of the developed control laws in simulation and experimentally will be carried out and discussed. Finally, the voltage controllers will be validated in simulation in Section 5.3 and experimentally in Section 5.4. The theory and results of the linear voltage controller are presented in the author's conference paper [3]. A journal paper is in preparation, to report the theory and the experimental result of the nonlinear controller.

### 5.1 Linear voltage control

To enable the design of a linear control algorithm aimed at tracking various DEA motion trajectories, an accurate voltage control of the HV circuit is necessary. To this purpose, a linearized model of the average model (4.65) will be developed.

### 5.1.1 Linearized model

To enable the design of a linear control algorithm aimed at tracking various DEA motion trajectories, an accurate voltage control of the HV circuit is necessary. A small-signal model is developed by linearizing the nonlinear average system in (4.65) around a given quiescent operating condition. Given an output voltage at the steady-state  $v_{DEA,av}^q$ , the corresponding quiescent values of the duty-cycle  $\alpha^q$  and the average electrical charge  $\zeta_{av}^q$  are computed by solving (4.65) at the steady state. Then, the small-signal portions are defined as follows

$$x = \zeta_{av} - \zeta_{av}^q, \quad y = v_{DEA,av} - v_{DEA,av}^q, \quad u = \alpha - \alpha^q. \quad (5.1)$$

The small signal LTI model is provided as

$$\begin{cases} \dot{x} &= -ax + bu \\ y &= cx + du \end{cases}, \quad (5.2)$$

where

$$\begin{aligned} a &= -\left. \frac{\partial f}{\partial \zeta_{av}} \right|_{(\zeta_{av}, \alpha) = (\zeta_{av}^q, \alpha^q)}, & b &= \left. \frac{\partial f}{\partial \alpha} \right|_{(\zeta_{av}, \alpha) = (\zeta_{av}^q, \alpha^q)}, \\ c &= \left. \frac{\partial g}{\partial \zeta_{av}} \right|_{(\zeta_{av}, \alpha) = (\zeta_{av}^q, \alpha^q)}, & d &= \left. \frac{\partial g}{\partial \alpha} \right|_{(\zeta_{av}, \alpha) = (\zeta_{av}^q, \alpha^q)}. \end{aligned} \quad (5.3)$$

To enhance clarity in subsequent sections, the minus sign in front of  $a$  is explicitly denoted. In this way,  $a$ ,  $b$ ,  $c$ , and  $d$  all have positive signs. It is noteworthy that matrix  $d$  has a relatively low value compared to the other state-space matrices. This aspect should be considered during the controller development phase because a non-zero  $d$  introduces a zero in the model's transfer function. If this zero is small, it can lead to significant overshooting in the control action.

### 5.1.2 Linear controller

A linear control algorithm is developed to allow the HV circuit to track arbitrary trajectories defined around the quiescent operating point. As a first step, the linear model (5.2) is converted into an input-output differential equation

$$\begin{aligned} \dot{y} &= c\dot{x} + d\dot{u} = -cax + cbu + d\dot{u} = -ay + cbu + adu + d\dot{u} \\ \dot{y} &= -ay + (ad + cb)u + d\dot{u}. \end{aligned} \quad (5.4)$$

By inverting this dynamic and injecting a control action that depends on both the tracking error  $e_v$  and its integral  $\int e_v$ , the following control input is derived:

$$\begin{cases} \dot{z} &= -\left(a + \frac{cb}{d}\right)z + \frac{1}{d}\left(ay + \lambda_p(y^* - y) + \lambda_i \int (y^* - y)dt + \dot{y}^*\right), \\ u &= z \end{cases}, \quad (5.5)$$

where  $y^*$  is the desired voltage trajectory, while  $\lambda_p > 0$  and  $\lambda_i > 0$  are free control design parameters that influence the internal stability of the system, which is described by the roots of the polynomial  $s^2 + \lambda_p s + \lambda_i = 0$ . By substituting (5.5) into (5.4) and considering the system (5.2) we obtain:

$$\dot{y} = -ay + (ad + cb)u + d\dot{u} = \lambda_p(y^* - y) + \lambda_i \int (y^* - y)dt + \dot{y}^*. \quad (5.6)$$

The transfer function of the closed-loop system when (5.5) is applied is derived by applying the Laplace transformation to (5.6):

$$T(s) = \frac{Y(s)}{Y^*(s)} = \frac{s + \lambda_p + \frac{\lambda_i}{s}}{s + \lambda_p + \frac{\lambda_i}{s}} = 1. \quad (5.7)$$

Finally, while (5.5) ensures that the transfer function  $G(s)$  from  $y^*$  to  $y$  remains identically equal to 1, its practical implementation can pose challenges. In practice, the model in (5.5) exhibits a pole in  $-(a + \frac{cb}{d})$ , which coincides with the system open-loop zero. When considering the values in (4.62), along with  $\alpha^q = 0.5$  and  $v_{DEA,av}^q = 1500$  V, we obtain  $a = 576$ ,  $b = 3620$ ,  $c = 562$ , and  $d = 16.5$ , which in turn lead to a zero for system (5.4) (i.e., an eigenvalue for controller (5.5)) having a natural frequency of 20 kHz.

Clearly, for practical implementation in discrete-time, this very fast controller dynamics would necessitate very high sampling frequencies. Figure 5.1 compares the resulting closed-loop responses of the system when the controller is continuous and when it is discretized with three different sampling times. Parameters  $\lambda_p$  and  $\lambda_i$  are chosen so that the closed-loop eigenvalues are complex-conjugated with a natural frequency of 80 Hz and a damping ratio of 0.7. It becomes evident that reasonable sampling frequencies for a low-cost device (up to 15-20 kHz) would render the closed-loop implementation of such an ideal controller unstable.

To address this issue, we consider a simplified implementation of controller (5.5) in which  $d \rightarrow 0$ , given as follows:

$$u = \frac{1}{cb} \left( ay + \lambda_p(y^* - y) + \lambda_i \int (y^* - y)dt + \dot{y}^* \right). \quad (5.8)$$

Note that, differently from (5.5), controller (5.8) no longer exhibits fast internal dynamics. By combining (5.8) with (5.2) and transforming in the Laplace domain, we obtain the closed-loop transfer function  $T(s)$  as

$$T(s) = \frac{Y(s)}{Y^*(s)} = \frac{ds^3 + \alpha_1 s^2 + \alpha_2 s + h\lambda_i}{\beta_1 s^2 + \beta_2 s + h\lambda_i}, \quad (5.9)$$

with

$$\begin{aligned} h &= ad + cb, & \alpha_1 &= d\lambda_p + h, & \alpha_2 &= d\lambda_i + h\lambda_p, \\ \beta_1 &= -ad + cb + d\lambda_p, & \beta_2 &= abc + \lambda_i d - ah + h\lambda_p. \end{aligned} \quad (5.10)$$

The lack of causality in (5.9) results from the dependency of the control input on the derivative of the reference trajectory, which does not pose a limitation if  $y^*$  is

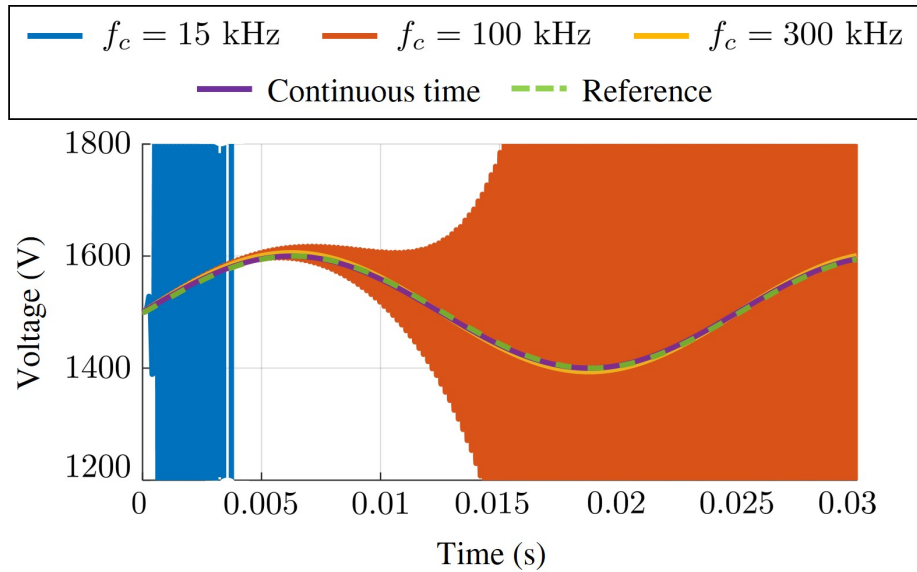


Figure 5.1: Closed-loop response comparison when the dynamic inversion controller is continuous and discretized with three different sampling times.

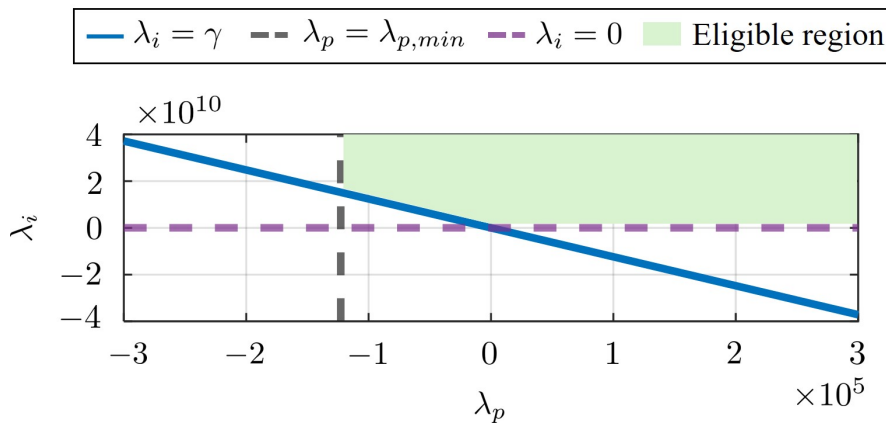


Figure 5.2: Eligible region for selecting  $\lambda_p$  and  $\lambda_i$ .

known a priori. To ensure closed-loop stability of (5.9), it must result that:

$$\begin{aligned}
 I. \quad & \beta_1 > 0 \rightarrow cb - ad + d\lambda_p > 0 \rightarrow \lambda_p > \lambda_{p,min} \\
 II. \quad & \beta_2 > 0 \rightarrow \lambda_i > \gamma - \frac{h\lambda_p}{d} \\
 III. \quad & h\lambda_i > 0 \rightarrow \lambda_i > 0
 \end{aligned} \tag{5.11}$$

where  $\lambda_{p,min} = a - \frac{cb}{d}$  and  $\gamma = a^2$ . Therefore, the conditions for stability can be summarized as

$$\begin{cases} \lambda_p > \lambda_{p,min}, \\ \lambda_i > \max\left(0, \gamma - \frac{h\lambda_p}{d}\right). \end{cases} \tag{5.12}$$

For instance, in Fig. 5.2, the eligible region for  $\lambda_p$  and  $\lambda_i$  is illustrated, considering the previously reported values of  $a$ ,  $b$ ,  $c$ , and  $d$ . To successfully track a desired

trajectory, the ideal closed-loop transfer function should be 1. However, due to the fact that the controller has been designed by assuming that  $d = 0$ , this condition is no longer met for every frequency. To quantify the effect of this approximation, we can rewrite the closed-loop transfer function (5.9) as  $T(s) = 1 + T_d(s)$ , where  $T_d(s)$  accounts for the deviation to the ideal dynamic inversion introduced by imposing  $d = 0$  in the controller, given as

$$T_d(s) = T(s) - 1 = \frac{ds(s+a)^2}{\beta_1 s^2 + \beta_2 s + h\lambda_i}. \quad (5.13)$$

To tune  $\lambda_p$  and  $\lambda_i$ , we strive to minimize the amplitude of (5.13) as much as possible within a frequency range of interest, which defines a desired tracking bandwidth. Here, given the open-loop circuit bandwidth of 40 Hz, we consider a frequency range of 0 – 100 Hz. Hence, we select the controller gains  $\lambda_p$  and  $\lambda_i$  satisfying (5.11) which lead to a nearly unitary gain of the closed-loop transfer function at the frequency of  $f_0 = 100$  Hz. This is attained by ensuring that  $T_d(s)$  has a corresponding amplitude that restricts the tracking error to below 1% in the desired tracking bandwidth. Thus, the control design has to satisfy the condition:

$$|T_d(j2\pi f_0)| = 0.01 \equiv -40 \text{ dB}. \quad (5.14)$$

By imposing (5.14), and selecting identical closed-loop poles  $p_1$  and  $p_2$  to simplify the problem, the values  $p_1 = p_2 = -306$  rad/s are determined. From the characteristic polynomial of (5.9) the control parameters can be derived as follows:

$$P(s) = \frac{s^2}{\beta_1} + \frac{\beta_2}{\beta_1}s + \frac{h\lambda_i}{\beta_1} = s^2 + \underbrace{(p_1 + p_2)}_p s + p_1 p_2, \quad (5.15)$$

thus, by using (5.10)

$$\begin{aligned} \frac{h\lambda_i}{\beta_1} = p_1 p_2 &\rightarrow \lambda_i = \frac{p_1 p_2}{h} (cb - ad + d\lambda_p), \\ \frac{\beta_2}{\beta_1} = p &\rightarrow \frac{h\lambda_i}{cb - ad + d\lambda_p} \rightarrow (h - pd)\lambda_p = pcb - pad - cba - \lambda_i d + ah. \end{aligned} \quad (5.16)$$

By substituting  $\lambda_i$  in  $\lambda_p$ , we obtain:

$$\begin{aligned} \lambda_p &= \frac{n_2}{n_1}, \\ \lambda_i &= \frac{p_1 p_2}{h} \left( cb - ad + \frac{dn_2}{n_1} \right). \end{aligned} \quad (5.17)$$

For  $p_1 = p_2 = -306$  rad/s, the parameters are:

$$\begin{aligned} \lambda_p &= 650, \\ \lambda_i &= 9.3 \times 10^4, \end{aligned} \quad (5.18)$$

Figure 5.3 shows the resulting amplitude diagrams of  $T(s)$  and  $T_d(s)$ . Note that, with the provided controller, the amplitude of  $T(s)$  is guaranteed to stay within the specified error threshold of 1% within the range 0 – 100 Hz.

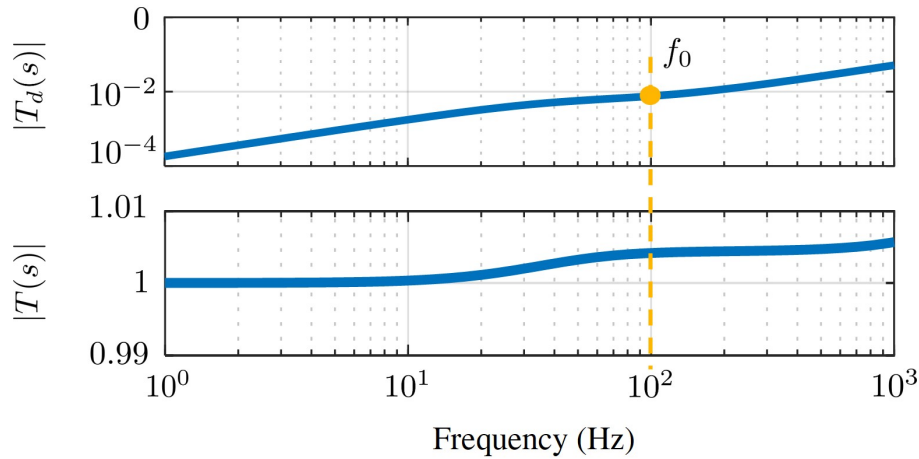


Figure 5.3: Bode diagrams of  $T_d(s)$  and  $T(s)$ , with  $f_0 = 100$  Hz and  $p_1 = p_2 = -306$  rad/s.

## 5.2 Nonlinear voltage control

Linear controllers, such as (5.8), are widely used due to their simplicity and ease of implementation. They are particularly effective in systems that operate within a narrow range of conditions where the system dynamics can be approximated as linear. However, the HV circuit here discussed needs to provide an output voltage in the range  $0 - 3000$  V, thus it operates for large-amplitude signals. Moreover, the circuit presents inherently nonlinearities, exhibiting behaviors that cannot be accurately captured by linear models, especially under varying operating conditions and large signal perturbations. In this context, the importance of a nonlinear controller becomes evident. In fact, nonlinear control techniques allow the output voltage to follow large-amplitude signals with higher precision. On the other hand, the complex structure of the model makes the development of nonlinear controllers challenging.

The nonlinear controller proposed in this work is based on the idea of controlling the output voltage  $v_{DEA}$  by imposing a closed-loop control on the system's state. The average model (4.65) can be rewritten as follows:

$$\begin{cases} \dot{\zeta}_{av} = f(\zeta_{av})\zeta_{av} + g(\zeta_{av})\alpha \\ v_{DEA} = h(\zeta_{av})\zeta_{av} + l(\zeta_{av})\alpha \end{cases}, \quad (5.19)$$

where

$$\begin{aligned} f(\zeta_{av}) &= -A_d^C, & g(\zeta_{av}) &= B_d^C \bar{v}_{in} + \left( (A_d^C - A_c^C)\zeta + (B_c^C - B_d^C)\bar{v}_{in} \right)\alpha, \\ h(\zeta_{av}) &= C_d^C, & l(\zeta_{av}) &= (C_c^C - C_d^C)\zeta_{av}, \end{aligned} \quad (5.20)$$

$\alpha$  is the duty-cycle,  $\bar{v}_{in} = 6$  V, and the state space matrices' values are those reported in (4.62). Note that the signs of  $A_d$  and  $A_c$  are explicitly defined. For simplicity, the apex  $C$  will be omitted. The presence of the term  $l(\zeta_{av})$  renders the model less compatible with many conventional control strategies, such as sliding mode control. Additionally,  $l(\zeta_{av})$  approaches zero in a manner analogous to the matrix

$d$  in the linear model, since  $C_c - C_d \approx 0$ . Consequently, a control strategy based on the inversion of the system dynamics becomes infeasible. This is because the control input would escalate to impractically high values due to the near-zero  $l(\zeta_{av})$ , thereby making the controller inapplicable. One possible approximation consists in considering  $l(\zeta_{av}) = 0$ , analogous to what was done in the linear case. From now on, the state space vector  $\zeta_{av}$  will be named for simplicity  $\zeta$ .

Given a desired output voltage trajectory,  $v_{DEA}^*(t)$ , the output error is defined as  $\tilde{y} = v_{DEA}^* - v_{DEA}$ . A corresponding state trajectory is defined by considering  $(C_c - C_d) = 0$ , i.e.,

$$\zeta^*(t) = \frac{1}{C_d} v_{DEA}^*(t). \quad (5.21)$$

The controller is defined such that it tracks the trajectory on the state,  $\zeta^*(t)$ . An additional term proportional to the integral of the output error is also introduced to account for the errors introduced by (5.21) and by model uncertainties. Thus, the controller is found by imposing that

$$\begin{cases} \dot{v} = \tilde{y} \\ \dot{\zeta} = -A_d \zeta + B_d \bar{v}_{in} + \left( (A_d - A_c) \zeta + (B_c - B_d) \bar{v}_{in} \right) \alpha \equiv -\lambda \tilde{x} + \dot{\zeta}^* - kv \end{cases}, \quad (5.22)$$

where  $v = \int \tilde{y} dt$  is the integral state error and  $\tilde{x} = \zeta^* - \zeta$  is the state error. The resulting controller is

$$\alpha = \frac{A_d \zeta - B_d \bar{v}_{in} - \lambda \tilde{x} + \dot{\zeta}^* - kv}{(A_d - A_c) \zeta + (B_c - B_d) \bar{v}_{in}}. \quad (5.23)$$

The closed-loop states are the integral of the output error  $v$  and the error  $\tilde{x}$ . Considering (5.22), the closed-loop dynamics of the state  $v$  is as follows:

$$\begin{aligned} \dot{v} &= v_{DEA}^* - v_{DEA} \\ &= v_{DEA}^* - C_d \zeta - (C_c - C_d) \zeta \alpha \\ &= \underbrace{v_{DEA}^* - C_d \zeta^*}_{=0} + C_d \tilde{x} - (C_c - C_d) \zeta \alpha \\ &= C_d \tilde{x} - (C_c - C_d) \zeta \left( \frac{A_d \zeta - B_d \bar{v}_{in} - \lambda \tilde{x} + \dot{\zeta}^* - kv}{(A_d - A_c) \zeta + (B_c - B_d) \bar{v}_{in}} \right) \\ &= C_d \tilde{x} + \frac{(C_c - C_d) \zeta}{(A_d - A_c) \zeta + (B_c - B_d) \bar{v}_{in}} \left( A_d \zeta - B_d \bar{v}_{in} - \lambda \tilde{x} + \dot{\zeta}^* - kv \right) \\ &= C_d \tilde{x} - \gamma(\zeta) \left( A_d \zeta - B_d \bar{v}_{in} - \lambda \tilde{x} + \dot{\zeta}^* - kv \right) \\ &= \left( C_d - \gamma(\zeta) \lambda \right) \tilde{x} - \gamma(\zeta) kv + \gamma(\zeta) \left( A_d \zeta - B_d \bar{v}_{in} + \dot{\zeta}^* \right) \\ &= -\gamma(\zeta) kv + \left( C_d - \gamma(\zeta) \lambda - \gamma(\zeta) A_d \right) \tilde{x} + \gamma(\zeta) \left( A_d \zeta^* + \dot{\zeta}^* - B_d \bar{v}_{in} \right), \end{aligned} \quad (5.24)$$

with  $\gamma(\zeta) = \frac{(C_c - C_d) \zeta}{(A_d - A_c) \zeta + (B_c - B_d) \bar{v}_{in}}$ . The closed-loop dynamics of the state  $\tilde{x}$  becomes

$$\dot{\tilde{x}} = \lambda \tilde{x} + kv \quad (5.25)$$

Thus, combining (5.24) and (5.25), the closed-loop system becomes the following:

$$\begin{bmatrix} \dot{v} \\ \dot{\tilde{x}} \end{bmatrix} = \begin{bmatrix} -\gamma(\zeta)k & C_d - \gamma(\zeta)\lambda - \gamma(\zeta)A_d \\ k & \lambda \end{bmatrix} \begin{bmatrix} v \\ \tilde{x} \end{bmatrix} + \begin{bmatrix} \gamma(\zeta) \\ 0 \end{bmatrix} (A_d\zeta^* + \dot{x}^* - B_d\bar{v}_{in}). \quad (5.26)$$

Based on (5.21), the exogenous input is written as

$$A_d\zeta^* + \dot{\zeta}^* - B_d\bar{v}_{in} = \frac{A_d}{C_d} \left( v_{DEA}^* + \frac{1}{A_d} \dot{v}_{DEA}^* - \frac{B_d C_d}{A_d} \bar{v}_{in} \right) = \frac{A_d}{C_d} \delta(v_{DEA}^*) \quad (5.27)$$

. Note that  $\delta(v_{DEA}^*)$ , in case of  $B_d = 0$ , represents the reference value filtered by a high-pass system featuring the open-loop pole.

Thus, (5.26) becomes

$$\begin{bmatrix} \dot{v} \\ \dot{\tilde{x}} \end{bmatrix} = \begin{bmatrix} -\gamma(\zeta)k & C_d - \gamma(\zeta)\lambda - \gamma(\zeta)A_d \\ k & \lambda \end{bmatrix} \begin{bmatrix} v \\ \tilde{x} \end{bmatrix} + \begin{bmatrix} \frac{A_d}{C_d} \gamma(\zeta) \\ 0 \end{bmatrix} \delta(v_{DEA}^*). \quad (5.28)$$

### 5.2.1 Linear Parameter-Varying system (LPV system) and Linear Matrix Inequality optimization (LMI optimization)

The model (5.28) is Linear Parameter-Varying (LPV), since its matrices depend linearly on  $\gamma(\zeta)$ . The bound on the state  $\zeta$  can be found by considering the steady-state values obtained with minimum and maximum input, i.e., duty-cycle  $\alpha = 0$  and  $\alpha = 1$ . From (5.19), the steady states are:

$$\begin{cases} \zeta = 0 & \text{when } \alpha = 0 \\ \bar{\zeta} = \frac{B_c}{A_c} \bar{v}_{in} & \text{when } \alpha = 1 \end{cases} \quad (5.29)$$

Note that  $B_d = 0$  in the model when  $\zeta = 0$ .

To show that the first-order dynamics in (5.19) is always bounded, i.e.,  $\underline{\zeta} \leq \zeta \leq \bar{\zeta}$ , for any  $\alpha$  in  $[0, 1]$ , the following needs to hold true:

$$\begin{cases} \dot{\zeta} \leq 0 & \forall \alpha \text{ and } \zeta = \bar{\zeta} \\ \dot{\zeta} \geq 0 & \forall \alpha \text{ and } \zeta = \underline{\zeta} \end{cases} \quad (5.30)$$

If  $\zeta = \bar{\zeta}$ , the dynamics is

$$\dot{\zeta} = -\frac{B_c A_d}{A_c} \bar{v}_{in} + (A_d - A_c) \frac{B_c}{A_c} \bar{v}_{in} \alpha + B_c \bar{v}_{in} \alpha = \frac{B_c A_d}{A_c} \bar{v}_{in} (\alpha - 1), \quad (5.31)$$

which is always negative as  $\alpha \leq 1$ . Instead, if  $\zeta = \underline{\zeta}$ , the dynamics is

$$\dot{\zeta} = B_c \bar{v}_{in} \alpha, \quad (5.32)$$

which is always positive. Thus, the state  $\zeta(t)$  is always bounded between 0 and  $\bar{\zeta}$ .

As  $\gamma$  depends on  $\zeta$ , the bounds (5.29) allow to define also upper and lower bounds of  $\gamma(\zeta)$ , i.e.,

$$\begin{cases} \underline{\gamma} = \gamma(\bar{\zeta}) = \frac{(C_c - C_d)}{A_d} < 0 \\ \bar{\gamma} = \gamma(\underline{\zeta}) = 0 \end{cases} \quad (5.33)$$



The system in (5.28) can be rewritten in an LPV form as follows

$$\begin{bmatrix} \dot{v} \\ \dot{\tilde{x}} \end{bmatrix} = [A(\gamma) - B_1(\gamma)K] \begin{bmatrix} v \\ \tilde{x} \end{bmatrix} + B_2(\gamma)\delta(v_{DEA}^*), \quad (5.34)$$

with

$$\begin{aligned} A(\gamma) &= \begin{bmatrix} 0 & -C_d - \gamma(\zeta)A_d \\ 0 & 0 \end{bmatrix}, & B_1(\gamma) &= \begin{bmatrix} \gamma(\zeta) \\ 1 \end{bmatrix}, \\ K &= [k \quad \lambda], & B_2(\gamma) &= \begin{bmatrix} \frac{A_d}{C_d}\gamma(\zeta) \\ 0 \end{bmatrix}, \end{aligned} \quad (5.35)$$

which is polytopic. This form allows to perform the design of a robust control law by using standard Linear Matrix Inequality (LMI) optimization [73]. By defining convex sets, LMI optimization techniques ensure that any local minimum found in the optimization process is also a global minimum. This property simplifies the optimization process and guarantees that the solution is optimal.

To manage systems with model uncertainties and external disturbances, such as model (5.34), one possible optimization strategy is the  $\mathcal{H}_\infty$  infinity norm control. It is a robust control strategy that aims to minimize the worst-case gain (infinity norm) from the disturbance input to the controlled output. It is important to specify that the frequency domain interpretation of the  $\mathcal{H}_\infty$  norm is only valid for LTI systems. In this case, the model (5.34) is an LPV model, thus the minimization of the infinity norm gives only a qualitative understanding of the tracking performance. To preprocess the disturbance input, often a shaping filter is used. In this case, an  $\mathcal{H}_\infty$  control strategy with shaping filter is exploited to found the control gains.

A shaping filter  $W(s)$  is considered, defined via the following upper bound function:

$$W^{-1}(s) = \frac{A_\infty s}{s + \omega_b \sqrt{\frac{A_\infty^2}{A_b^2} - 1}}, \quad (5.36)$$

where  $A_\infty$ ,  $A_b$ , and  $\omega_b$  are defined as

$$\begin{aligned} |W^{-1}(j0)| &= 0 \\ |W^{-1}(j\omega_b)| &= A_b, \\ |W^{-1}(j\infty)| &= A_\infty \end{aligned} \quad (5.37)$$

where  $A_\infty$  is the high-frequency gain,  $A_b$  is the gain at frequency  $\omega_b$ , with  $A_b \leq A_\infty$ . In other words, the filter  $W(s)$  weights the error due the exogenous input for frequencies higher than  $\omega_b$ .

The output  $z$  of the shaping filter, when the voltage tracking error  $\tilde{y}$  is considered as input becomes

$$z = W(s)\tilde{y} = \frac{s + \omega_b \sqrt{\frac{A_\infty^2}{A_b^2} - 1}}{A_\infty s} \tilde{y} = \frac{1}{A_\infty} \tilde{y} + \frac{\omega_b \sqrt{\frac{A_\infty^2}{A_b^2} - 1}}{A_\infty} \frac{\tilde{y}}{s} = \frac{1}{A_\infty} \dot{v} + \frac{\omega_b \sqrt{\frac{A_\infty^2}{A_b^2} - 1}}{A_\infty} v. \quad (5.38)$$

The state-space representation of the shaping filter is given by considering (5.24):

$$\begin{aligned}
z &= \frac{1}{A_\infty} \left( \left( -C_d - \gamma(\zeta)A_d \right) \tilde{x} - \gamma(\zeta)kv - \gamma(\zeta)\lambda\tilde{x} + \frac{A_d}{C_d}\gamma(\zeta)\delta(y^*) \right) + \frac{\omega_b \sqrt{\frac{A_\infty^2}{A_b^2} - 1}}{A_\infty} v \\
&= \left[ -\frac{1}{A_\infty}\gamma(\zeta)k + \frac{\omega_b \sqrt{\frac{A_\infty^2}{A_b^2} - 1}}{A_\infty} \quad -\frac{1}{A_\infty}\gamma(\zeta)\lambda - \frac{1}{A_\infty}(C_d + \gamma(\zeta)A_d) \right] \begin{bmatrix} v \\ \tilde{x} \end{bmatrix} + \frac{1}{A_\infty} \frac{A_d}{C_d} \gamma(\zeta) \delta(y^*) \\
&= \left( C(\gamma) - D_1 \begin{bmatrix} k & \lambda \end{bmatrix} \right) \begin{bmatrix} v \\ \tilde{x} \end{bmatrix} + D_2 \delta(y^*),
\end{aligned} \tag{5.39}$$

with

$$C(\gamma) = \frac{1}{A_\infty} \left[ \omega_b \sqrt{\frac{A_\infty^2}{A_b^2} - 1} \quad -C_d - \gamma(\zeta)A_d \right], \quad D_1(\gamma) = -\frac{\gamma(\zeta)}{A_\infty}, \quad D_2(\gamma) = \frac{A_d \gamma(\zeta)}{C_d A_\infty}. \tag{5.40}$$

The control gain  $K = [k \ \lambda]$  is found so that the following conditions are satisfied:

- **$\mathcal{H}_\infty$  specification:** Considering (5.34), the  $\mathcal{L}_2$  gain from the exogenous input  $\delta(y^*)$  to the filter's output  $z$  is kept smaller than 1. Doing so, the error caused by  $\delta(y^*)$  is minimized.
- **$\mathcal{H}_2$  specification:** Considering (5.39), the  $\mathcal{H}_2$  norm of the transfer function from  $\delta(y^*)$  to  $u$  is minimized. Thus, the control energy, i.e., control effort, is minimized.

The following LMI optimization problem is set and solved in each vertex:

Find  $Y \in \mathbb{R}^{1 \times 2}$ ,  $M \in \mathbb{R}$ , and  $P \in \mathbb{R}^{2 \times 2}$  s.t.

$$\left\{ \begin{array}{l} P \succ 0 \\ M > 0 \\ \begin{bmatrix} A(\gamma)P + PA(\gamma)^\top - B_1(\gamma)Y - Y^\top B_1(\gamma)^\top & B_2(\gamma) & PC(\gamma)^\top - Y^\top D_1(\gamma)^\top \\ & B_2(\gamma)^\top & -I & D_2(\gamma)^\top \\ & C(\gamma)P - D_1(\gamma)Y & D_2(\gamma) & -I \end{bmatrix} \prec 0 \\ \begin{bmatrix} A(\gamma)P + PA(\gamma)^\top - B_1(\gamma)Y - Y^\top B_1(\gamma)^\top & B_2(\gamma) \\ & B_2(\gamma)^\top & -I \end{bmatrix} \prec 0 \\ \begin{bmatrix} M & -Y \\ -Y^\top & P \end{bmatrix} \succ 0 \end{array} \right. , \tag{5.41}$$

Once matrix  $Y$  is found, the controller is given as  $K = YP^{-1}$ .

## 5.2.2 State observer

The nonlinear controller is here reported:

$$\begin{cases} \alpha = \frac{A_d \zeta - B_d \bar{v}_{in} - \lambda \tilde{x} + \zeta^* - kv}{(A_d - A_c)\zeta + (B_c - B_d)\bar{v}_{in}} \\ \dot{v} = v_{DEA} - v_{DEA}^* \end{cases}, \quad (5.42)$$

where  $v = \int \tilde{y} dt$  and  $\tilde{x} = \zeta^* - \zeta$ . It can be noticed that the controller  $\alpha$  depends on the state of the system. Indeed, the goal of such controller is to follow a state trajectory, considering  $C_c - C_d = 0$ , so that

$$\zeta^* = \frac{1}{C_d} v_{DEA}^*. \quad (5.43)$$

To estimate the system state, a state observer is necessary.

Let  $\hat{\zeta}$  be the state observed according to the following dynamic system

$$\begin{aligned} \dot{\hat{\zeta}} = & -A_d \hat{\zeta} + B_d \bar{v}_{in} + \left( (A_d - A_c) \hat{\zeta} + (B_c - B_d) \bar{v}_{in} \right) \alpha + \\ & + \left( L - A_d + (A_d - A_c) \alpha \right) \left( \frac{v_{DEA}}{C_d + (C_c - C_d) \alpha} - \hat{\zeta} \right), \end{aligned} \quad (5.44)$$

where  $L > 0$  is a free design parameter which allows to tune the convergence speed of the observer. In fact, the convergence and stability of the observer is proved by considering the derivative of the error  $e = \zeta - \hat{\zeta}$ , i.e.,

$$\begin{aligned} \dot{e} = \dot{\zeta} - \dot{\hat{\zeta}} = & -A_d \zeta + B_d \bar{v}_{in} + \left( (A_d - A_c) \zeta + (B_c - B_d) \bar{v}_{in} \right) \alpha + \\ & - \left( -A_d \hat{\zeta} + B_d \bar{v}_{in} + \left( (A_d - A_c) \hat{\zeta} + (B_c - B_d) \bar{v}_{in} \right) \alpha + \right. \\ & \left. + \left( L - A_d + (A_d - A_c) \alpha \right) \left( \frac{v_{DEA}}{C_d + (C_c - C_d) \alpha} - \hat{\zeta} \right) \right) = \\ = & -A_d \zeta + B_d \bar{v}_{in} + \left( (A_d - A_c) \zeta + (B_c - B_d) \bar{v}_{in} \right) \alpha + A_d \hat{\zeta} - B_d \bar{v}_{in} + \\ & - \left( (A_d - A_c) \hat{\zeta} + (B_c - B_d) \bar{v}_{in} \right) \alpha + \\ & - \left( L - A_d + (A_d - A_c) \alpha \right) \left( \frac{v_{DEA}}{C_d + (C_c - C_d) \alpha} - \hat{\zeta} \right) \\ = & -A_d e + (A_d - A_c) e \alpha - \left( L - A_d + (A_d - A_c) \alpha \right) e = \\ = & -A_d e + (A_d - A_c) e \alpha - L e + A_d e - (A_d - A_c) e \alpha = \\ = & -L e, \end{aligned} \quad (5.45)$$

which asymptotically converges to zero as long as  $L > 0$ .

## 5.3 Voltage controllers validation in simulation

This section will present a validation in simulation of the two voltage controllers, (5.8) and (5.23). The simulations were carried out in MATLAB/Simulink environment.

### 5.3.1 Linear voltage control - Validation in simulation

The block diagram of the closed-loop system is shown in Fig. 5.4.

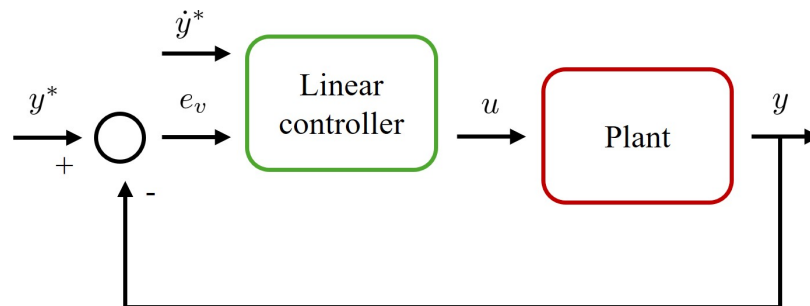


Figure 5.4: Block diagram of the closed-loop system when the linear controller is used.

The block "Linear controller" consists of the combination of controller (5.8) and an anti-windup clamping strategy, aimed to avoid value of the control action  $u$  bigger than 1. The performance of the closed-loop system was analyzed using both the linear model (5.2) and the average model (4.65) as the plant. Several simulations were conducted in the MATLAB environment, and the results are shown in Fig. 5.5. The system's response to different desired trajectories, varying in amplitude and frequency, was examined. The control parameters are the ones expressed by (5.18).

The results indicate that the output voltage  $v_{DEA}$  accurately follows small-amplitude trajectories, specifically  $\pm 100$  V and  $\pm 500$  V around the equilibrium point  $v_{DEA} = 1500$  V at frequencies of 1, 10, and 40 Hz. However, for larger amplitude trajectories and higher frequencies, the output voltage fails to follow the desired trajectory, particularly when the average model is used as the plant. This discrepancy occurs because the controller (5.8) is based on the small-signal model (5.2), which is not adequate for larger signals. Figure 5.6 shows the correlated errors in time, where it can be noticed that for small-amplitude trajectories the error stays below the 1%.

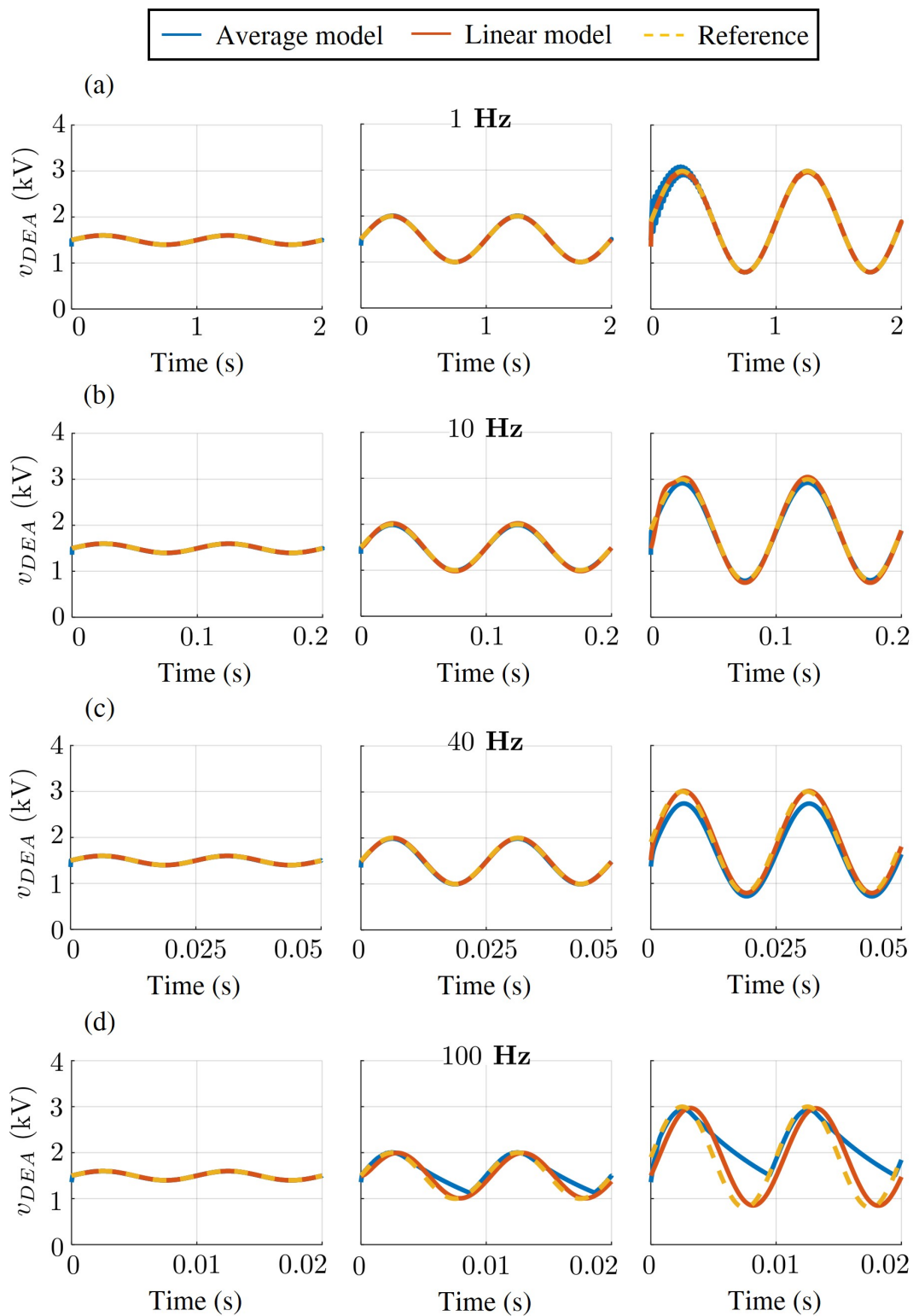


Figure 5.5: Validation in simulation of the linear voltage controller, considering both the linear and the average model as the plant of the closed-loop system. Trajectory with  $\pm 100 - \pm 500$  V amplitude around the equilibrium point and large-amplitude trajectory are considered at (a) 1 Hz, (b) 10 Hz, (c) 40 Hz, and (d) 100 Hz.

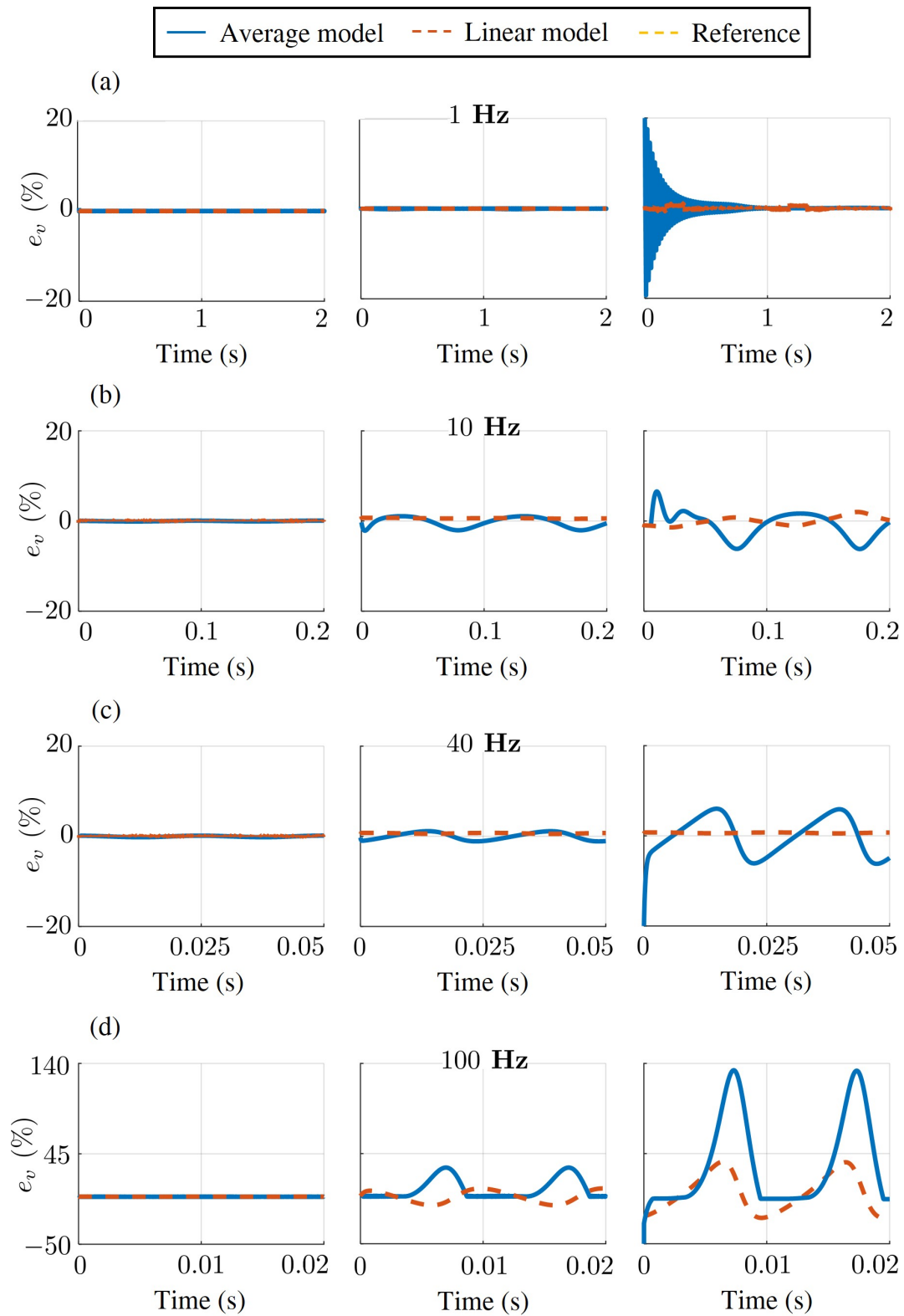


Figure 5.6: Percentage errors of the validation in simulation. (a) 1 Hz; (b) 10 Hz; (c) 40 Hz; (d) 100 Hz.

### 5.3.2 Nonlinear voltage control - Validation in simulation

Figure 5.7 shows the block diagram of the closed-loop system, considering the nonlinear controller (5.23) and the switching model (4.59) as plant. First the feasibility of

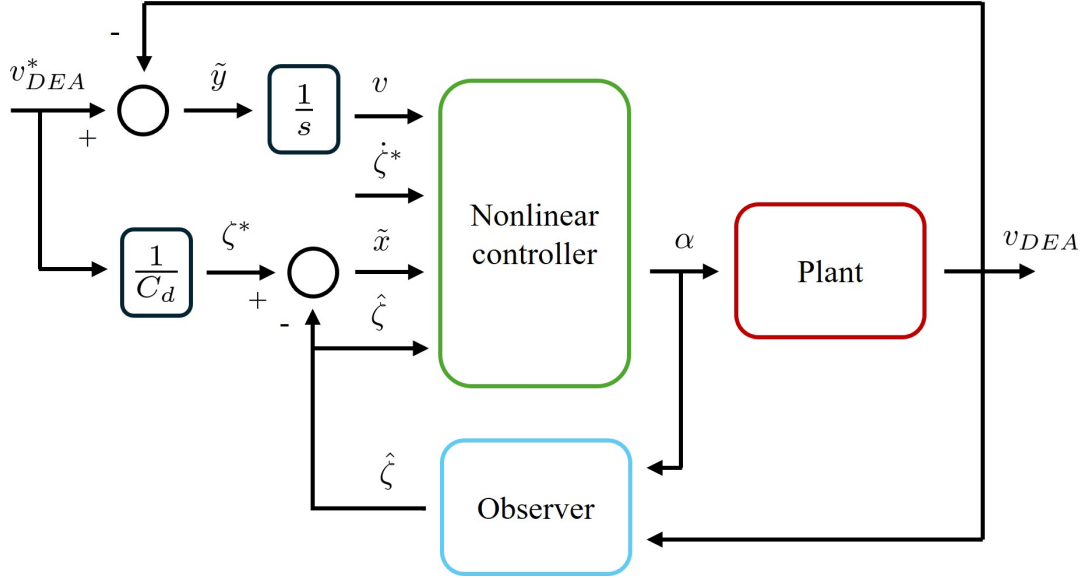


Figure 5.7: Block diagram of the closed-loop system when the nonlinear controller is used.

the LMI problem in (5.41) was examined. The filter parameters are the followings:

$$A_\infty = \left| \underline{\gamma} \frac{A_d}{C_d} \right| \quad (5.46)$$

$$A_b = \frac{0.01}{\sqrt{1 + \frac{\omega_b^2}{A_d^2}}} \beta,$$

with  $\beta$  as the error percentage. The analysis shows that with a percentage error  $\beta \leq 2$  the minimum cutting frequency that makes the LMI problem feasible is  $\omega_{b,Hz} = 40$  Hz, while for a percentage error  $\beta \leq 5$ , the cutting frequency is  $\omega_{b,Hz} = 70$  Hz. Considering (5.34), the transfer function from  $\delta(y^*)$  and  $v$  is:

$$G_v(s) = C_m(sI - A_m)^{-1}B_m, \quad (5.47)$$

with  $C_m = [1 \ 0]$ ,  $A_m = A(\underline{\gamma}) - B_1(\underline{\gamma})K$ , and  $B_m = B_2(\underline{\gamma})$ . Thus, the transfer function from  $\delta(y^*)$  and  $\tilde{y} = v_{DEA}^* - v_{DEA} = \dot{v}$  is:

$$G_{\tilde{y}}(s) = sG_v(s). \quad (5.48)$$

Figure 5.8 shows the bode magnitude diagrams of  $G_{\tilde{y}}(s)$  considered for  $\underline{\gamma} = \underline{\gamma}$  at different  $\omega_{b,Hz}$  and  $\beta$ , compared to the bode diagram of the upper bound  $\overline{W}(s)$ ,

shown in Fig. 5.8. In particular, the following specifications were chosen:

$$\begin{aligned} \text{Fig. 5.8 (a): } & \begin{cases} \omega_{b,H_z} = 40\text{Hz} \\ \beta = 1 \end{cases}, \text{ Fig. 5.8 (b): } & \begin{cases} \omega_{b,H_z} = 40\text{Hz} \\ \beta = 2 \end{cases}, \\ \text{Fig. 5.8 (c): } & \begin{cases} \omega_{b,H_z} = 50\text{Hz} \\ \beta = 1 \end{cases}. \end{aligned} \quad (5.49)$$

The magnitude of  $G_{\tilde{y}(s)}$  stays in each cases bounded and the LMI problems are feasible, given the following control gain:

$$(a) \quad K = YP^{-1} = [k \ \lambda] = [1.9 \times 10^4 \ 8.8 \times 10^3]$$

$$(b) \quad K = YP^{-1} = [k \ \lambda] = [3 \times 10^4 \ 2.7 \times 10^3]$$

$$(c) \quad K = YP^{-1} = [k \ \lambda] = [1.1 \times 10^5 \ 3.2 \times 10^4].$$

It is important to notice that not every combination of  $\omega_{b,H_z}$  and  $\beta$  give in result a feasible LMI problem. Indeed, if  $\omega_{H_z} = 60$  Hz and  $\beta = 1$  are to be chosen, the LMI problem would not be feasible and, in fact, the control gain would be  $K = YP^{-1} = [k \ \lambda] = [-2 \times 10^5 \ -4.1 \times 10^4]$ . To render the LMI feasible for such frequency, or greater than this, the error margin needs to be increased.

In simulation, the performance of the closed-loop system utilizing the nonlinear controller (5.41) with the switching model (4.59) as the plant was compared to the performance obtained using the linear controller (5.2) applied to the average model (4.65). This comparison was conducted for both small-amplitude and large-amplitude trajectories. The nonlinear controller parameters for this campaign are:

$$\text{I. Nonlinear controller: } \omega_{b,H_z} = 40 \text{ Hz, } \beta = 2 \rightarrow K = YP^{-1} = [k \ \lambda] = [1.6 \times 10^4 \ 9 \times 10^3]$$

$$\text{II. Observer: } L = 100.$$

To properly compare nonlinear and linear controller, the linear controller parameter where chosen as in (5.18). For this simulation campaign the nonlinear controller was applied to the switching model, while the linear controller was applied to the average model. Figure 5.9 shows the results of the validation. The quantities of interest are the output voltage  $v_{DEA}$  in both cases, the voltage error  $e_v = v_{DEA}^* - v_{DEA}$ , the system state  $x$ , and the observer output  $\hat{x}$ . Trajectories at 40 Hz for small and large-amplitude were chosen. The results show that for small-amplitude trajectories, both controllers work very well, ensuring an error  $e_v < 1\%$ . For large-amplitude trajectories, the benefits of the nonlinear controller are evident. Indeed, the output  $v_{DEA}$  can follow the desired trajectory with an error  $e_v < 2\%$ , whereas the system under the linear controller fails to pursue the trajectory and the voltage error exceeds the 1%.



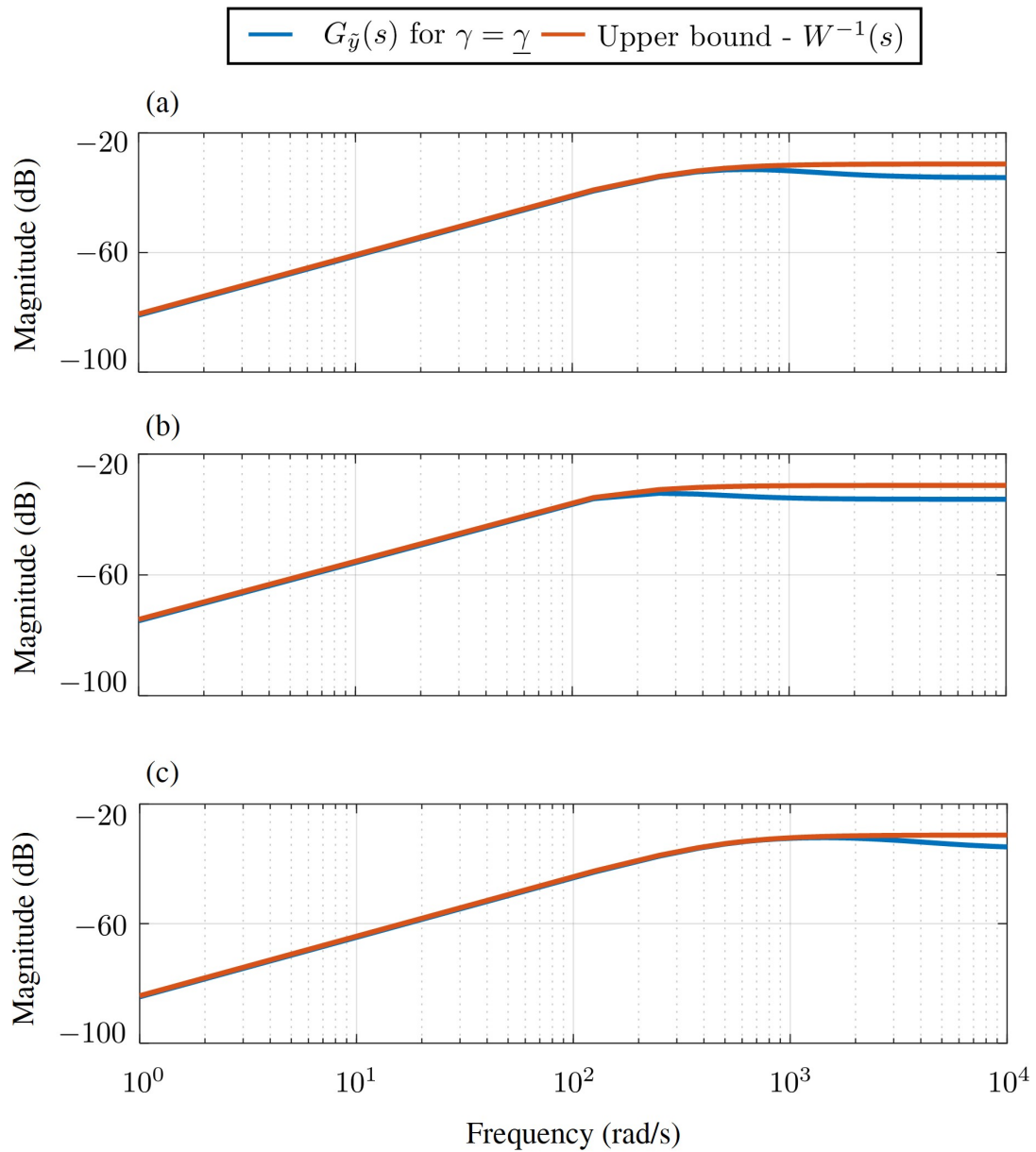


Figure 5.8: Bode magnitude diagrams of  $G_{\bar{y}}(s)$  and  $W(s)$  for (a)  $\omega_{b,Hz} = 40$  Hz,  $\beta = 1$ ; (b)  $\omega_{b,Hz} = 40$  Hz,  $\beta = 2$ ; (c)  $\omega_{b,Hz} = 50$  Hz,  $\beta = 1$ .

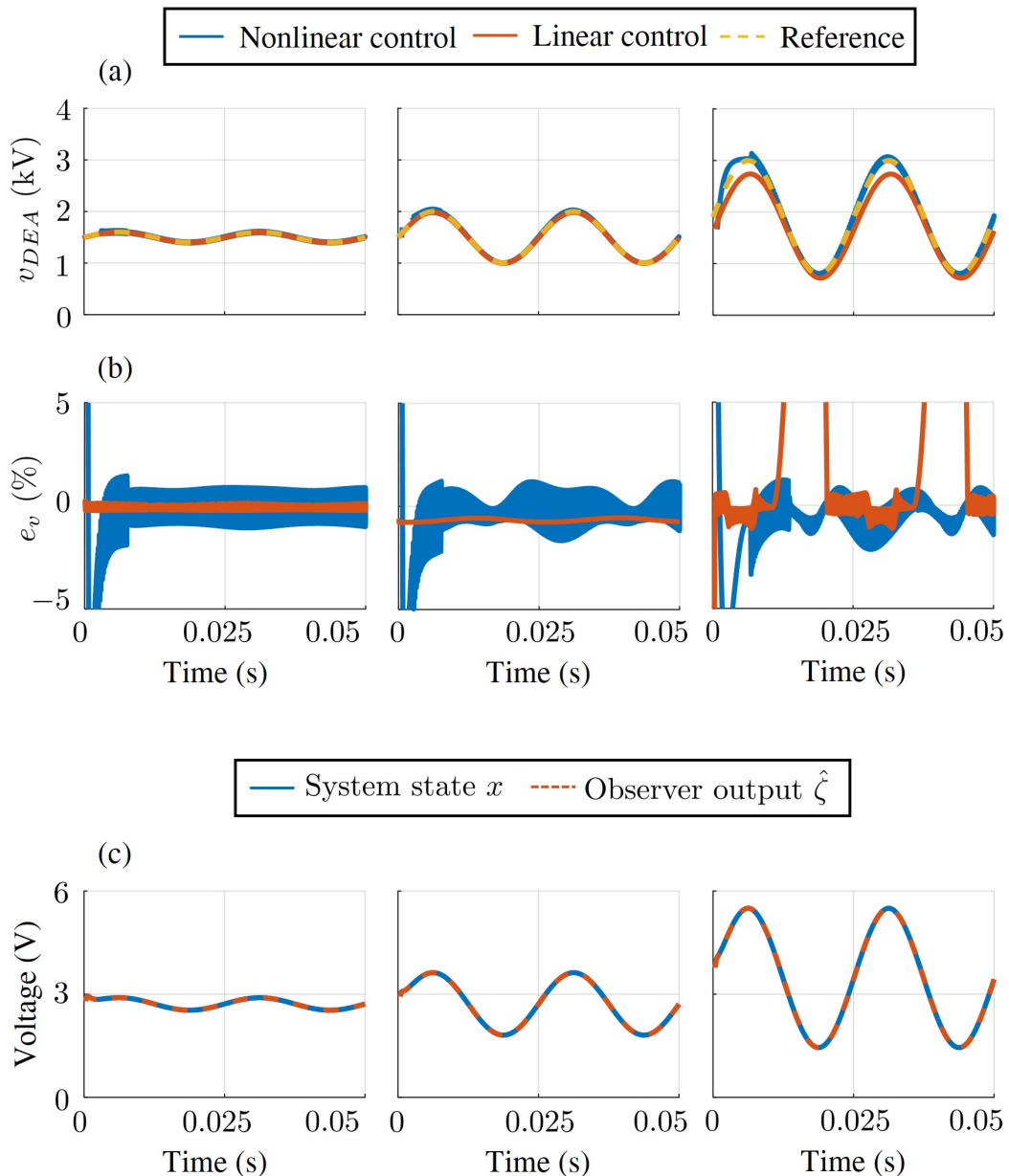


Figure 5.9: Validation in simulation, considering both linear and nonlinear controller for the switching model for small- and large-amplitude trajectories at 40 Hz. (a) Output of the closed-loop systems; (b) Voltage error; (c) System state and observer output.

## 5.4 Voltage controllers experimental validation

In this section an experimental campaign will be carried out with the goal of validate experimentally the linear and nonlinear voltage controllers. The controllers will be implemented on an STM32 NUCLEO F446RE board, which generated the PWM driving signals for the circuit at a frequency of 15 kHz. The used setup is shown in Fig. 4.19.

### 5.4.1 Linear voltage control - Experimental validation

The first experimental validation aimed to assess the performance of the linear voltage controller in tracking a specified reference voltage. The voltage signal to be tracked was a sinusoidal wave ranging from 1400 V to 1600 V at increasing frequencies. Figure 5.10 compares the voltage reference, the output of the closed-loop system, and the output of the open-loop system. The output signals are measured via a high-voltage voltage divider. It is evident that the controller significantly improves the circuit performance, allowing it to accurately track reference signals up to 60 Hz, while unavoidable model inaccuracies reduce the tracking precision at higher frequencies. As a further quantitative comparison, Fig. 5.10 shows the voltage error offset (upper part), calculated as follows

$$e_{off} = |\bar{y}^* - \bar{y}|, \quad (5.50)$$

with  $\bar{y}^*$  and  $\bar{y}$  the mean value of the trajectory and the output signal, respectively. The figure shows also the Root Mean Square (RMS) value of its offset-free amplitude (lower part) for different frequencies, calculated as

$$RMS = \sqrt{\frac{1}{N} \sum_{i=1}^N |e_v - \bar{e}_v|^2}, \quad (5.51)$$

with  $N$  length of the data, and  $\bar{e}_v$  the mean value of the error  $e_v$ . The results confirm the benefits of the closed-loop voltage control architecture.

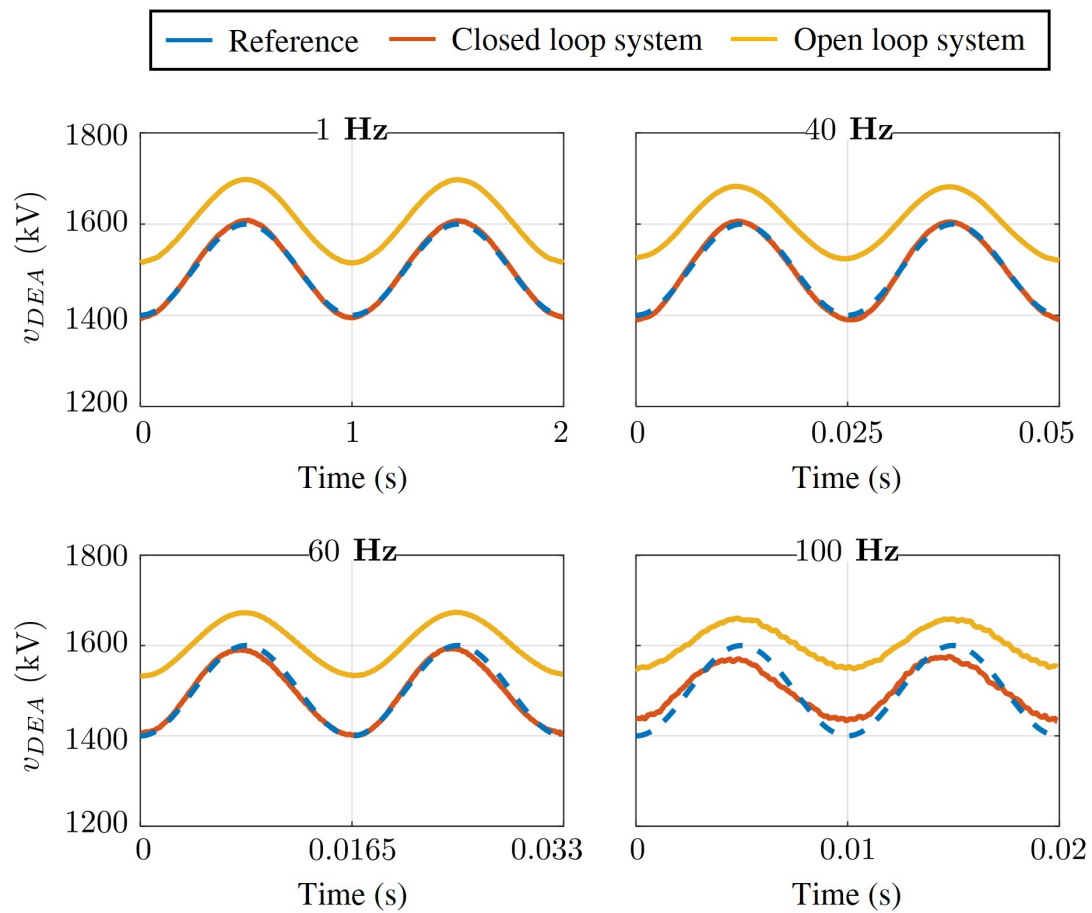


Figure 5.10: Experimental validation of the linear voltage controller for small-amplitude trajectories at different frequencies.

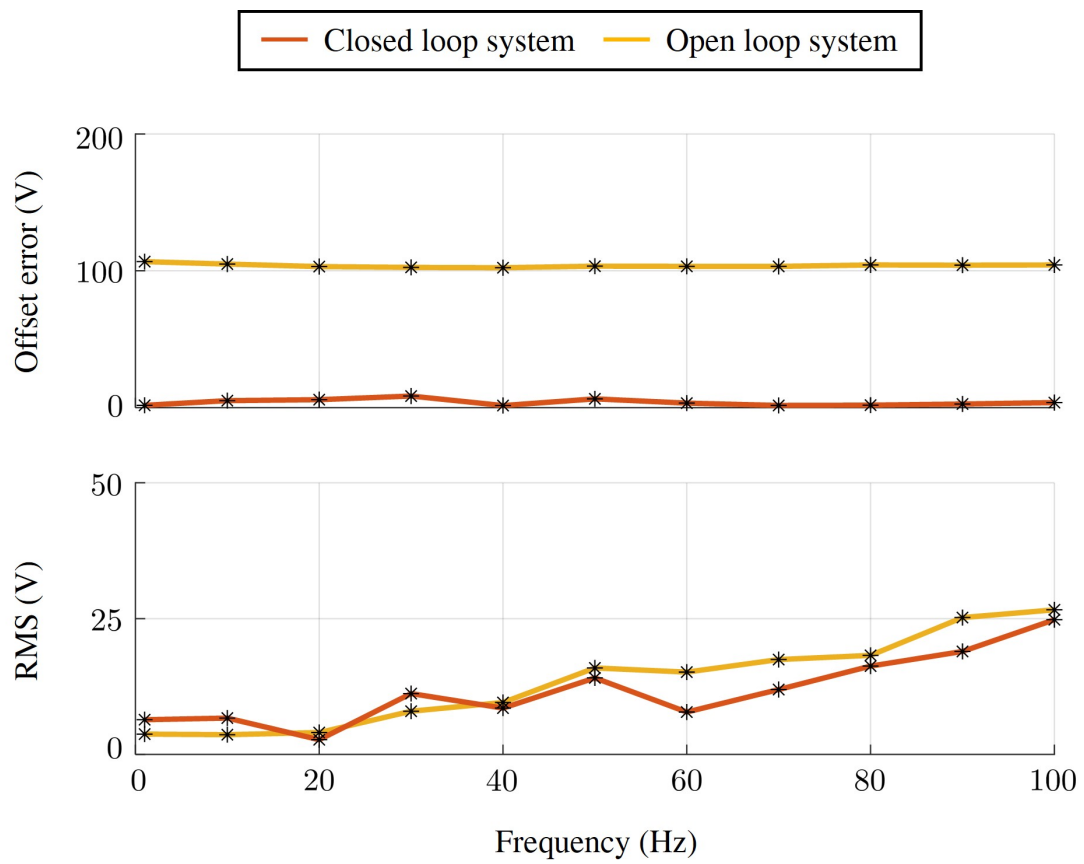


Figure 5.11: Offset and amplitude RMS errors at each frequency.

### 5.4.2 Nonlinear voltage control - Experimental validation

A broad experimental campaign was carried out to validate the closed-loop performance when the nonlinear controller is applied. The goal is to demonstrate that the bandwidth of the circuit in closed-loop is higher than the bandwidth obtained in open-loop (40 Hz), by maintaining an error margin between 2 – 5%. The desired trajectory was a sinusoidal wave at different amplitude ranges and frequencies. Figures 5.12 and 5.13 show the experimental results. The output voltage  $v_{DEA}$  has been compared to the reference and only in 5.12 (a) to the output voltage obtained by closed-loop controlled via the linear controller (5.8). For this analysis, the nonlinear controller specifications were chosen as follows:

$$\begin{cases} \omega_{b,Hz} & = 40 \text{ Hz} \\ \beta & = 2 \end{cases}, \quad (5.52)$$

while the specifications of the linear controller were set as in (5.18). At frequencies greater than 40 Hz, considering the feasibility of the LMI optimization problem exposed above, the chosen controller specifications are:

$$\begin{cases} \omega_{b,Hz} & = 70 \text{ Hz} \\ \beta & = 5 \end{cases}. \quad (5.53)$$

As a further quantitative comparison, an analysis only for large-amplitude signals was conducted. Figure 5.14 shows the voltage error offset (upper part), calculated as follows

$$e_{off} = |\bar{v}_{DEA}^* - \bar{v}_{DEA}|, \quad (5.54)$$

with  $\bar{v}_{DEA}^*$  and  $\bar{v}_{DEA}$  the mean value of the trajectory and the output signal, respectively. The figure shows also the Root Mean Square (RMS) value of its offset-free amplitude (lower part) for different frequencies, calculated as

$$RMS = \sqrt{\frac{1}{N} \sum_{i=1}^N |e_v - \bar{e}_v|^2}, \quad (5.55)$$

with  $N$  length of the data, and  $\bar{e}_v$  the mean value of the error  $e_v$ . The results confirm that the closed-loop controlled by the nonlinear voltage controller is able to follow sinusoidal small-amplitude trajectories with an error below the 5% up to 120 Hz and large-amplitude with an error below the 4% up to 80 Hz, making evident the benefit of this controller over the linear controller presented previously.

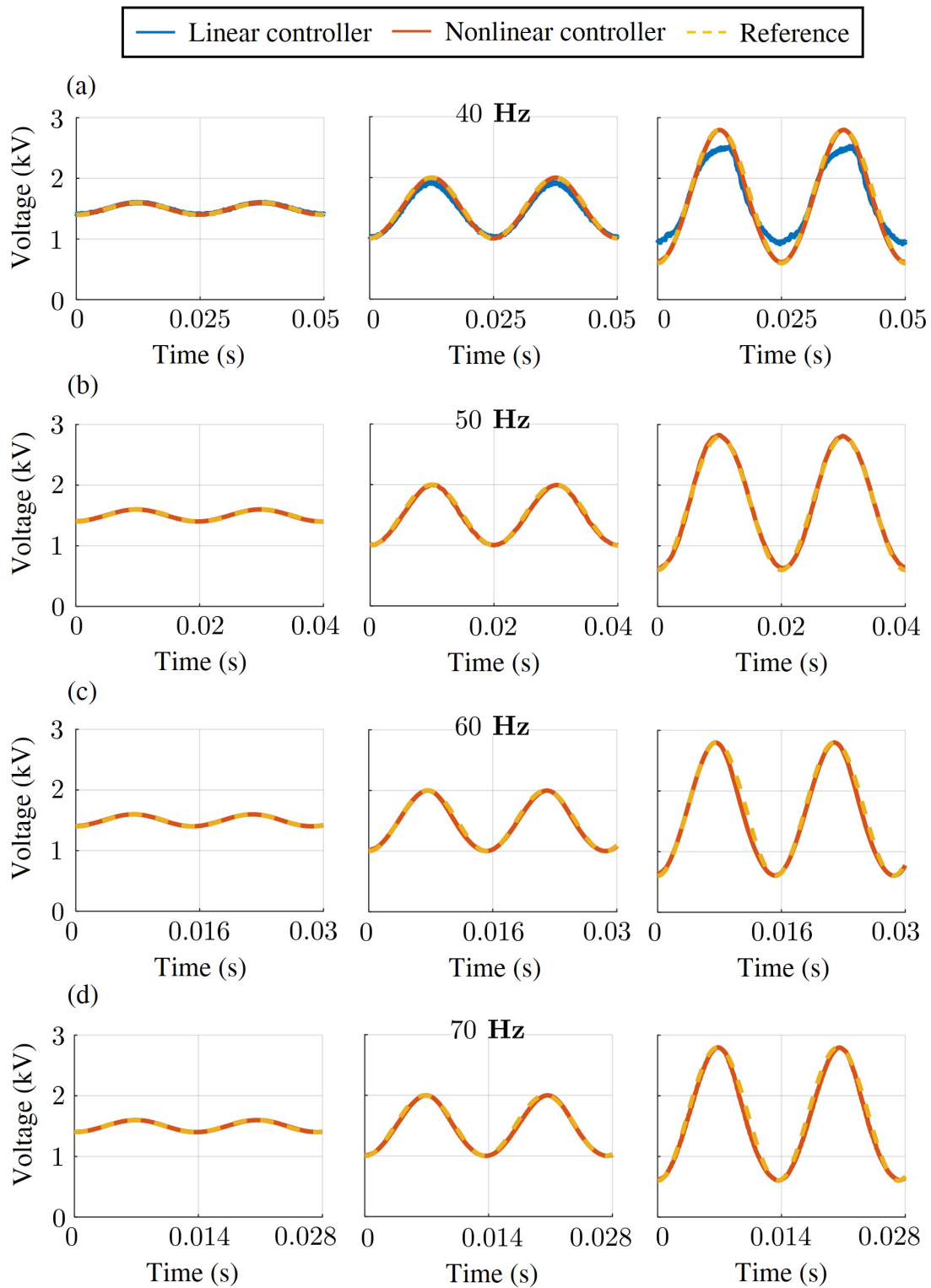


Figure 5.12: Experimental validation of the voltage controller for small- and large-amplitude trajectories at different frequencies: (a) 40 Hz; (b) 50 Hz; (c) 60 Hz; (d) 70 Hz.

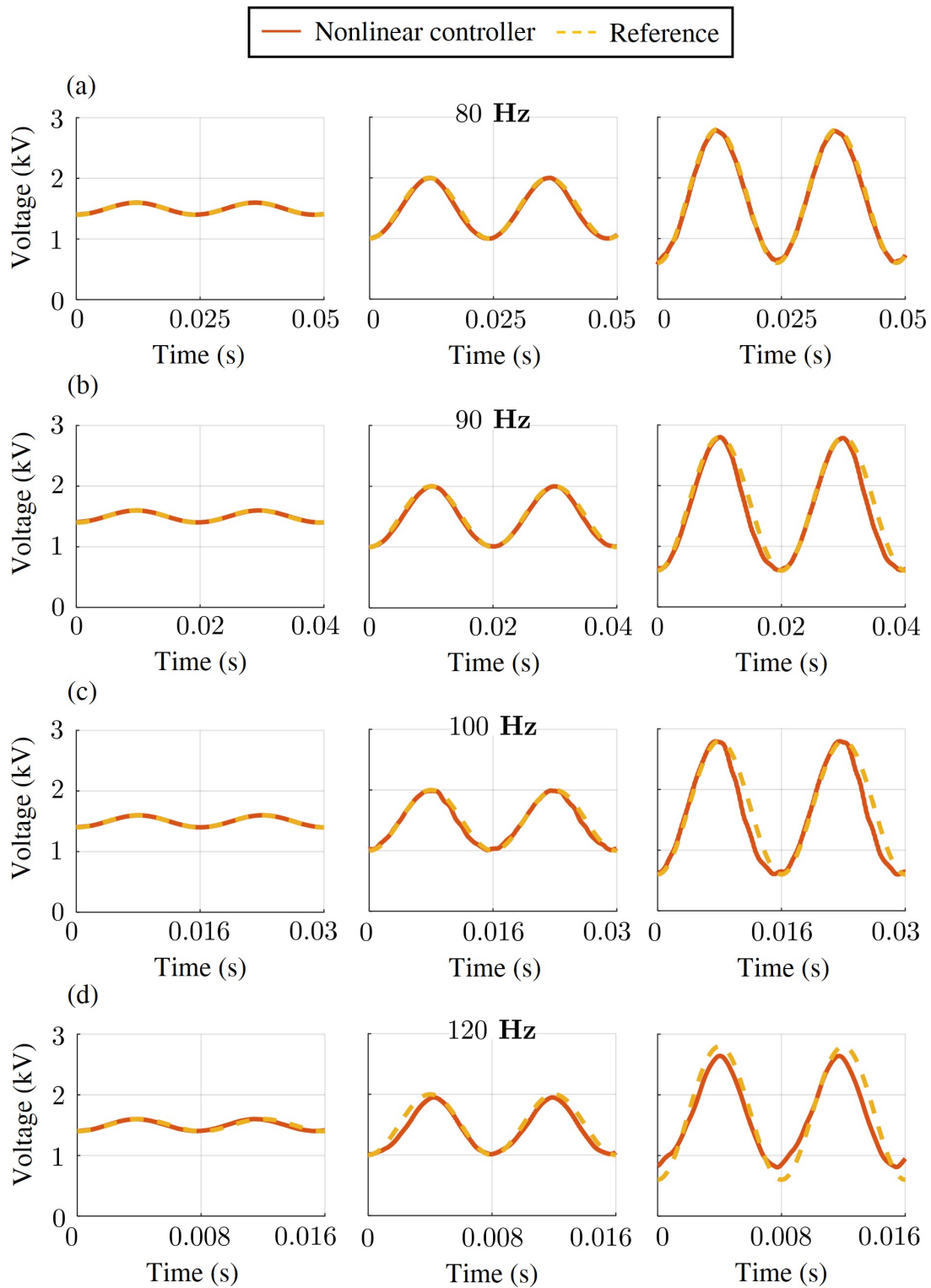


Figure 5.13: Experimental validation of the voltage controller for small- and large-amplitude trajectories at different frequencies: (a) 80 Hz; (b) 90 Hz; (c) 100 Hz; (d) 120 Hz.



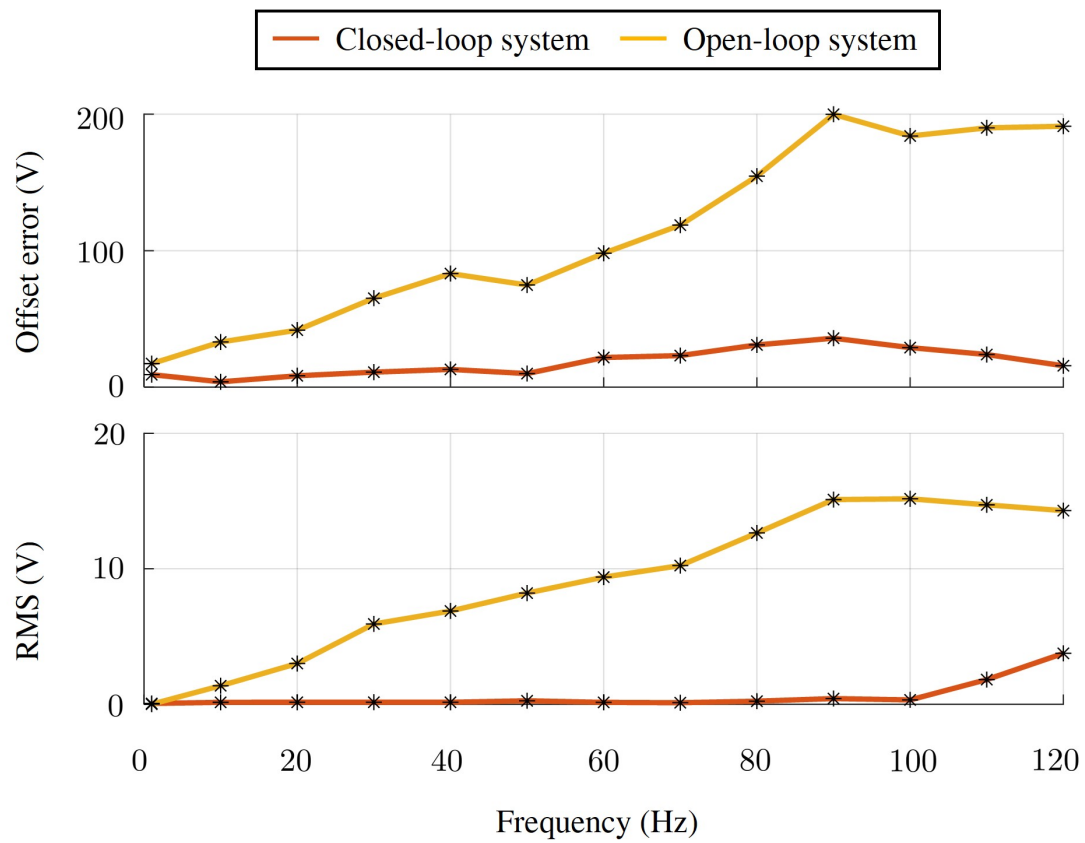


Figure 5.14: Offset and amplitude RMS errors at each frequency. In red and yellow the performance of the closed- and open-loop, respectively.

# Chapter 6

## Applied case of study: DEAs position control

In this chapter the linear voltage control (5.8) will be applied to a specific case of study: DEA position control. Small and accurate actuation displacement of the actuator are required in many application, such as in microfluidics, i.e., valve application, where only few millimeters of the DEA's stroke are necessary to open or close the valve, or optical application where DEAs can adjust the focus of lenses.

The primary focus is on the actuator's displacement. To achieve fine adjustment, the control strategy integrates a DEA motion controller, as developed in [4], with the linear voltage controller (5.8). Results will demonstrate that relying solely on position control is insufficient for precise and fine-tuned adjustment of the actuator's displacement without also controlling the voltage applied to the DEA. The performance of the closed-loop system, where the DEA is driven by a HV circuit, will be compared to that of a system using a commercial voltage amplifier, specifically an UltraVolt. It will be shown that the HV circuit's performance in terms of precision of the delivered output voltage within a mechanical frequency range of  $[0 - 4]$  Hz is comparable to that of the UltraVolt amplifier. The results are reported in the conference paper [3].

### 6.1 Nested control: Linear voltage and DEA's position controllers

The proposed controller (5.23) will be integrated into a DEA motion control loop, whose design is based on our previous results in [4]. The latter control strategy will aim to control the DEA position  $y_p$  so to track a desired motion trajectory  $y_p^*$ . It consists of a low-pass filtered PID controller combined with a square root term, to compensate for the nonlinear relationship between DEA displacement and the applied voltage, in parallel to a feed-forward term. The block diagram of the closed-loop system is shown in Fig. 6.1 . Initially, an identification process was conducted to establish a mathematical model of the DEA, using the applied voltage as the input and the resulting displacement as the output. The DE illustrated in Fig. 4.19 (dimensions:  $30 \text{ mm} \times 30 \text{ mm} \times 50 \mu\text{m}$ ) was the subject of the identification process.

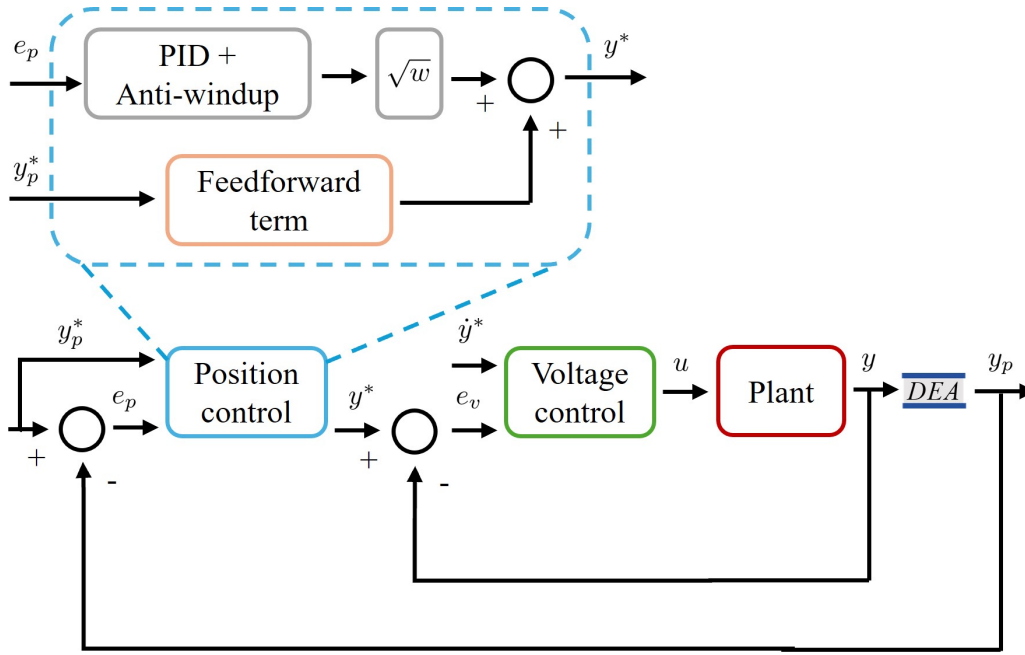


Figure 6.1: Block diagram of the cascade of DEA outer position controller and HV circuit inner voltage controller.

Pulse wave high voltage signal at 0.2 Hz was applied using a commercial voltage amplifier, specifically an UltraVolt, and the DE's displacement was assessed using the laser sensor optoNCDT 1607. Data collection was conducted via LabVIEW and subsequently analyzed in MATLAB. The mathematical model for the DE was identified using the System Identification MATLAB Toolbox and it results as follows:

$$G_{DEA}(s) = \frac{Y_p(s)}{Y^2(s)} = \frac{b_0}{s^2 + a_1s + a_0}, \quad (6.1)$$

with  $Y^2(s)$ ,  $Y_p(s)$  Laplace transformation of the squared applied voltage  $y^2$  and the DEA position  $y_p$ , respectively. The coefficients are:

$$b_0 = 4.7 \times 10^{-4}, \quad a_1 = 7.554, \quad a_0 = 1402. \quad (6.2)$$

The resulting second-order model demonstrated a FIT of 87.55% between the observed and predicted displacements. Figure 6.2 presents the results of this identification.

The PID controller as the following structure:

$$PID(s) = K_p + \frac{K_i}{s} + \frac{K_d s}{\tau_d s + 1}, \quad (6.3)$$

with  $K_p$  proportional gain,  $K_i$  integral gain,  $K_d$  derivative gain, and  $\tau_d$  time constant of the low-pass filter. Its parameter were calculated as:

$$\begin{cases} K_p = \left(a_1 - \frac{a_0 \tau^*}{2}\right) \frac{1}{2b_0 \delta^{*2} \tau^*} \\ K_i = \frac{a_0}{2b_0 \delta^{*2} \tau^*} \\ K_d = \left(1 - \frac{a_1 \tau^*}{2} + \frac{a_0 \tau^{*2}}{4}\right) \frac{1}{2b_0 \delta^{*2} \tau^*} \\ \tau_d = \frac{\tau^*}{2} \end{cases}, \quad (6.4)$$

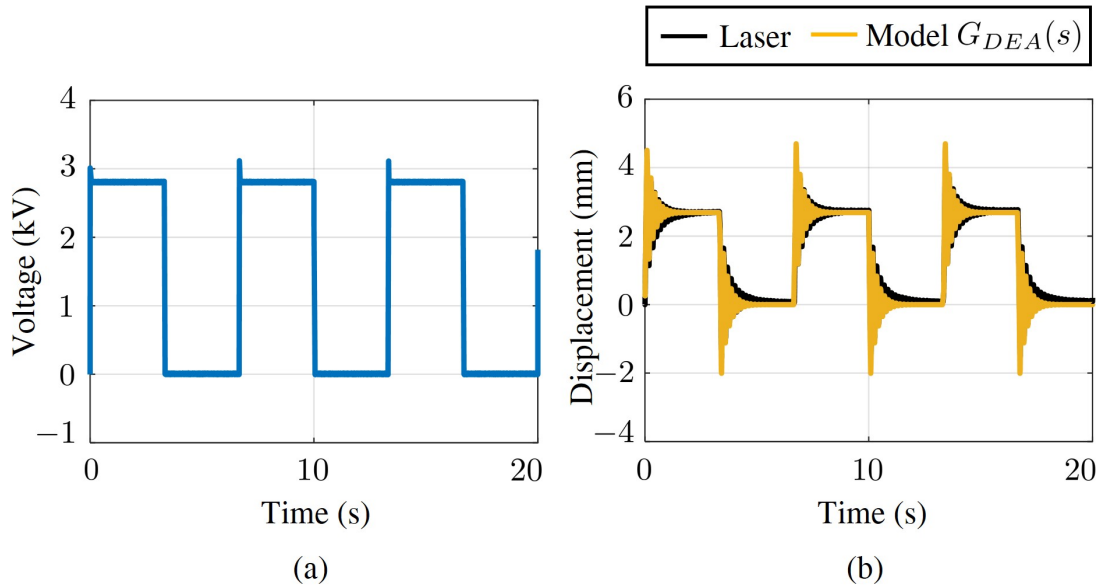


Figure 6.2: DEA model identification. (a) High voltage signal, model input; (b) Comparison between laser measurement and the model output.

with  $\tau^* = 0.4$  s and  $\delta^* = 0.7$ . An anti-windup strategy is used so that the output of  $PID(s)$  is bounded between  $y_{min}^{*2} = 600^2$  and  $y_{max}^{*2} = 3000^2$ . The feed-forward term is the following:

$$G_{DEA}^{-1}(s) = \frac{s^2 + a_1 s + a_0}{b_0}. \quad (6.5)$$

Because both static and dynamic behaviors of DEAs displacement are influenced by the square of the applied voltage, a square root term is added in cascade to the PID. By doing so, the effect of this nonlinearity is canceled by an inverse compensation in the control law.

Finally, the output  $y^*$  of the position controller represents the desired high voltage that the circuit needs to generate. Thus,  $y^*$  is the desired trajectory for the voltage controller.

## 6.2 Experimental validation

Experimental validation will be performed by using the setup in Fig. 4.19 in three different scenarios, where the DEA input voltage is regulated as follows:

- I. using the position controller to directly drive the HV circuit, without any voltage control loop;
- II. using the position controller output as the reference voltage for controller (5.8), resulting in the nested control in Fig. 6.1;
- III. using the position controller output as the reference voltage for the UltraVolt supply, which is assumed to behave as an ideal voltage source.

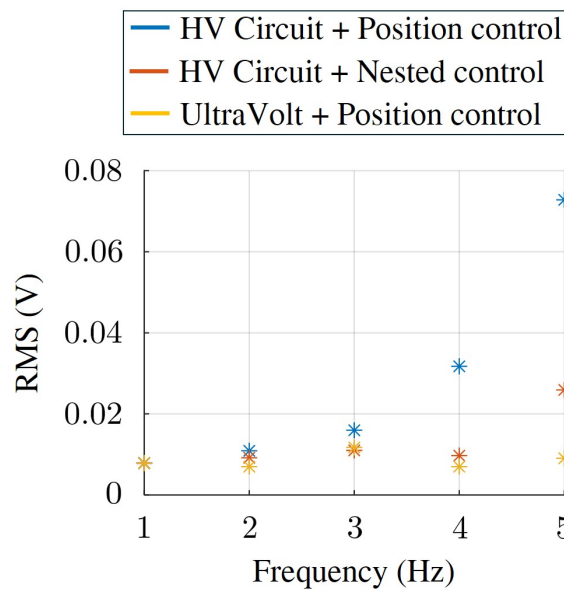


Figure 6.3: RMS values at each frequency.

The reference trajectories,  $y_p^*$ , are sinusoidal signals ranging from 0 mm to 0.2 mm, and frequency between 1 Hz and 5 Hz. The results in Fig. 6.4 show the tracking performance achieved through the nested control strategy compared to relying solely on the position controller. Figure 6.3 shows the RMS values of each experiment case at each frequency. When the position controller directly drives the HV circuit, its tracking performance begins to decline markedly when the reference frequency surpasses 3 Hz. In contrast, the nested control architecture maintains performance levels that are closely aligned with those achieved using the Ultravolt amplifier. Furthermore, the position error remains consistently below 0.07 mm when utilizing the nested control. This is in stark contrast to the scenario where only the position controller is employed, which results in a position error as significant as the reference amplitude at a frequency of 5 Hz. This difference highlights the inadequacy of the position controller alone in handling higher reference frequencies. The nested control method effectively decouples the design considerations of the position and voltage controllers. This decoupling allows the HV circuit to function with a behavior akin to a constant gain system, thereby simplifying the control strategy and enhancing overall performance. As a result, the proposed control architecture not only matches the performance of high-end HV amplifiers but does so with significantly reduced complexity and cost. In light of this result, the HV circuit, when operated under the proposed nested control approach, emerges as a highly cost-effective and efficient solution for driving and controlling DEAs. This approach obviates the need for bulky and expensive commercial HV amplifiers, offering a streamlined and economically viable alternative without compromising on performance.

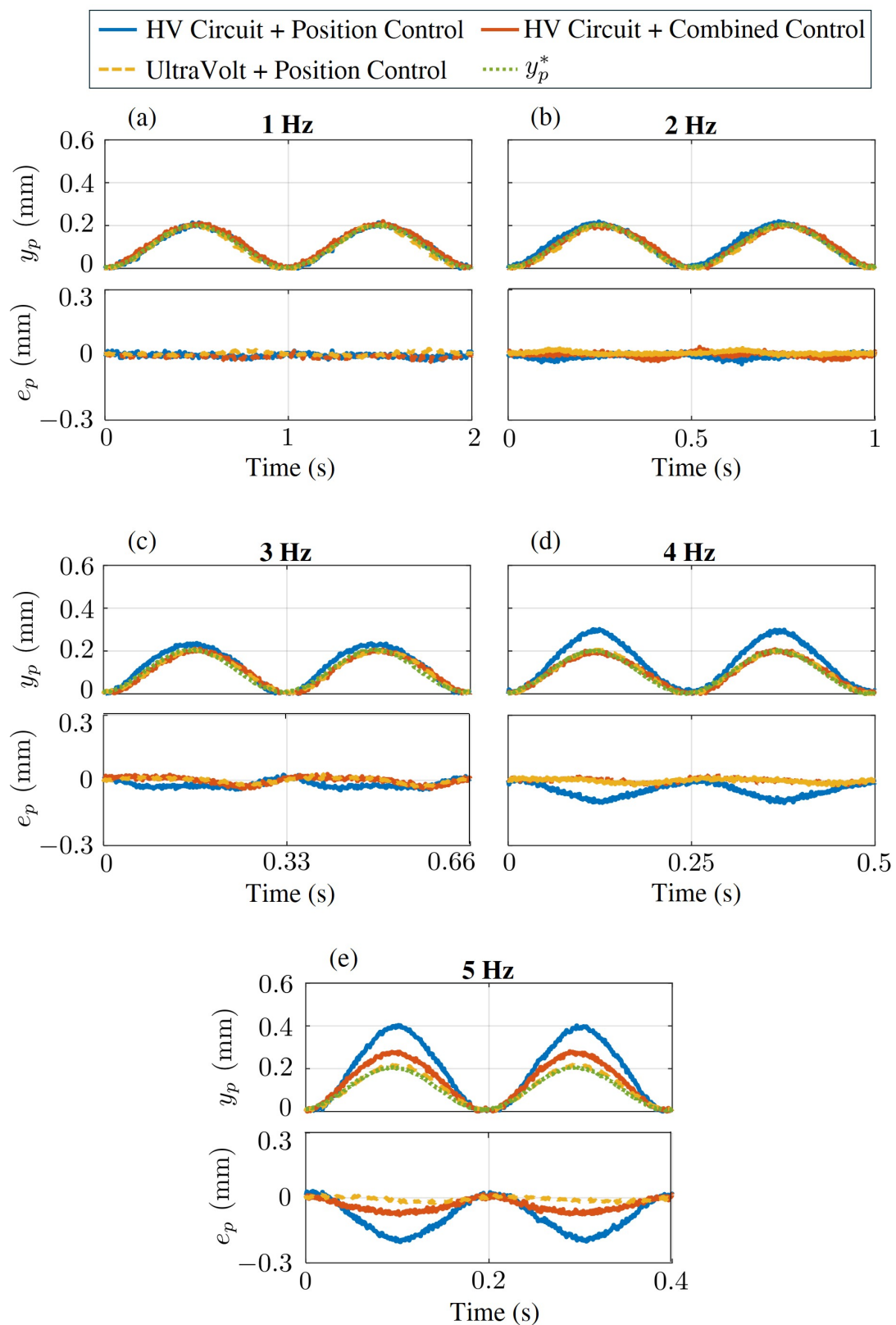


Figure 6.4: Experimental comparison of different control architectures. A desired trajectory of 0.2 mm was chosen at (a) 1 Hz, (b) 2 Hz, (c) 3 Hz, (d) 4 Hz, and (e) 5 Hz.

# Chapter 7

## Conclusions

This thesis has addressed the problem of developing and control a High Voltage (HV) driving circuit for Dielectric Elastomer Actuators (DEAs). In order to achieve this goal, the thesis has been organized in four main parts, which deal in details with the design, modeling, voltage control, and voltage-position control, respectively.

In the first part, the design of the circuit was presented. The HV electronic is characterized by two stages, namely the charging and the discharging stages. The charging stage consists of a resonant converter combined to a voltage doubler and rectifier circuit and it exploits a three-coil transformer with a turn ration between primary and secondary side of 100. This simple concept allowed to generate high voltage (up to 3000 V) from a low input voltage (up to 6 V). The discharging stage involves an active discharging path that allows the load to discharge more efficiently. Consequently, the discharging time decreases significantly, enabling operation at a high frequency. Moreover, a microcontroller interface is deployed to digitally control via two complementary PWM signals. The design used a relative low number of components to maintain small dimensions (130 mm  $\times$  50 mm), a low cost (20\$), and minimal weight (48 g). Consequently, the circuit can be easily integrated into various applications where a compact driving circuit is required.

In the second part, a mathematical model for the circuit was presented. Initially, two separate LTI state-space models were developed for the charging and discharging stages, considering equivalent models of the dynamic components, the stray and ohmic losses of the transformer, and the DEA as time-varying capacitive load. The two models were combined into one model, named switching model, to take into account the switching behavior of the circuit between the charging and discharging phases. The model was able to effectively predict the output voltage of the circuit for given input voltage. Validation campaigns, both in simulation and through experiments, demonstrated a high agreement between the measured and predicted output voltage signals for various input voltage signals across different frequencies and amplitudes. The *FIT* of the model ranged from 79.16% to 94.54%, depending on the frequency and waveform of the input signal. From the experimental validation, it was observed that the bandwidth of the circuit in open-loop was around 40 Hz. Subsequently, an average model was presented to facilitate the development of simpler linear and nonlinear control strategies.

In the third part two voltage control algorithms were presented. The first one

was a linear controller based on the linear model derived from the average model. The control law was derived by inverting the system linear dynamic and imposing a new one, designed to satisfy the control requirements, i.e., the tracking of small-amplitude voltage trajectories up to 100 Hz maintaining the voltage error below 1%. The second control strategy was based on the average model represented as a LPV system. Thus, the problem of designing a controller for the complex nonlinear system was converted into the design of a state feedback control for the LPV system. This design was effectively addressed via a LMI optimization techniques. This approach enabled the design of a robust control law that was easy to implement without explicitly canceling the system nonlinearities. Since the nonlinear controller required measurements of the system state, an observer was developed. The nonlinear voltage controller was validated in simulation and via an experimental campaign. Compared to the linear controller, the nonlinear controller allowed the circuit's output voltage to follow both small- and large-amplitude trajectories up to 80 Hz with a voltage error below 4%. Thus, the voltage controller enhanced the performance of closed-loop system by increasing also its bandwidth.

The fourth part of the thesis focused on the combination of the linear voltage controller with a DEA position controller. The performance of DEAs is influenced by the applied voltage. Therefore, to achieve precise actuator positioning, it is essential to integrate a position controller for the DEA with a voltage controller for the driving electronics. The combination of these controllers was also experimentally validated. During the campaign, the actuator was first driven by the proposed HV circuit controlled by the combined controller and then by a commercial voltage amplifier, the UltraVolt, subjected only to the position controller since its bandwidth could be considered infinite compared to that of the HV circuit. The results showed that within the range of mechanical frequency before the resonance frequency of the DEA, the HV circuit's performance was comparable to that of the UltraVolt. Indeed, the RMS values obtained from the system driven by the HV circuit are below 0.02 V up to 4 Hz, matching those obtained from the system driven by the UltraVolt.

The results shown in this thesis proved that it is possible to design a small, compact, modular, lightweight, and cheap high voltage electronic to drive DEAs and that by means of model-based control laws, the electronic can be a valid alternative to the commercial, bulky, and expensive voltage amplifiers, for accurately drive a DEA. Nevertheless, there are still a number of open research issues on high voltage circuit design and control. Some possible directions for future research are outlined below.

The key role in the design of the HV circuit is the transformer  $TR$ , which presents an high amplification factor. However, the transformer represents also the bottleneck of the circuit in terms of maximum output voltage and power. Indeed, the circuit is limited to an output of 4500 V and around 2 W. Consequently, the actual circuit cannot drive actuators in applications where the capacitive load is significantly high, such as those using stacked DEs, where capacitance can reach values as high as 50 nF, and required power can be in the order of  $10^1$  W. Additionally, it is not suitable for high-frequency applications, such as acoustic applications. Therefore, optimizing the HV circuit for high-frequency and/or high-power applications is a crucial research



topic that would significantly expand the use of DEAs in various applications. This optimization would enable, for example, the possibility of self-sensing control of DEAs by utilizing the HV circuit as the driving source.

The mathematical model presented in this thesis can be enhanced by incorporating the dielectric resistance of the DEA, which would account for the leakage current of the actuator. This enhancement would enable a more accurate estimation of the discharging time, leading to improved predictions of the output voltage at high frequencies. Additionally, this extended model could be used to develop advanced control strategies designed to track large-amplitude trajectories at high frequencies. Furthermore, the mathematical model developed in this thesis can be utilized to create observers for controlling the output voltage by measuring on the low-voltage side, eliminating the need for measurements on the high-voltage side.

The control algorithms developed in this thesis are primarily based on linear and average models, which offer a foundational approach to controlling power electronics by simplifying the system's dynamics. Moving forward, an important area for further exploration would involve the design of advanced control laws grounded in switched system theory. This approach would allow for a more accurate representation of the system's inherent switching characteristics, potentially improving control performance by addressing the fast, discrete changes in circuit states directly, rather than through averaged approximations. Implementing such control techniques would provide a more nuanced and responsive solution that aligns more closely with the system's real-time switching behavior, thereby enhancing stability, precision, and efficiency in high-voltage applications.

# Bibliography

- [1] Carmen Perri et al. “Modeling and validation of a high voltage driving circuit for dielectric elastomer actuators”. In: *2021 IEEE 30th International Symposium on Industrial Electronics (ISIE)*. IEEE. 2021, pp. 01–06.
- [2] Carmen Perri et al. “Design, modeling, and experimental validation of a high voltage driving circuit for dielectric elastomer actuators”. In: *IEEE Transactions on Industrial Electronics* 71.5 (2023), pp. 5083–5093.
- [3] Carmen Perri et al. “Closed Loop Positioning of a Dielectric Elastomer Actuator Driven by a Feedback-Controlled High Voltage Circuit”. In: *2024 IEEE 18th International Conference on Advanced Motion Control (AMC)*. IEEE. 2024, pp. 1–6.
- [4] Gianluca Rizzello et al. “Modeling, identification, and control of a dielectric electro-active polymer positioning system”. In: *IEEE Transactions on Control Systems Technology* 23.2 (2014), pp. 632–643.
- [5] Muhammad Khan et al. “Retracted: A concise review on the elastomeric behavior of electroactive polymer materials”. In: *International Journal of Energy Research* 45.10 (2021), pp. 14306–14337.
- [6] Federico Carpi et al. “Electroactive polymer actuators as artificial muscles: are they ready for bioinspired applications?”. In: *Bioinspiration & biomimetics* 6.4 (2011), p. 045006.
- [7] Federico Carpi et al. *Dielectric elastomers as electromechanical transducers: Fundamentals, materials, devices, models and applications of an emerging electroactive polymer technology*. Elsevier, 2011.
- [8] Alexander York and Stefan Seelecke. “Towards self-sensing of DEAP actuators: capacitive sensing experimental analysis”. In: *Smart Materials, Adaptive Structures and Intelligent Systems*. Vol. 44151. 2010, pp. 307–314.
- [9] Christopher R Walker and Iain A Anderson. “Monitoring diver kinematics with dielectric elastomer sensors”. In: *Electroactive Polymer Actuators and Devices (EAPAD) 2017*. Vol. 10163. SPIE. 2017, pp. 11–21.
- [10] Holger Böse and Johannes Ehrlich. “Dielectric Elastomer Sensors with Advanced Designs and Their Applications”. In: *Actuators*. Vol. 12. 3. MDPI. 2023, p. 115.
- [11] Frederikke B Madsen et al. “The current state of silicone-based dielectric elastomer transducers”. In: *Macromolecular rapid communications* 37.5 (2016), pp. 378–413.

- 
- [12] Soo Jin Adrian Koh et al. “Dielectric elastomer generators: How much energy can be converted?” In: *IEEE/ASME Transactions on mechatronics* 16.1 (2010), pp. 33–41.
- [13] Thomas G McKay et al. “Dielectric elastomer generators that stack up”. In: *Smart Materials and Structures* 24.1 (2014), p. 015014.
- [14] Sophie Kirkman et al. “Electromechanics of Planar HASEL Actuators”. In: *Extreme Mechanics Letters* 48 (2021), p. 101408. DOI: 10.1016/j.eml.2021.101408.
- [15] Nicholas Kellaris et al. “Peano-HASEL actuators: Muscle-mimetic, electrohydraulic transducers that linearly contract on activation”. In: *Science Robotics* 3.14 (2018), eaar3276.
- [16] Luc Maffli, Samuel Rosset, and HR Shea. “Zipping dielectric elastomer actuators: characterization, design and modeling”. In: *Smart Materials and Structures* 22.10 (2013), p. 104013.
- [17] WACKER, *ELASTOSIL Film 2030*. URL: <https://www.wacker.com/h/en-us/c/elastosil-film-2030/p/000038005>.
- [18] Gianluca Rizzello. “Modeling, Control and Self-Sensing of Dielectric Elastomer Actuators”. In: *Polytecnic University of Bari, Bari, Italy* (2016).
- [19] Micah Hodgins, Alex York, and Stefan Seelecke. “Modeling and experimental validation of a bi-stable out-of-plane DEAP actuator system”. In: *Smart Materials and Structures* 20.9 (2011), p. 094012.
- [20] Micah Hodgins, Alexander York, and Stefan Seelecke. “Experimental comparison of bias elements for out-of-plane DEAP actuator system”. In: *Smart Materials and Structures* 22.9 (2013), p. 094016.
- [21] Steffen Hau et al. “Silicone based dielectric elastomer strip actuators coupled with nonlinear biasing elements for large actuation strains”. In: *Smart Materials and Structures* 27.7 (2018), p. 074003.
- [22] Roy D Kornbluh et al. “Electroelastomers: applications of dielectric elastomer transducers for actuation, generation, and smart structures”. In: *Smart Structures and Materials 2002: Industrial and Commercial Applications of Smart Structures Technologies*. Vol. 4698. SPIE. 2002, pp. 254–270.
- [23] Ailish O’Halloran, Fergal O’malley, and Peter McHugh. “A review on dielectric elastomer actuators, technology, applications, and challenges”. In: *Journal of Applied Physics* 104.7 (2008).
- [24] Hyoukryeol Choi et al. “Multiple degree-of-freedom digital soft actuator for robotic applications”. In: *Smart Structures and Materials 2003: Electroactive Polymer Actuators and Devices (EAPAD)*. Vol. 5051. SPIE. 2003, pp. 262–271.
- [25] Federico Carpi et al. “Helical dielectric elastomer actuators”. In: *Smart Materials and Structures* 14.6 (2005), p. 1210.
- [26] Ji Su et al. “Electrostrictive grafr elastomers and applications”. In: *MRS Online Proceedings Library (OPL)* 600 (1999), p. 131.
-

- 
- [27] Michael Wissler and Edoardo Mazza. “Modeling of a pre-strained circular actuator made of dielectric elastomers”. In: *Sensors and Actuators A: Physical* 120.1 (2005), pp. 184–192.
- [28] Julian Kunze et al. “Design, manufacturing, and characterization of thin, core-free, rolled dielectric elastomer actuators”. In: *Actuators*. Vol. 10. 4. MDPI. 2021, p. 69.
- [29] Federico Carpi and Danilo De Rossi. “Dielectric elastomer cylindrical actuators: electromechanical modelling and experimental evaluation”. In: *Materials Science and Engineering: C* 24.4 (2004), pp. 555–562.
- [30] Rémi Waché et al. “Rotary motion achieved by new torsional dielectric elastomer actuators design”. In: *IEEE/ASME Transactions on Mechatronics* 20.2 (2014), pp. 975–977.
- [31] Thorben Hoffstadt and Jürgen Maas. “Analytical modeling and optimization of DEAP-based multilayer stack-transducers”. In: *Smart Materials and Structures* 24.9 (2015), p. 094001.
- [32] E-F Markus Henke, Samuel Schlatter, and Iain A Anderson. “Soft dielectric elastomer oscillators driving bioinspired robots”. In: *Soft robotics* 4.4 (2017), pp. 353–366.
- [33] Philipp Linnebach, Gianluca Rizzello, and Stefan Seelecke. “Design and validation of a dielectric elastomer membrane actuator driven pneumatic pump”. In: *Smart Materials and Structures* 29.7 (2020), p. 075021.
- [34] Liang Jiang et al. “Electrohydrodynamic printing of a dielectric elastomer actuator and its application in tunable lenses”. In: *Composites Part A: Applied Science and Manufacturing* 147 (2021), p. 106461.
- [35] Giacomo Moretti et al. “A multi-domain dynamical model for cone-shaped dielectric elastomer loudspeakers”. In: *Electroactive Polymer Actuators and Devices (EAPAD) XXIII*. Vol. 11587. SPIE. 2021, pp. 226–239.
- [36] Sascha Pfeil et al. “A worm-like biomimetic crawling robot based on cylindrical dielectric elastomer actuators”. In: *Frontiers in Robotics and AI* 7 (2020), p. 9.
- [37] Ahad Behboodi and Samuel CK Lee. “Benchmarking of a commercially available stacked dielectric elastomer as an alternative actuator for rehabilitation robotic exoskeletons”. In: *2019 IEEE 16th International Conference on Rehabilitation Robotics (ICORR)*. IEEE. 2019, pp. 499–505.
- [38] Iain A Anderson et al. “A dielectric elastomer actuator thin membrane rotary motor”. In: *Electroactive Polymer Actuators and Devices (EAPAD) 2009*. Vol. 7287. SPIE. 2009, pp. 470–479.
- [39] Onur Bilgen et al. “Lightweight high voltage electronic circuits for piezoelectric composite actuators”. In: *Journal of Intelligent Material Systems and Structures* 21.14 (2010), pp. 1417–1426.
- [40] Carsten Wallenhauer et al. “Efficiency-improved high-voltage analog power amplifier for driving piezoelectric actuators”. In: *IEEE Transactions on Circuits and Systems I: Regular Papers* 57.1 (2009), pp. 291–298.
-

- 
- [41] Shane K Mitchell, Trent Martin, and Christoph Keplinger. “A pocket-sized ten-channel high voltage power supply for soft electrostatic actuators”. In: *Advanced Materials Technologies* 7.8 (2022), p. 2101469.
- [42] Tirthasarathi Lodh and Hanh-Phuc Le. “An Ultra High Gain Converter for Driving HASEL Actuator Used in Soft Mobile Robots”. In: *Biomimetics* 8.1 (2023), p. 53.
- [43] Tirthasarathi Lodh and Hanh-Phuc Le. “Power Electronic Drivers for Electrostatic HASEL Actuators Used in Soft Mobile Robots”. In: *IEEE Journal of Emerging and Selected Topics in Industrial Electronics* (2023).
- [44] Lucas Pniak et al. “Ultrahigh-voltage switch for bidirectional dc–dc converter driving dielectric elastomer actuator”. In: *IEEE Transactions on Power Electronics* 35.12 (2020), pp. 13172–13181.
- [45] Chen Chen et al. “A low-power and high-gain converter for driving dielectric elastomer actuators”. In: *2013 Twenty-Eighth Annual IEEE Applied Power Electronics Conference and Exposition (APEC)*. IEEE. 2013, pp. 2755–2760.
- [46] S Reynolds. “A high-voltage, high-frequency linear amplifier/driver for capacitive loads”. In: *Measurement Science and Technology* 3.3 (1992), p. 283.
- [47] Samuel Schlatter, Patrin Illenberger, and Samuel Rosset. “Peta-pico-Voltron: An open-source high voltage power supply”. In: *HardwareX* 4 (2018), e00039.
- [48] Shmuel Ben-Yaakov and Mor Mordechai Peretz. “A self-adjusting sinusoidal power source suitable for driving capacitive loads”. In: *IEEE Transactions on Power Electronics* 21.4 (2006), pp. 890–898.
- [49] RP Massey and EC Snyder. “High voltage single-ended DC-DC converter”. In: *1977 IEEE Power Electronics Specialists Conference*. IEEE. 1977, pp. 156–159.
- [50] Prasanth Thummala, Zhe Zhang, and Michael AE Andersen. “High voltage Bidirectional flyback converter for capacitive actuator”. In: *2013 15th European Conference on Power Electronics and Applications (EPE)*. IEEE. 2013, pp. 1–10.
- [51] Raphael Mottet et al. “Ultra-high-voltage (7-kV) bidirectional flyback converter used to drive capacitive actuators”. In: *IEEE Transactions on Industry Applications* 57.5 (2021), pp. 5145–5156.
- [52] Gerardo Escobar, Arjan J Van Der Schaft, and Romeo Ortega. “A Hamiltonian viewpoint in the modeling of switching power converters”. In: *Automatica* 35.3 (1999), pp. 445–452.
- [53] Jürgen Maas and Thorben Hoffstadt. “Model-based control of a dual active bridge for bidirectional feeding of deep transducers”. In: *2014 IEEE/ASME International Conference on Advanced Intelligent Mechatronics*. IEEE. 2014, pp. 310–315.
- [54] Lina Huang, Zhe Zhang, and Michael AE Andersen. “Analytical switching cycle modeling of bidirectional high-voltage flyback converter for capacitive load considering core loss effect”. In: *IEEE Transactions on Power Electronics* 31.1 (2015), pp. 470–487.
-

- 
- [55] Huang Kewei et al. “Modeling analysis and simulation of high-voltage flyback DC-DC converter”. In: *2009 IEEE International Symposium on Industrial Electronics*. IEEE. 2009, pp. 813–818.
- [56] Sanjeev Kumar Pandey, SL Patil, and Vijaya S Rajguru. “Isolated flyback converter designing, modeling and suitable control strategies”. In: *Int. Conf. on Advances in Power Electronics and Instrumentation Engineering*. Citeseer. 2014, pp. 47–58.
- [57] Vaishnavi Ravi and N Lakshminarasamma. “Modeling, analysis, and implementation of high voltage low power flyback converter feeding resistive loads”. In: *IEEE Transactions on Industry Applications* 54.5 (2018), pp. 4682–4695.
- [58] Soroush Amini Akbarabadi, Hamid Atighechi, and Juri Jatskevich. “Circuit-averaged and state-space-averaged-value modeling of second-order flyback converter in CCM and DCM including conduction losses”. In: *4th International Conference on Power Engineering, Energy and Electrical Drives*. IEEE. 2013, pp. 995–1000.
- [59] Akshatha S Raj et al. “Modelling of flyback converter using state space averaging technique”. In: *2015 IEEE International Conference on Electronics, Computing and Communication Technologies (CONECCT)*. IEEE. 2015, pp. 1–5.
- [60] Heng-Yi Li and Hung-Chi Chen. “Dynamic modeling and controller design for a single-stage single-switch parallel boost-flyback-flyback converter”. In: *IEEE Transactions on Power Electronics* 27.2 (2010), pp. 816–827.
- [61] Brian T Irving, Yuri Panov, and Milan M Jovanovic. “Small-signal model of variable-frequency flyback converter”. In: *Eighteenth Annual IEEE Applied Power Electronics Conference and Exposition, 2003. APEC'03*. Vol. 2. IEEE. 2003, pp. 977–982.
- [62] Hafiz Kashif Iqbal and Ghulam Abbas. “Design and analysis of SMC for second order DC-DC flyback converter”. In: *17th IEEE International Multi Topic Conference 2014*. IEEE. 2014, pp. 533–538.
- [63] SQ Xie et al. “An adaptive control system for dielectric elastomers”. In: *2005 IEEE International Conference on Industrial Technology*. IEEE. 2005, pp. 335–340.
- [64] Gianluca Rizzello et al. “Modeling, identification, and control of a dielectric electro-active polymer positioning system”. In: *IEEE Transactions on Control Systems Technology* 23.2 (2014), pp. 632–643.
- [65] Mehdi Ferdowsi et al. “Pulse regulation control technique for flyback converter”. In: *IEEE Transactions on Power Electronics* 20.4 (2005), pp. 798–805.
- [66] Tsorng-Juu Liang, Kai-Hui Chen, and Jiann-Fuh Chen. “Primary side control for flyback converter operating in DCM and CCM”. In: *IEEE Transactions on Power Electronics* 33.4 (2017), pp. 3604–3612.
-

- [67] Chong Wang et al. “A constant current digital control method for primary-side regulation active-clamp flyback converter”. In: *IEEE Transactions on Power Electronics* 36.6 (2020), pp. 7307–7318.
- [68] Shen Xu et al. “A digital control scheme for PSR flyback converter in CCM and DCM”. In: *IEEE Journal of Emerging and Selected Topics in Power Electronics* 8.3 (2019), pp. 2837–2849.
- [69] Prasanth Thummala et al. “Digital Control of a High-Voltage (2.5 kV) Bidirectional DC–DC Flyback Converter for Driving a Capacitive Incremental Actuator”. In: *IEEE/ASME Transactions on Power Electronics* 31.12 (Jan. 2016), pp. 8500–8516.
- [70] Carlos Andres Ramos-Paja, Juan David Bastidas-Rodriguez, and Andres Julian Saavedra-Montes. “Sliding-mode control of a photovoltaic system based on a flyback converter for microinverter applications”. In: *Applied Sciences* 12.3 (2022), p. 1399.
- [71] Thorben Hoffstadt and Jürgen Maas. “Adaptive sliding-mode position control for dielectric elastomer actuators”. In: *IEEE/ASME Transactions on Mechatronics* 22.5 (2017), pp. 2241–2251.
- [72] MFN Tajuddin et al. “State space averaging technique of power converter with digital PID controller”. In: *TENCON 2009-2009 IEEE Region 10 Conference*. IEEE, 2009, pp. 1–6.
- [73] Stephen Boyd et al. *Linear matrix inequalities in system and control theory*. SIAM, 1994.